Phase Diversity

for the Deployable Space Telescope

D. Risselada

Delft University of Technology, Faculty of Aerospace Engineering

Phase Diversity

for the Deployable Space Telescope

by

D. Risselada

In partial fulfillment of the requirements for the degree of
Master of Science in Aerospace Engineering

at Delft University of Technology

To be defended at Tuesday February 5, 2019 at 13:00.

Student number:	4150724	
Thesis committee:	dr. A. Cervone,	Delft University of Technology, Committee Chair
	dr. ir. J.M. Kuiper,	Delft University of Technology, Supervisor
	dr. ir. W. van der Wal	Delft University of Technology

Cover photo adapted from an image taken by Planet's RapidEye, taken from effigis.com [1]

TU Delft

Summary

The Deployable Space Telescope Project (DST) was started at Delft University of Technology in 2014. The project aims to develop an ultra-high resolution Earth Observation telescope with a resolution of $0.25m$, but with a much lower mass and volume than its competitors currently in operation. In order to meet the stringent mass requirements, a deployable primary and secondary mirror are used. However, it is expected that the deployment of the optics will introduce severe aberrations in the system, limiting the performance. This thesis project investigated the implementation of phase diversity algorithms as a method for correction of these aberrations that does not add additional mass and complexity to the system. Phase diversity algorithms originate from the field of ground-based astronomy and are rarely used in space systems. Even less is known about their behavior in Earth Observation telescopes, which typically suffer from larger aberrations than ground-based telescopes. Also, Earth Observation telescopes image extended scenes instead of point objects. FORTA, a ray tracing application developed ir. D. Dolkens specifically for simulation of the Deployable Space Telescope Optics, was used for the simulation of the telescope imaging process. A MATLAB toolbox, developed during this project, was then used for simulation of a broad range of phase diversity algorithm configurations. These algorithm configurations numerous methods from the field of imaging, including an effective method for mitigating wrap-around effects resulting from the application of the Fast Fourier Transform. First, the set of algorithm parameters resulting in the optimum configuration in the context of the DST project was determined through a large number of parametric studies. After that, it was found through simulations that by using a novel method for the selection of the subframe to which phase diversity is applied a significant performance increase could be obtained. An analysis of the open-loop performance of the algorithm showed that the wavefront error in the exit pupil could be estimated to within a Root Mean Square (RMS) error of $0.07\lambda_0$ in over 75% of simulations, where $\lambda_0 = 450nm$ is the smallest wavelength accepted by the panchromatic channel, and that a Strehl ratio (SR) of above 0.8 was achieved in over 80% of cases. Through the development of an innovative post-processing method that exploits a priori knowledge of the expected error shape, both these percentages could be increased to above 85%. Deconvolution using a Wiener filter subsequently resulted in the reconstruction of details of smaller than $0.25m$, in accordance with requirements. In addition, an analysis of the closed-loop performance was done, in which the wavefront error estimates were used for iterative control of the active optics. This analysis showed that for initial Strehl ratios of higher than 0.6, the method would consistently increase the Strehl ratio to a value of around 0.8 or above. However, after an optimum was reached the method would diverge again. For the reliable implementation of phase diversity in a closed-loop configuration, an effective termination criterion should be developed. Phase Diversity methods show potential for implementation in the DST project, and it is recommended that further studies are performed. These studies should focus on making the method more reliable through identification of inaccurate estimations, as well as on the joint implementation of phase diversity with other calibration methods so that the strengths of phase diversity can be exploited and its weaknesses compensated.

Keywords: *Phase Diversity, Aberration Correction, Deployable Optics, Earth Observation, Gradient-Based Optimization, Imaging, Space Systems Engineering*

Preface

First and foremost I would like to thank Hans Kuiper and Dennis Dolkens for their invaluable support. Hans, thank you for creating a unique environment in which students get a chance to work on exciting projects together with experts from academia and industry, without taking from them the freedom to do things their own way. This is incredibly motivating and I enjoyed it very much to be part of the team. Dennis, it often feels like you know everything there is to know about space optics and the DST project. Moreover, you were always available at the most unorthodox hours to share this knowledge, for answering my questions and for helping me out with FORTA. Without your help and guidance, I don't think I would have gotten nearly as far as I got.

I would like to thank professor Paul Urbach and Yifeng Shao from the Department of Imaging Physics at the Faculty of Applied Physics, who provided me with very useful insights at the start of my thesis. These insights have played a vital role in completing the project.

To the other members of the DST team, past and present, as well as the other MSc room occupants I would like to say: thank you for the company and the laughs. Working on an MSc thesis can be a lonely endeavor at times, but regular coffee breaks with people who share the burden make it perfectly bearable. I would like to thank Gijsbert in particular for helping me at the start by sharing all his literature and insights with me, and Sean and Matys for providing feedback on my report.

Also a shout-out to all my friends, who supported me and provided me with very welcome distractions from my thesis when needed. In particular to my girlfriend's housemates and my own, for suffering my noisy laptop in the living room for weeks on end during the months when I was running simulations.

A very special thank you to my parents Rodie and Joke. You played a much larger role in achieving this and other milestones in my life than you will ever dare to admit to yourselves. And also to my brother. Daan, everything was a competition when we were kids. The competitive attitude we developed in those days has really helped me in bringing the project to fruition.

Finally, I want to thank my girlfriend Josephine for being so supportive of me, always. Working on this thesis, safe in the knowledge that I could always knock on your door when the project brought me down, made a world of difference. Here's to life after our theses!

Contents

List of Figures

List of Tables

Nomenclature

(ξ, η)	Position coordinates in the object plane
(f)	Shorthand notation for (f_X, f_Y)
(f_X, f_Y)	Spatial frequency coordinates in the image plane
(u)	Shorthand notation for (u, v)
(u, v)	Position coordinates in the image plane
(x)	Shorthand notation for (x, y)
(x, y)	Position coordinates in the pupil plane
α_j	j-th Zernike coefficient
$\bar{\lambda}$	Base wavelength in terms of which the wavefront error is defined
Δl	Ground resolution
Δu	Pixel pitch in the image plane
Δx	Pixel pitch in the exit pupil plane
κ	Adam alorithm learning rate
λ	Wavelength
λ_0	Smallest wavelength accepted by the system, $450nm$, wavefront error is expressed in terms of this wavelength for RMS calculation
$\mathbf{H}_{kl}$	Wavelength dependent Coherent Transfer Function for detector k and wavelenght with index l
$\mathbf{Z}_{jl}$	Wavelength dependent Zernike basis function j scaled for wavelength with index l
ϕ_k	Known phase error for the k-th detector
σ_n^2	Variance of the Gaussian noise distribution
θ	Wavefront error in the exit pupil plane
θ_{act}	Actual wavefront error
θ_{est}	Estimated wavefront error
θ_{res}	Residual wavefront error
D	Aperture diameter
F	Wiener deconvolution filter
G_g	Fourier transform of U_g
G_i	Fourier transform of U_i
g_k	Image plane intensity distribution predicted by noiseless but not aberration-free optics
H	Coherent Transfer Function (CTF), Fourier transform of h
h	Coherent Point Spread Function (Coherent PSF)

H_{kl} Coherent Transfer Function for detector k at sample wavelength with index l

h_{kl} Coherent Point Spread Function for detector k at sample wavelength with index l

H_{orbit} Orbital height

I Fourier transform of the intensity measurement i

i_g Intensity distribution in the image plane as predicted by aberration free noiseless geometric optics

i_i Intensity distribution in the image plane

I_k Fourier Transform of the k-th detector measurement

i_k image plane intensity measurement at the k-th detector

I_p Fourier transform of periodic part of image used for smooth decomposition

i_p Periodic part of image used for smooth decomposition

I_s Fourier transform of smoothly varying part of image used for smooth decomposition

i_s Smoothly varying part of image used for smooth decomposition

L Log-likelihood estimator

L_M Optimum log-likelihood metric

M Magnification

N Image side length in terms of the number of pixels

N_i Fourier transform of the detector noise term

n_i Detector noise term

N_{kl} Array size used for Fourier transform of the CTF for detector k and sample wavelength sample with index l

O Fourier transform of the intensity distribution of the object predicted by geometrical aberration-free optics

o Intensity distribution in the image plane as predicted by aberration-free geometrical optics

P Binary pupil function

S Optical Transfer Function (OTF)

s Point Spread Function

S_k Optical Transfer Function of the k-th detector

s_k Intensity Point Spread Function of the k-th detector

S_k^b Broadband phase diversity Optical Transfer Function for detector k

s_k^b Broadband phase diversity Point Spread Function for detector k

$s_{aberration-free}$ Intensity point spread function of an ideal, aberration-free optical system

s_{kl} Point Spread Function for detector k at sample wavelength with index l

s_{pix} Pixel PSF including both the effect of aberrations in the optical channel as well as the effect of sampling by the detector

T_{kl} product of grey world spectrum value and detector responsivity for detector k at the sample wavelength with index l

U_g	Amplitude distribution of the EM field in the object plane predicted by aberration-free, noiseless geometric optics
U_i	Amplitude distribution of the EM field in the image plane
U_o	Amplitude distribution in the image plane predicted by ideal, aberration-free geometrical optics
U_o	Amplitude distribution of the EM field in the object plane
w	Apodization window function
z_i	Distance between exit pupil and image plane
Z_j	j-th Zernike polynomial according to the Noll ordering

List of Abbreviations

CTF Coherent Transfer Function. xv, xvi, 23, 25, 103

DM Deformable Mirror. 12, 16, 18, 19, 60, 93

DST Deployable Space Telescope. iii, v, ix, 1, 4, 5, 7–11, 13, 15, 17, 19, 21, 23, 28, 33–35, 37, 39, 46, 95–98

EO Earth Observation. 1, 4, 16, 31, 94, 96

FFT Fast Fourier Transform. x, 40, 51, 71

FORTA Fast Optical Ray Tracing Application. iii, v, 33, 35, 46, 49, 51, 53, 69, 88

FOV Field of View. 9, 13

GSD Ground Sampling Distance. 1, 3, 7

MTF Modulation Transfer Function. 7, 15, 96

NSR Noise to Signal Ratio. 87

OPD Optical Path Difference. 18, 25, 52

OTF Optical Transfer Function. xvi, 24, 29, 30, 41, 44, 45, 103

PD Phase Diversity. 1, 19, 33, 53, 54, 83, 93, 94, 97

PSF Point Spread Function. ix, xi, xv, xvi, 22–28, 31, 35–37, 41, 42, 44–46, 49, 51, 82, 86–88, 94–96, 101–103

PV Peak to Valley. 25

RG Reduced Gaussian. 29, 30

RMS Root Mean Square. iii, x, xi, xiv, xv, 15, 27, 31, 47, 52, 53, 60, 66, 69, 71, 82, 83, 85, 86, 89, 93–96, 119, 120

SGD Stochastic Gradient Descent, refers to the Parallel Pertubation Stochastig Gradient Algorithm developed by van Marrewijk. 17, 97

SNR Signal to Noise Ratio. xiii, 7, 35, 36, 44, 45, 49, 61, 75, 88, 98, 110

SR Strehl Ratio. iii, x, xi, 27, 51, 83, 86, 93

TDI Time Delay and Integration detector. xi, xiii, 9, 17, 33, 34, 36, 37, 41, 48, 49, 51–53, 56, 61, 75, 77, 79, 86–88, 97, 108, 110

1
Introduction

The possibility to observe the Earth from space using satellite imagery has opened many doors in myriad fields. Nowadays, more than fifty years after the launch of the first Earth observation satellite, the first of a series of seven weather monitoring satellites aptly named "Nimbus", sectors like farming, environmental monitoring and defense depend heavily on remote sensing for many of their operations [12]. Where the availability of satellite imagery once shook each of these sectors to its foundations, the tables have now turned and businesses, institutes and governments are driving the development of remote sensing technology toward even higher resolutions and broader coverage.

Currently setting the standard in high-resolution Earth imaging, is the WorldView-4 satellite developed and operated by DigitalGlobe [13]. With a spatial resolution of $0.31m$ the WorldView-4 has the highest resolution of all commercial earth imaging satellites currently in operation. However, as outlined by Dolkens [9], the current generation of high-resolution Earth imaging systems are all very large in terms of both mass and volume, in the order of thousands of kilograms. Consequently, they are very expensive to build and launch. In addition, these systems often have small swath widths, which results in the need for large constellations of ultra-high resolution satellites if a high temporal resolution or broad coverage is required. Because of the combination of the high unit costs and the limited coverage, the costs of ultra-high resolution Earth observation (EO) imagery is currently very high.

This chapter will introduce a proposed solution to this problem in the form of the Deployable Space Telescope, currently developed at Delft University of Technology. The DST is an ultra-high resolution space telescope with a low mass and deployable optics that can be folded into a small volume for launch. After the context of the project, the project mission and the current state of the project are discussed, elaboration will be provided on the main topic of this thesis project. The topic is improvement of the image quality using a class of algorithms called Phase Diversity (PD) algorithms. The main thesis goal relating to this topic can be expressed as: *To determine whether the implementation of Phase Diversity algorithms is a suitable strategy for aberration correction for the Deployable Space Telescope.*

First, section 1.1 will present a short analysis of the current Ultra-high resolution EO satellite market. After that, section 1.2 provides an overview of the DST mission. Section 1.3 will present the current state of the optical design. Section 1.4 will present the current state of the aberration correction strategy and finally 1.5 will present the thesis goal and research questions that will be answered in this report.

1.1. Ultra High Resolution Earth Observation Market

An overview of satellites capable of taking images with a ground resolution below $10m$ taken from the work of Dolkens is presented in table 1.1 [10]. A scatter plot of the same data is presented in figure 1.1. From the data, it can observed that the WorldView-4, which has a ground sampling distance (GSD) of $30cm$ currently provides the highest resolution of all systems in operation. The Worldview-4 image presented in figure 1.2, shows that such a resolution even makes it possible to distinguish individual humans.

However, this resolution comes at a cost. Table 1.1 also shows that with a mass of over $2000kg$ and dimensions as shown in figure 1.3, the telescope is one of the heaviest in operation. The high volume and mass lead to very high launch costs. It is estimated that expenses for the WorldView-4, including launch, amount to USD $835M$ including the costs of upgrading the DigitalGlobe ground station network [14]. High capital ex-

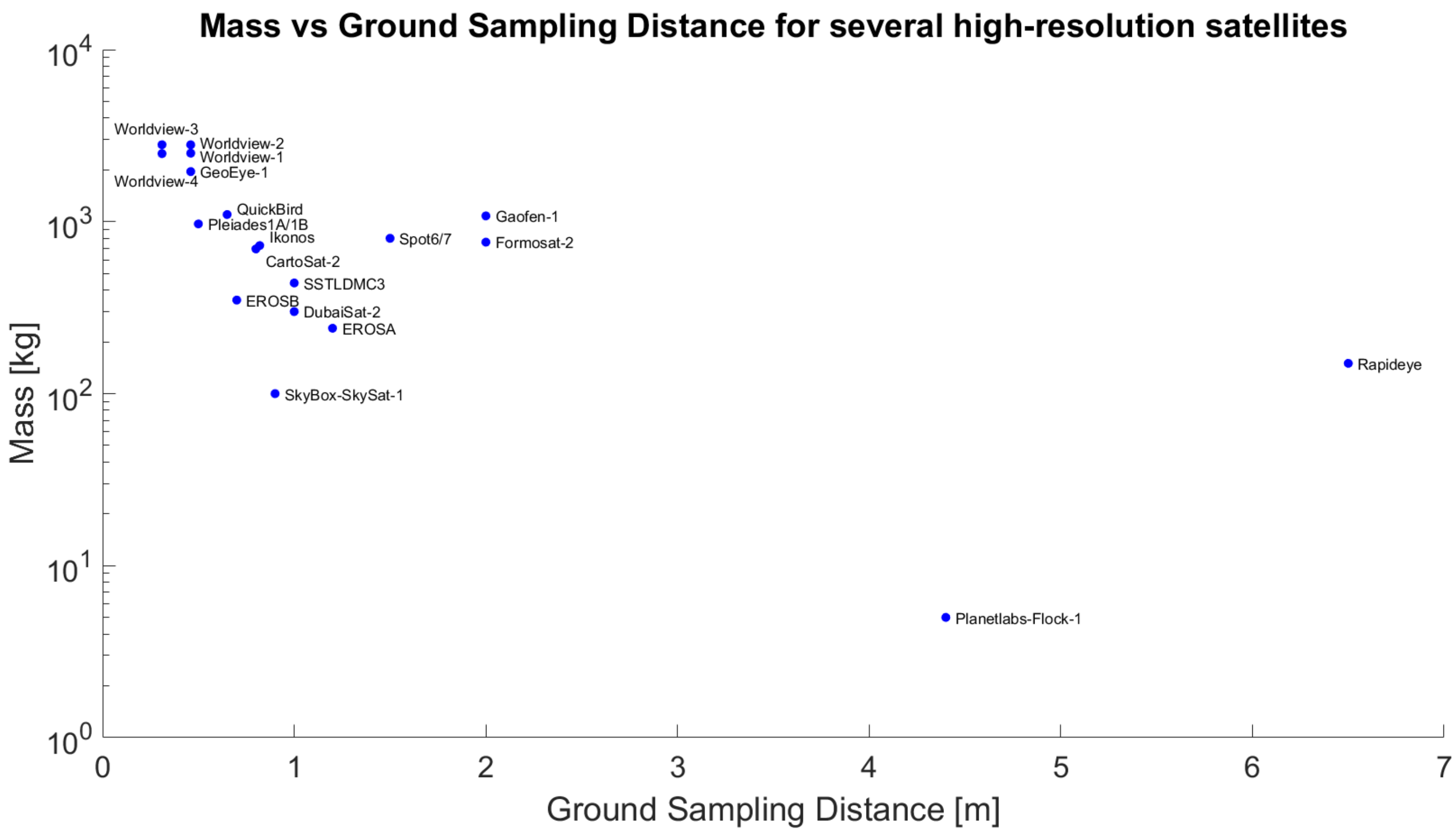

Figure 1.1: Scatter plot of the mass vs the ground sampling distance for the systems listed in table 1.1.

Table 1.1: List of high resolution Earth observation satellites currently in operation, as presented by Dolkens [9].

Mission	**Launch Year**	**Mass [kg]**	**Altitude [km]**	**GSD [m]**	**GS @ 500 km [px/m]**	**Swath Width [km]**	**Swath Width [1000 pixels]**
Worldview-4	2016	2485	617	0.31	3.98	13.1	42
Worldview-3	2014	2800	620	0.31	4	13.1	42
Worldview-2	2009	2800	770	0.46	3.35	16.4	36
GeoEye-1	2008	1955	770	0.46	3.35	15.2	33
Pleiades 1A / 1B	2011 / 2012	970	695	0.5	2.78	20	40
Worldview-1	2007	2500	496	0.46	2.16	17.6	38
Ikonos	1999	726	681	0.82	1.66	11.3	14
CartoSat-2	2010	694	630	0.8	1.58	9.6	12
QuickBird	2001	1100	482	0.65	1.48	16.8	26
EROS B	2006	350	506	0.7	1.45	7	10
SSTL DMC3	2014/2015	440	650	1	1.3	24	24
DubaiSat-2	2013	300	600	1	1.2	12.2	12
SkyBox - SkySat-1	2013	100	450	0.9	1	8	9
Spot 6/7	2012 / 2014	800	694	1.5	0.93	60	40
Formosat-2	2004	760	888	2	0.89	24	12
EROS A	2000	240	523	1.2	0.87	14	12
Gaofen-1	2013	1080	645	2	0.65	69	35
Rapideye	2008	150	620	6.5	0.19	77	12
Planetlabs - Flock-1	2013	5	410	4.4	0.19	25	6

Figure 1.2: The Louvre in Paris, as captured by DigitalGlobe's WorldView-4 satellite[2].

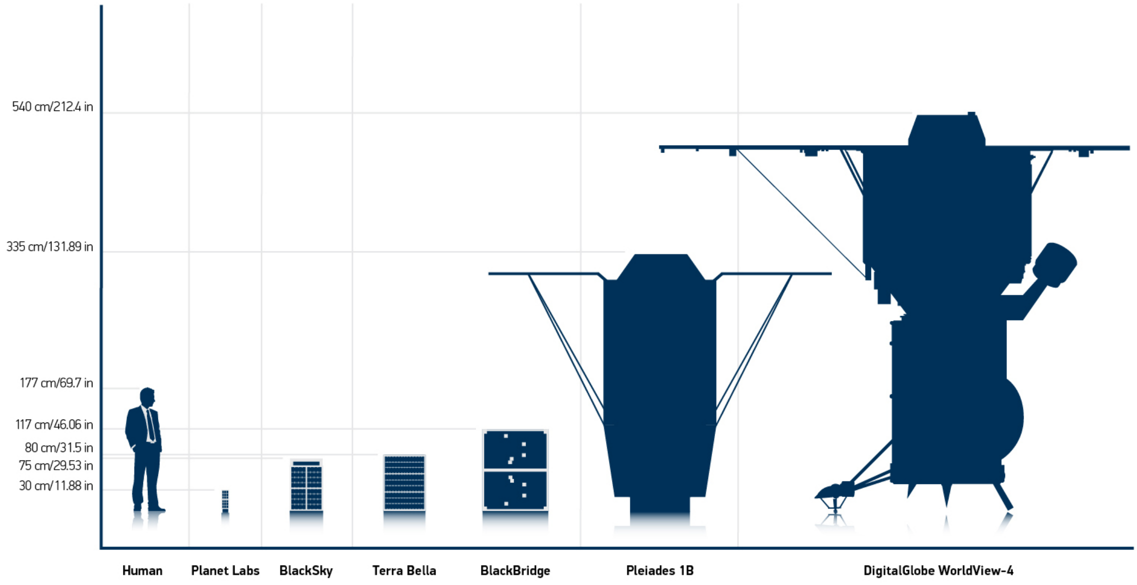

Figure 1.3: Schematic representation of the volume of the WorldView-4 telescope and some of its competitors. This image was created by DigitalGlobe [3].

penses like this have to be compensated for by high prices for imagery and limit the possibility of launching large constellations.

It can be concluded that to achieve a reduction in the price of high resolution satellite imagery and enable a broader coverage and increased temporal resolution it is necessary to decrease the mass and volume of high resolution Earth observation satellites. This necessity is the driving force behind the DST project.

1.2. Project Mission

This section will provide a short introduction to the motivation for the Deployable Space Telescope project and the inherent challenges of building earth observation telescopes with low mass and volume. The section will start with an introduction to the diffraction limit, a law of nature that is the main factor dictating the large dimensions of high-resolution EO satellites.

1.2.1. The Diffraction Limit

The attainable spatial resolution of an ideal optical instrument is still limited by the effects of diffraction. Through research in the field of optics performed by Christiaan Huygens and later by Augustin-Jean Fresnel it was discovered that every point on the wavefront of a light wave acts as a point source emitting spherical wavelets[15] [16]. When a light wave passes to a finite aperture, this behavior leads to scattering of the light wave around the edges. This effect is not uniquely affiliated with light waves, but can also be observed in other types of waves. Figure 1.4 shows a schematic representation of diffraction as well as a real-world example of the diffraction of ocean waves. Due to this diffraction effect, light entering the optical system originating from a single point on the object is "smeared out" onto the image plane. A typical example of this smearing is the Airy disk, an intensity pattern that arises when a single point source is imaged using a circular aperture, shown in figure 1.5 [17].

This blurring caused by diffraction effects leads to an irreversible loss of small details in the imaging process, consequently limiting the aberration-free resolution that can be achieved. The diffraction limited resolution is the minimum ground distance at which two distinct point objects can be resolved by the imaging system. For the particular case of the circular aperture, this is when in the image plane the center lobe of the Airy disk resulting from the imaging of the first point coincides with the first dark ring of the Airy disk resulting from the imaging of the second point and two distinct peaks can be observed. This is called the Rayleigh criterion and is shown in figure 1.6 [18]. A mathematical representation of this criterion is provided

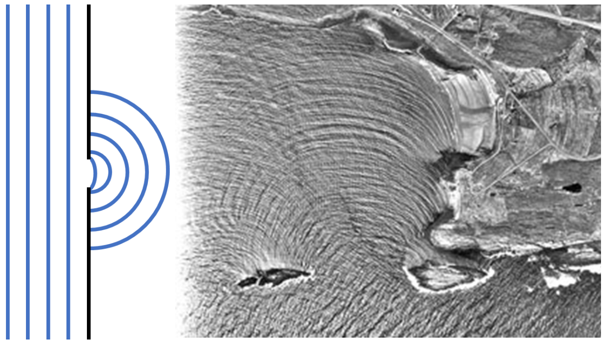

Figure 1.4: 2D visualization of diffraction effects for a lightwave passing through a finite aperture [left] and a real world example from ocean waves passing between two islands [right]. Photograph taken from [4].

in equation (1.1). While apertures are generally not circular the Rayleigh criterion has been shown to give accurate results even for non-circular apertures [5]. The representation of the criterion provided here has already been slightly rewritten to represent the specific case of an Earth observation satellite in orbit. In this equation the variable Δl is the ground resolution, H_{orbit} is the orbital height, λ is the wavelength of the light and D is the aperture diameter, all measured in meters. As can be observed the resolution is inversely proportional to the aperture diameter. If, for example, one requires a resolution of $0.25m$, similar to the resolution of WorldView-4, flying at an orbital height of $550km$ and assuming a wavelength of $\lambda = 550nm$, one would require an aperture diameter of at least $D = 1.48m$.

$$\Delta l = 1.220 H_{orbit} \frac{\lambda}{D} \tag{1.1}$$

Diffraction provides an aperture size dependent upper limit to the resolution and therefore dictates a hard lower limit for the aperture size if a certain resolution is to be achieved. The large aperture diameter required to achieve a resolution of $0.25m$, however, also requires a large platform to support. This leads to the large volumes and high masses that can be observed in table 1.1.

A space telescope with deployable optics could potentially be a solution to this problem because it would reduce the launch volume of the spacecraft. In addition, it is hypothesized that enabling relaxation of the otherwise stringent mechanical requirements on the deployment mechanisms through the use of state-of-the-art active aberration correction methods and image post-processing can lead to a great reduction in mass relative to existing systems.

Due to the potential reduction in the cost of ultra-high satellite imagery and increase in the coverage, the DST project was initiated with the goal of developing:

> *a deployable space telescope on a microsatellite platform with a resolution equal to the highest resolution achieved by a satellite currently in operation and a significantly lower volume and mass than other ultra-high-resolution satellites* [19].

However, deployable optics require the use of hinges. The use of moving parts in combination with relaxed mechanical requirements is expected to lead to aberrations in the system. Aberrations are blurs in the image plane that result from irregularities, misalignments and vibrations in the optical elements. A more in-depth of the effects and origins of aberrations is provided in section 1.4.1. If a high resolution is to be achieved, these aberrations have to be corrected. The focus of this MSc thesis project will be on the topic of aberration correction for the DST using phase diversity methods. The motivation for this topic will be presented later in this report.

Before the report will elaborate on the goal the goal of this thesis project is presented, first an in-depth discussion of the DST project is provided, starting with the mission requirements.

1.2.2. Mission Requirements

For the DST project the following mission requirements were defined and justified by Dolkens [9]:

REQ-1 The Ground Sampling Distance of the instrument shall be equal to 25 cm in the panchromatic band from an orbital altitude of 500 km

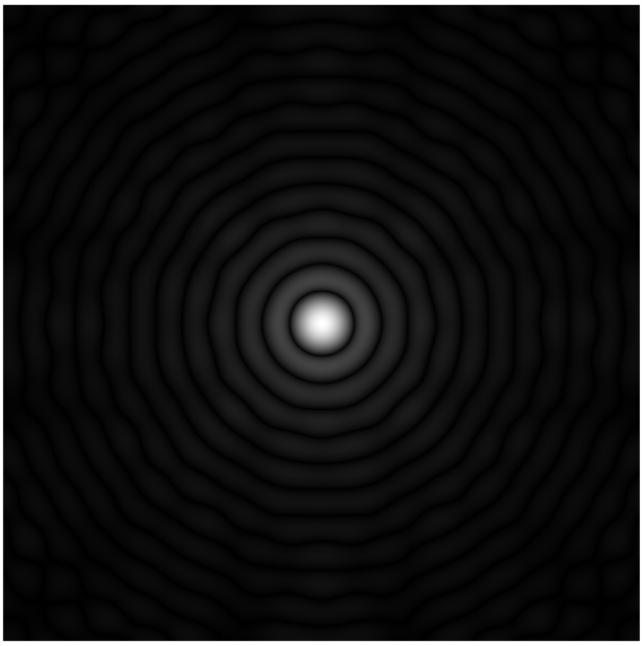

Figure 1.5: Airy disk pattern, caused by diffraction effects, resulting from the imaging of a single point using a circular aperture.

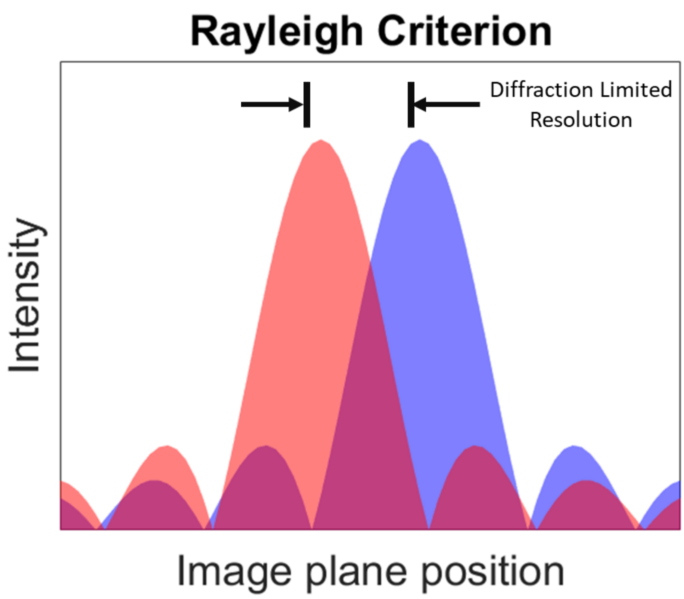

Figure 1.6: 1D representation of the Rayleigh criterion. The red and blue intensity distributions result from the imaging of the first and second point respectively. It can be observed that their peaks align with the first dark ring of the other distribution.

REQ-2 The swath width of the instrument shall be wider than 1 km (threshold) / 5 km (goal)

REQ-3 The system shall have one panchromatic channel and four multispectral bands with the wavelength ranges and GSD indicated in Table 1.2

REQ-4 The Signal-to-Noise Ratio (SNR) of the instrument shall be higher than 100 for a reflectance of 0.30 and a sun Zenith angle of 60 degrees

REQ-5 The nominal Modulation Transfer Function (MTF) at both the Nyquist frequency and half the Nyquist frequency shall be higher than 5% (threshold) / 15% (goal)

REQ-6 After calibration, the residual Strehl ratio of the system shall be higher than 0.80.

REQ-7 The mass of the instrument shall be lower than 100 kg (threshold) / 50 kg (goal)

REQ-8 In the stowed configuration, the volume of the instrument shall not exceed 1.5 m^3 (threshold) / 0.75 m^3 (goal)

Table 1.2: Ground Sampling Distances for the different optical channels [9].

Channel	**GSD at 500 km** $[m]$
Panchromatic ($450-650nm$)	0.25
Blue ($450-510nm$)	1
Green ($518-586nm$)	1
Yellow ($590-630nm$)	1
Red ($632-692nm$)	1

One concept central to aberration correction is the Strehl ratio that is mentioned in **REQ-6**. The Strehl Ratio is a measure of the severeness of the optical aberrations in the optical system. An optical system with a Strehl ratio above 0.8 is generally considered to be diffraction-limited, i.e. the performance of the optics is limited by diffraction effects instead of aberration effects. A mathematical explanation of this concept will be presented in section 2.1.4.

To design a system that meets these mission requirements, a project organization has been set-up that will be introduced in the next section.

1.2.3. Project Organization

The Deployable Space Telescope project was conceived at the Delft University of Technology in 2014 by dr. ir. J.M. Kuiper. A preliminary design has been made by ir. Dolkens, who performed his MSc thesis project on the subject of the DST, and is currently still working on the design of the telescope as part of his Ph.D. research under the supervision of dr. Kuiper. For the past years, a team consisting of several MSc and Ph.D. students has been working continuously on the design of the telescope. An overview of the project team, including both present as well as past members, is shown in figure 1.7.

While the contributions made by the thermo-mechanical team will be introduced briefly, the optical part of the DST design will be the main focus of this thesis. The optical design was primarily developed by Dolkens and extended by van Marrewijk and will be discussed in the next section. While the design has seen several iterations since its inception, only the most recent configuration will be presented here.

1.3. Optical Design

A render of the complete design is presented in its deployed state is presented in figure 1.8. This section will focus on the optical design of the telescope in particular. The design of the optics will be discussed in two parts. The first part discusses the ideal design of the optical channel including the shapes, dimensions, and positions of all the optical elements. The second part discusses the tolerance budgets. These are the allowable deviations from the ideal design. The discussion treats their impact on the optical performance and the design of mitigation strategies to counteract the detrimental effect of these tolerances.

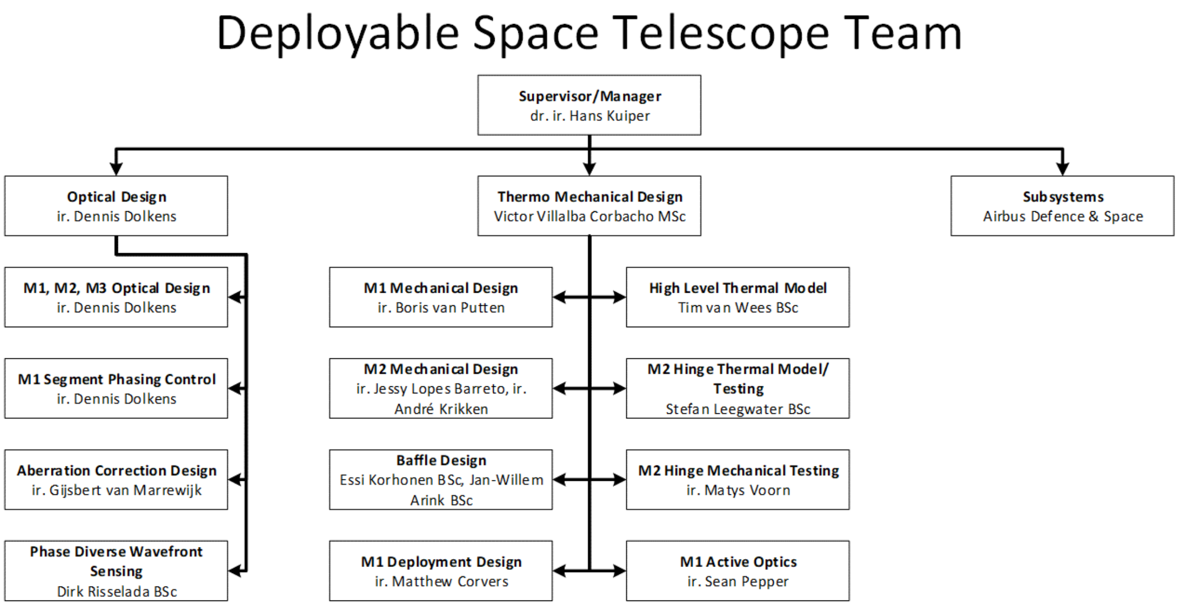

Figure 1.7: Overview of the Deployable Space Telescope team.

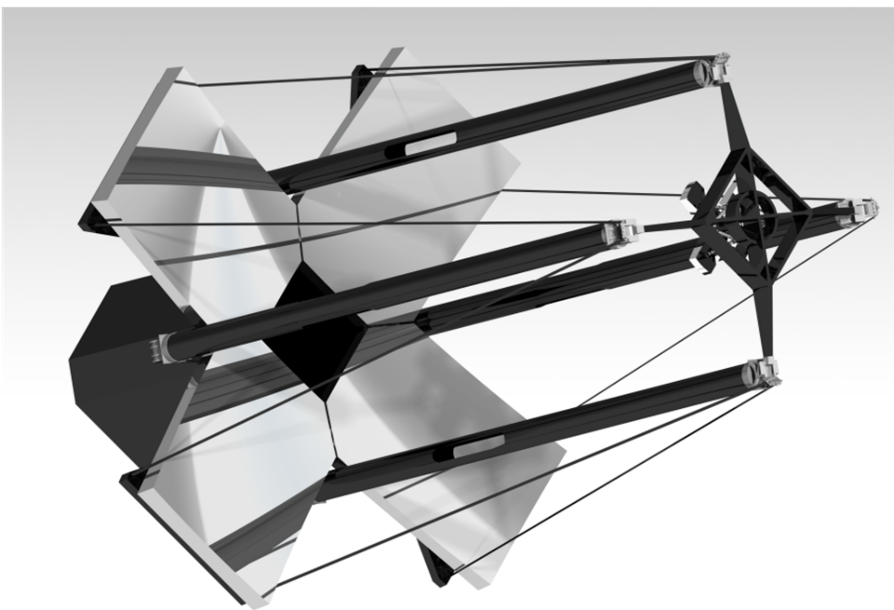

Figure 1.8: Render of the current DST design in its deployed state

1.3.1. Main Optical Elements and Deployability

It has been decided in an early phase of the design to avoid the use of refractive elements, lenses, in the design and exclusively use reflective elements, mirrors. This is because the use of lenses produces chromatic aberrations, i.e. aberrations that are wavelength dependent. Because the panchromatic channel of the DST spans virtually the entire visible wavelength spectrum, from $450nm$ to $650nm$, it is expected that the use of refractive elements would result in large chromatic aberrations. Chromatic aberrations are difficult to correct during post-processing without the loss of detail in the image [20]. It has also been found by Dolkens that to effectively minimize the three most common aberrations, i.e. spherical aberration, coma and astigmatism a configuration consisting of a minimum of three mirrors is required. It has therefore been decided include exactly three mirrors in the design so that the three main aberrations can be mitigated without adding unnecessary complexity and weight to the system. Such a three-mirror configuration is aptly called a three-mirror anastigmat. For the design, a trade-off has been made between a full field Korsch 3 mirror Anastigmat and an annular field Korsch 3 mirror Anastigmat [21]. Eventually, the latter has been selected, because it can support a wide field of view (FOV), as required by **REQ-2**, with significantly less stringent alignment tolerances for the mirrors, and no reduction in contrast, when compared to the full field Korsch configuration. A side view and a 3D view of the current optical design are presented in figures 1.9 and 1.10. The color of each set of rays corresponds to the field angle in the along-track direction from which these rays originate. They are not related to the actual color of the light.

It can be observed that the volume of the telescope is primarily determined by two key dimensions:

1. The radius of the primary mirror M1
2. The distance between the primary mirror M1 and the secondary mirror M2

In order to meet requirement **REQ-8** it is therefore imperative to reduce these two dimensions mentioned above during launch. Based on this reasoning two critical design choices have been made:

1. The primary mirror M1 design has been divided into four identical segments that can be folded outward against the sides of the instrument housing during launch.
2. The secondary mirror M2 will be mounted on four identical booms that can be folded during launch so that the distance between M1 and the bus can be greatly reduced during launch.

A schematic representation of the M1 mirror including the dimensions is provided in figure 1.11, a representation of the deployment of the mirror is provided in figure 1.12.

Extensive work on the M1 deployment hinges has been done by van Putten, Corvers, and Pepper during their MSc graduation projects [22] [23] [24]. Work on the M2 support structure and deployment mechanisms has been done by students Lopes Baretto, Krikken, and Voorn [25] [26] [27]. During the publication of this thesis, MSc students Leegwater, van Wees, Korhonen and Arink and Ph.D. student Villalba Corbacho are working on the (thermo-)mechanical design of the telescope. A further elaboration of the structural, mechanical and thermal design of the telescope will not be provided here since for this thesis project it is only relevant to known the tolerances in terms positioning and alignment errors. Not how these tolerances requirements are met in the mechanical design. For conciseness, readers are thus referred to the theses mentioned above in case of questions about the mechanical and structural design.

1.3.2. Image Plane and Deformable Mirror

Zooming in on the right part of figure 1.9, shown here in figure 1.13, it can be observed that the rays from different field angles arrive at different detectors. The rays from the smallest field angles, colored blue and red, are guided towards the TDI-1 and TDI-2 detectors. Because the detectors are placed next to each other in the along-track direction, a certain scene is first imaged by TDI-1 and after a certain time delay depending on the field separation, TDI-2 images the same scene. The rays originating from higher field angles, indicated with greed and turquoise, arrive at the wavefront sensor/sharpness sensing location and the multispectral channel respectively. While the design of the panchromatic and multispectral channel is already at an advanced stage, the exact form of wavefront sensing is still under consideration.

Under ideal circumstances, this system should be able to achieve diffraction limited performance and consequently meet the optical performance requirements. However, due to finite manufacturing accuracies, vibrations, and thermal effects during operation, the performance of the system is expected to be significantly impeded by the presence of optical aberrations. To push the system performance to meet the lower limit set

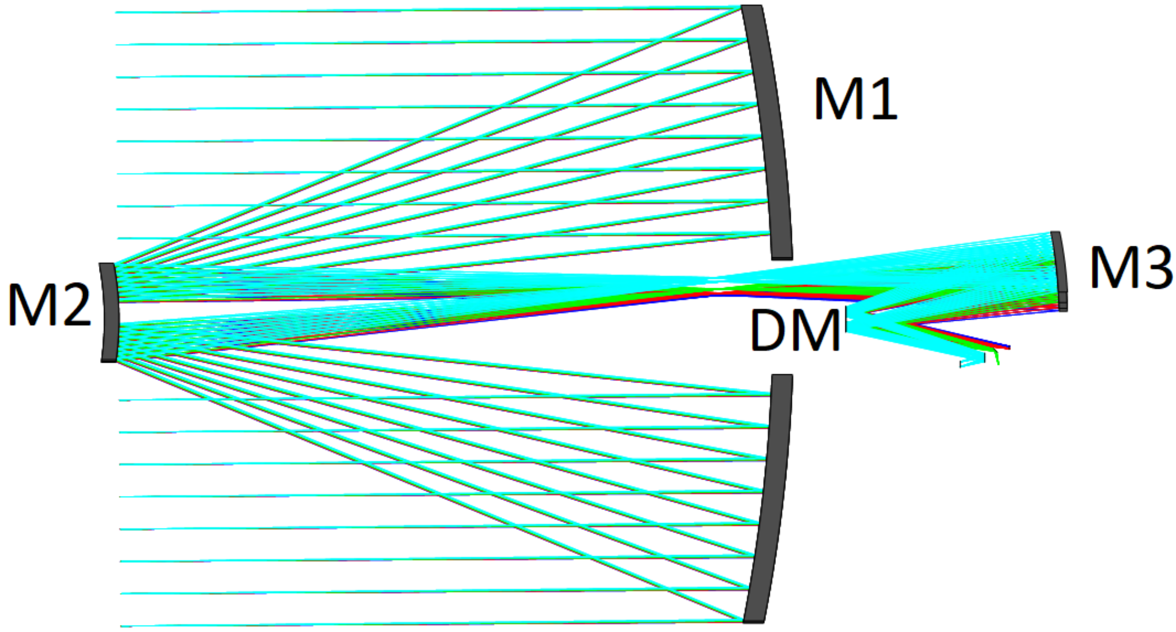

Figure 1.9: Final annular field Korsch telescope design of the DST [10]

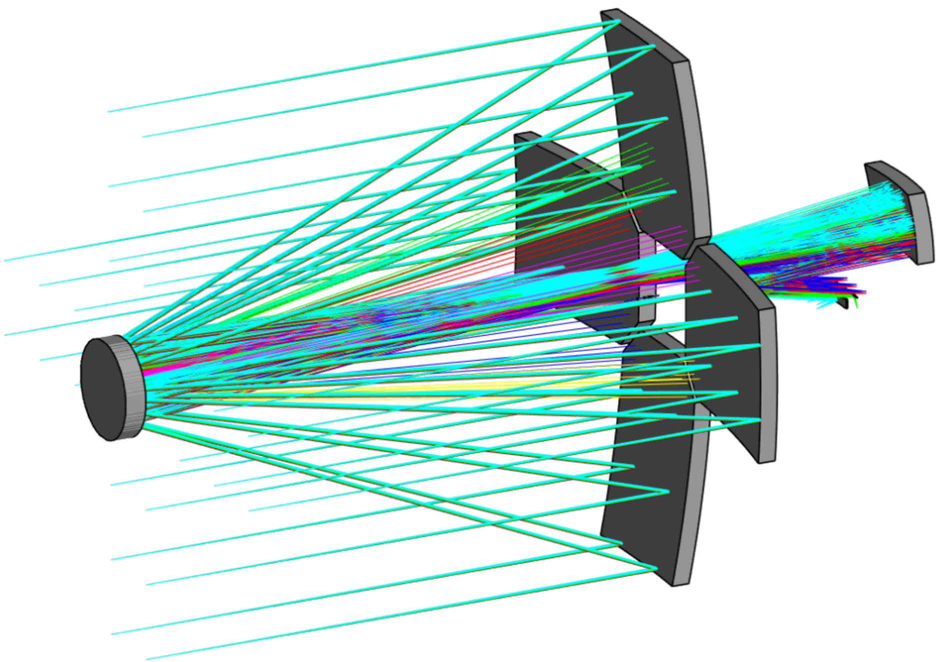

Figure 1.10: 3D view of the optical design of the DST, rays of different color indicate different field angles.

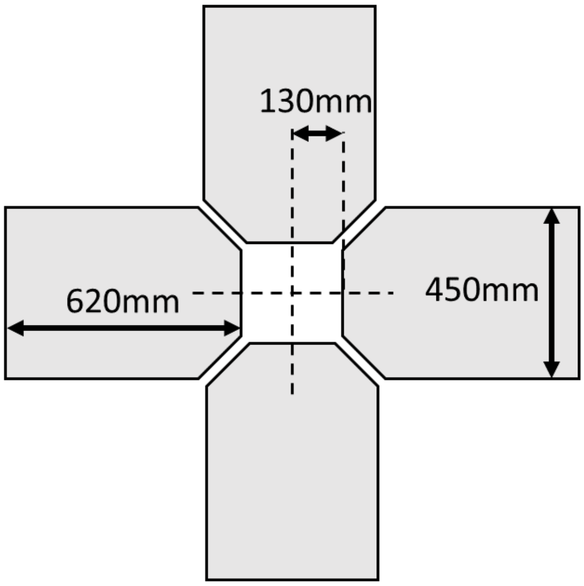

Figure 1.11: The four segment primary mirror selected for the DST.

Figure 1.12: Visual representation of the deployment of the telescope.

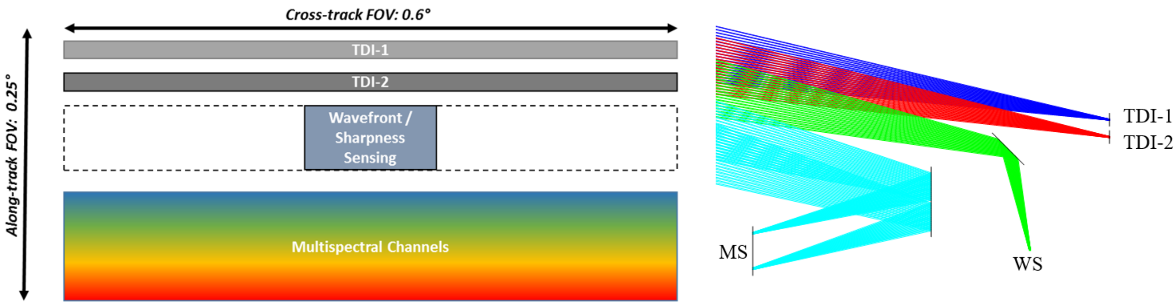

Figure 1.13: Detector configuration for the DST [10]

by the requirements, an optical aberration correction strategy should be implemented. While a final decision on the aberration correction system still has to be made, it is intended that the results of this thesis will provide a rigorous basis for making this decision, possible strategies can be roughly classified in two categories: passive aberration correction and active aberration correction. While passive aberration correction aims to increase the image quality through post-processing, active aberration correction corrects wavefront errors in the optical channels through control of the active optics. The active optics consist of the optical elements of which either shape, position or orientation can be changed in order to manipulate the light and reduce aberrations. Due to the stringent requirements on the weight and complexity of the design, it is anticipated that a combination of passive and active aberration correction methods is required for achieving diffraction limited performance. Therefore a deformable mirror (DM) for active aberration correction has been added to the design, in between M3 and the detectors. The location of the DM has been indicated in figure 1.9. A more elaborate discussion on aberration correction strategy and active correction using the DM will be discussion in section 1.4. First, a discussion on the mechanical tolerances for the primary, secondary and tertiary mirror is provided.

1.3.3. Design Budgets

Based on the performance requirements listed in Section 1.2 and the preliminary design work done a list of tolerance budgets has been determined for the design presented in the previous section [10]. These budgets take into account the *Deployment and Coarse Alignment* tolerances, the *In-Orbit Drifts* and the *Stability* budgets and are presented in table 1.3. In addition to these budgets, a budget was also determined for the primary mirror actuator control resolution. This budget was set to $10nm$. This was done to make sure that the control resolution does not noticeably impact the image quality.

Table 1.3: Top-down tolerance budgets for the primary, secondary and tertiary mirrors [10].

Element	**Position [µm]**			**Tilt [µrad]**			**Radius [%]**	**Shape Error [nm]**
	X	**Y**	**Z**	**X**	**Y**	**Z**		
Deployment and Coarse Alignment Tolerances								
M1	2	2	2	2	4	50	$1\cdot10^{-3}$	50
M2	15	15	10	100	100	100	$1\cdot10^{-2}$	25
M3	4	4	4	10	10	50	$1\cdot10^{-3}$	10
In-Orbit Drifts								
M1	$2\cdot10^{-2}$	$2\cdot10^{-2}$	$2\cdot10^{-2}$	$1\cdot10^{-2}$	$2\cdot10^{-2}$	5	$1\cdot10^{-4}$	5
M2	4	4	2	6	6	12	$1\cdot10^{-4}$	5
M3	$1\cdot10^{-1}$	$1\cdot10^{-1}$	$1\cdot10^{-1}$	1	1	5	$1\cdot10^{-4}$	5
Stability Budget								
M1	$5\cdot10^{-3}$	$5\cdot10^{-3}$	$5\cdot10^{-3}$	$2.5\cdot10^{-3}$	$1\cdot10^{-2}$	$5*10^{-1}$	n/a	n/a
M2	1	1	$5\cdot1^{-1}$	1.5	1.5	3	n/a	n/a
M3	$2.5\cdot10^{-2}$	$2.5\cdot10^{-2}$	$2.5\cdot10^{-2}$	$2.5\cdot10^{-1}$	$2.5\cdot10^{-1}$	1.25	n/a	n/a

It was found by Dolkens that, because complying with these budgets alone does not lead to diffraction limited imaging by itself, additional aberration correction is required. The rationale behind these budgets is based on the assumption of an operational strategy that involves the following steps:

1. After deployment all errors should be within the tolerances listed under "Deployment and Coarse Alignment Tolerances". At this point, the primary mirror segments are still expected to be misaligned and a phasing step is performed to correct the position and alignment of the four mirror segment. Each individual mirror segment control actuator has three degrees of freedom: the controller can move the mirror up and down (piston) and correct the angle of the mirror around the two axes perpendicular to the optical axis of the system. A design for the controller was developed by Pepper [24] during his MSc graduation project. The performance that can be acquired using this M1 phasing system will be presented later in this chapter. In addition, calibration using the DM will also be performed, altough the final calibration method has yet to be determined.

2. Between the M1 phasing events, changes will occur in the positions and shapes of the mirror components. The reason for this is that the system will be subject to both thermal as well as mechanical loads during operation, which cause the optical components to deviate from their original positions.

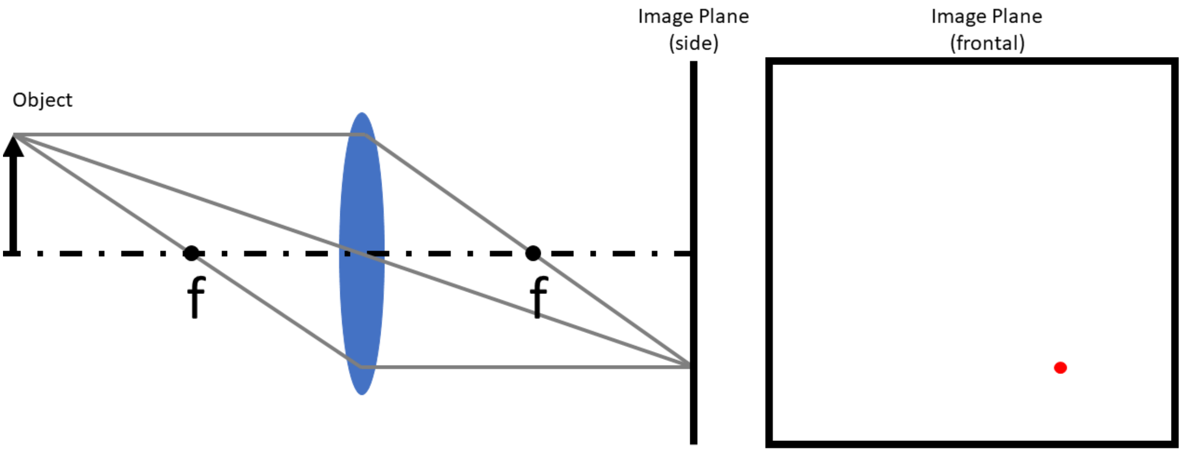

Figure 1.14: Schematic representation of an ideal lens where light from an object converges to a single point.

These deviations are covered by two separate budgets, the *Drift* budgets, and the *Instability* budgets. The *Drift* budgets are the tolerance budgets for all deviations that do not change noticeably during the acquisition of a single image, the *Instability* budgets are all deviations that do vary throughout the acquisition of a single image. While the *Instability* budgets have been chosen such that their impact on imaging will be very small, the *Drift* budgets are less stringent. The budgets have been chosen such that it is expected that they allow the system to meet the mass requirements, but stringent enough to allow a well-designed aberration control system to push the system performance to the level of diffraction-limited performance

All the design work done for the DST is done taking into account these engineering budgets to ensure that the final design will be able to achieve diffraction-limited resolution over the entire FOV. In the next section, a short introduction to the concept of aberrations is provided, including the work done by van Marrewijk and Dolkens on wavefront estimation and correction.

1.4. Aberration Correction Strategy

Aberrations have been described as anomalies resulting from unwanted mechanical characteristics of the optics of the system in turn resulting from nonzero tolerances such as the mechanical tolerances presented in table 1.3. To understand the aberration correction strategies presented here a slightly deeper understanding of aberrations is required.

1.4.1. Aberrations in Geometrical Optics

This understanding can be achieved through the use of geometrical optics, the branch of optics that describes light as rays, perpendicular to the wavefront of the light wave. Neglecting diffraction for a moment, it can be stated that light coming from a single point source that goes through an idealized lens converges in a single point as is shown in figure 1.14. In this image, the symbol f indicates the focal point of the lens. If all the rays converge to the same location, the result is a single point in the image. In practice, light rays never converge to exactly the same point let alone a point that lies exactly on the image plane. This deviation from convergence to a single point, caused by light rays following a different path than their theoretical ideal path, causes a blur. These different 'blurs' are called aberrations and are caused by myriad phenomena.

Aberrations are conveniently classified into several types, which are in turn classified in orders. The higher the order of an aberration the more complex its cause and resulting blur are. As an example, a few of the most

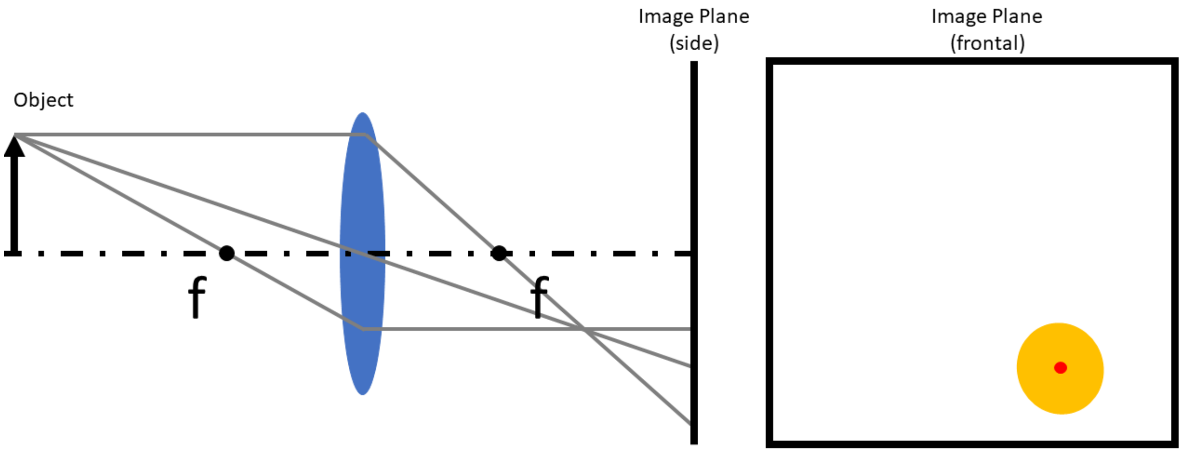

Figure 1.15: Schematic representation of the defocus aberration and the resulting blur. The red dot indicates the aberration-free projection of the point on the image plane.

common aberration types, all low order aberrations, are discussed here. The most common of all aberrations is defocus, which is the result of a mismatch between the point of convergence of the rays and the image plane. This is shown in figure 1.15. As can be observed in the figure defocus leads to smearing out of the point in all directions. However, not all aberrations cause blurs that are (approximately) equal in all direction. An example of an aberration that acts in only a single in-plane direction is astigmatism. Astigmatism is an aberration caused by differences in the lens radius of curvature along the horizontal axis and the radius of curvature along the vertical axis. In figure 1.16 an example of astigmatism is shown. In this example, the rays moving through the vertical plane converge to a point on the image plane, while the rays moving through the horizontal plane converge to a point behind the image plane, resulting in a blur in only the horizontal direction. The presentation of these two types of aberrations serves to convey a basic understanding of the nature of aberrations. While other aberrations will not be discussed here, the wavefront error shapes related to several aberrations are presented in the discussion on Zernike polynomials provided in section 2.1.3.

1.4.2. Aberrations in the DST

The main causes for aberrations in the Deployable Space Telescope after phasing of the M1 segments are expected to be structural vibrations due to on-board excitations and thermal loads. It is anticipated that without correction of these aberrations after phasing the satellite will not be able to achieve diffraction limited performance, characterized by a Strehl Ratio above 0.8 as specified in the requirements. The deployment of the primary and secondary mirrors, in particular, is expected to cause large misalignment errors at the locations of the deployment hinges. For that reason, a calibration strategy has been designed by Dolkens for correction of the position and alignment errors in the M1 mirror segments from within the limits of the *Deployment and Coarse Alignment Budgets* to a point where diffraction limited imaging is possible. This method relies on four piston cams, located at the four gaps between the M1 segments respectively, that measure the wavefront error at the gaps while the mirror segments are displaced to find the positions where the wavefront error is minimum. To quantify the Strehl Ratio increase that can be achieved using this calibration system, a set of Monte Carlo simulations was executed by Dolkens for four different scenarios. The uncalibrated scenario, the calibrated scenario the calibrated scenario including the drift tolerances and the calibrated scenario including the stability tolerances. The figure showing the results of the simulations is presented in figure 1.17. While it should be noted that a significant performance increase is achieved through calibration of the M1 mirror segments, it can also be observed that degradation due to drift and instability - especially the combined degradation which is not shown here - still results in a Strehl Ratio of less than 0.8 in most of the simulations.

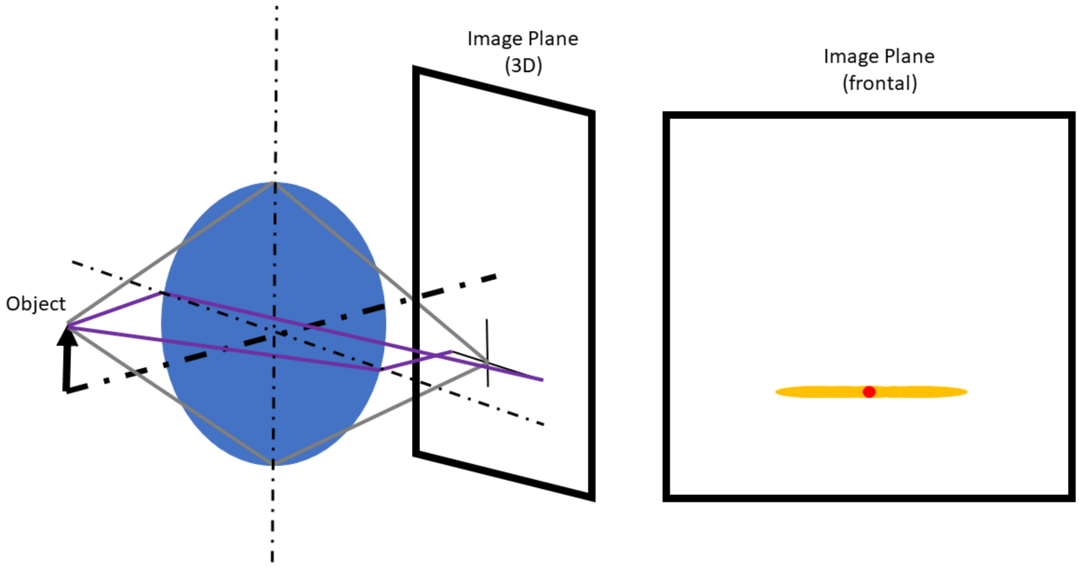

Figure 1.16: Schematic 3D representation of astigmatism due to differences in horizontal and vertical lens radius of curvature.

Thus, additional correction of aberrations is required to meet the requirement that the Strehl Ratio should be consistently above 0.8.

In order to provide an overview of the requirements that the aberration correction system has to comply with, the relevant optical requirements are repeated here:

REQ-1 The Ground Sampling Distance of the instrument shall be equal to 25 cm in the panchromatic band from an orbital altitude of 500 km

REQ-5 The nominal Modulation Transfer Function (MTF) at both the Nyquist frequency and half the Nyquist frequency shall be higher than 5% (threshold) / 15% (goal)

REQ-6 After calibration, the residual Strehl ratio of the system shall be higher than 0.80.

To this list of optical requirements, another relevant requirement has been added by van Marrewijk:

REQ-9 The Root Mean Square error of the wavefront error shall be lower than $0.07\lambda_0$, where $\lambda_0 = 450nm$ is the smallest wavelength accepted by the panchromatic channel

The rationale for this requirement is that a RMS error of $< 0.07\lambda_0$ typically corresponds to a diffraction limited system with a Strehl ratio of > 0.8, as found by Smith [28]. This second, independent figure of merit, has been added for robustness. The reason that these two figures of merit are complementary is explained later in section 2.1.4.

Several possibilities for aberration correction have already been studied in the context of the DST project. These aberration correction strategies can be roughly divided into two categories, methods based on the use of sensors and sensorless methods that estimate aberrations directly from the images. Some research has been done in the field of Shack-Hartmann sensors, a type of sensor that uses an array of lenslets to measure the local error at several locations in the aperture and uses these measurements to construct an estimate of the wavefront error [29] [30] [31] [32]. The wavefront error is a measure of the aberrations in the system. It describes the shape error in the light wave wavefront at the exit of the chain of optical elements. An in-depth discussion on the wavefront is provided in section 2.1.1. A study into the possibility of implementing Shack-Hartmann sensors in the context of the DST has been performed by student Radakrishnan as a part of his MSc graduation project [33]. However, Shack-Hartmann sensors generally have considerable complexity, volume, and mass. Therefore it has been decided by Dolkens to invest resources into the development of aberration correction strategies based on sensorless methods due to the stringent requirements on weight

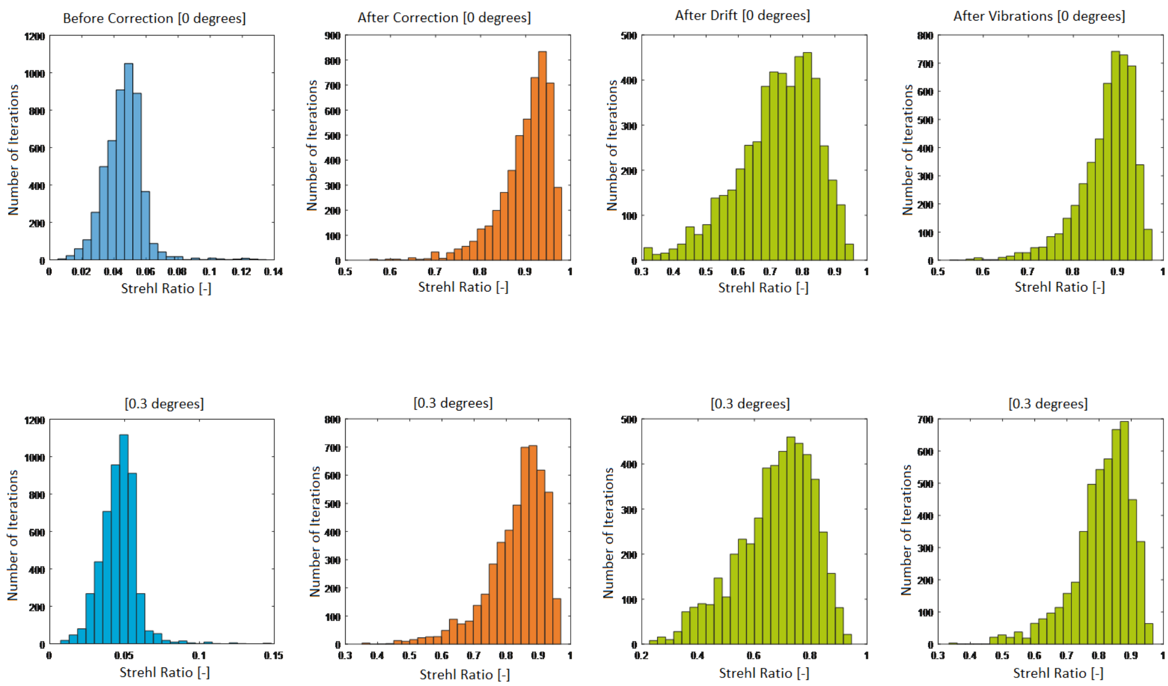

Figure 1.17: Results of the Monte Carlo simulations performed by Dolkens for four different scenarios. Both the central field, light entering the telescope from a cross-track field angle of 0 degrees, as well as the extreme field, light entering the telescope from a cross-track field angle of 0.3 degrees, are shown.

and complexity, the use of sensors would considerably add to both. Following the same reasoning, it was also decided not to use an on-board light source for in-orbit calibration of the instrument. From a trade-off performed by van Marrewijk two general concepts for sensorless aberration sensing have emerged.

1. **Performanc-Based Metrics:** The first concept involves performance metrics that directly assess the quality of the images. An example would be a sharpness metric that judges the quality of the image by the sharpness of the edges. The objective of such a method would be to find the deformable mirror setting that maximizes the performance metric. This type of methods does not directly produce an estimate of aberrations but an estimate can be derived from the DM settings at the maximum metric position

2. **Phase Diversity Algorithms:** The second concept is aberration sensing using a phase diversity algorithm. Phase diversity algorithms originate from the field of ground-based astronomy telescopes and have not been researched extensively in the context of space systems. Even less is known about the performance of these algorithms in the context of EO. EO systems typically involve larger initial aberrations and the imaging of extended scenes instead of point objects such as in astronomy. Phase diversity algorithms use measurements from one or more additional detectors located in the same channel as the primary detector, ideally suffering from exactly the same aberrations. A known aberration, generally defocus, is then added to each of the additional detectors. A phase diversity metric can then be calculated using the detector measurements and an estimate of the wavefront error. Ideally, the value of this metric is independent of the scene under consideration and minimum when the actual wavefront error is used as an input. An optimization algorithm can then aim to find the wavefront error for which the metric value is minimum. The wavefront error can then be used to control a DM, to deconvolute the image in post-processing or a combination of both. The concept of phase diverse wavefront sensing will be further elaborated in section 2.2

A detailed analysis and simulation of multiple performance metric-based methods has already been performed by van Marrewijk.

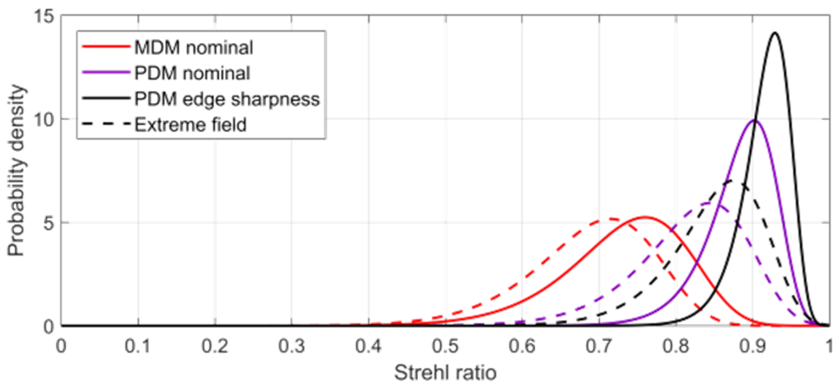

Figure 1.18: Results of a Monte Carlo analysis of the performance of the parallel pertubation stochastic gradient optimization algorithm developed by van Marrewijk using both the MDM and PDM deformable mirror types. Simulations include the effect of the *deployment and coarse alignment* tolerance budget but not the effect of the *drift* tolerance budgets.

1.4.3. Parallel Perturbation Stochastic Gradient Optimization

In van Marrewijk's master thesis it is concluded that, based on simulations, it is probable that a center field Strehl ratio of about 0.9 and an extreme field Strehl ratio of 0.8 can be achieved in most cases using sharpness metrics combined with a Stochastic Gradient Descent algorithm for control of the deformable mirror, even when taking into account the [19] [34]. This parallel perturbation stochastic gradient optimization algorithm (SGD) is called *SharpScan*, and relies on adding small stochastic perturbation to the deformable mirror in the time interval between the imaging of a particular scene by TDI-1 and the imaging of the same scene by TDI-2. For each image, a sharpness metric is evaluated. The difference between the sharpness metric values is used to determine the next stochastic perturbation step. The Strehl ratios resulting from a Monte Carlo analysis of the performance of the algorithm starting from the *Deployment and Coarse Alignment* tolerance budgets but not the *stability* and *drift* tolerance budgets, all listed in table 1.3, are shown in figure 1.18. The terms MDM and PDM indicate two different Deformable Mirror types. As can be observed, the PDM type mirror shows great promise in particular. Figure 1.19 shows the degradation in performance for the MDM mirror type when the *drift* tolerances are added to the simulation.

However, while the method can be used to achieve diffraction-limited imaging, the method also has the disadvantage that convergence can be rather slow, with some simulations requiring over 5 minutes of active run time for convergence. This time does not include the time the satellite is flying over low contrast regions where the algorithm has been shown to be ineffective.

While the results of the SGD sharpness optimizations do show that it is a good candidate for aberration correction and can even be used as initial calibration algorithm after deployment, it would be useful to compare its performance with the performance of phase diversity algorithms, as was suggested by both Dolkens and van Marrewijk. Based on insights gained through studying phase diverse wavefront sensing in the context of the DST, a decision can then be made to either implement SGD sharpness optimization, phase diversity algorithms or a combination of both methods. It is for that reason that phase diverse wavefront sensing for the DST was selected as the subject for this MSc thesis project. The next section will deal with the research questions that this report aims to answer.

1.5. Research Questions

Phase diverse wavefront sensing has been selected as the topic for this thesis project since it could possibly provide a reasonable alternative or addition to the Stochastic Gradient Descent algorithm described by van Marrewijk. Providing an accurate estimate of the increase in performance that can be achieved by implementing a phase diversity algorithm is necessary before a trade-off can be performed between the different aberration correction strategies. Based on this reasoning, the following goal has been formulated:

> *The goal of this thesis project is to determine whether the implementation of Phase Diversity algorithms is a suitable strategy for aberration correction for the Deployable Space Telescope*

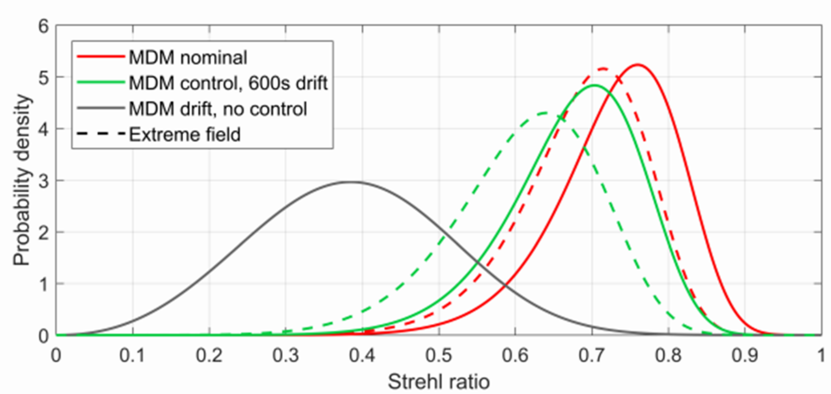

Figure 1.19: Results of a Monte Carlo analysis of the performance of the parallel pertubation stochastic gradient optimization algorithm developed by van Marrewijk. These simulations include the effect of the *drift* and *stability* tolerance budgets on top of the *deployment and coarse alignment* tolerance budgets.

Based on this project goal, several research questions have been formulated that this thesis project will aim to answer.

1.5.1. Primary Research Questions

The primary research question that will be answered in this projects presented here. The question is divided into two subquestions.

1. What is the achievable performance increase when phase diverse wavefront sensing is implemented for the Deployable Space Telescope?
   (a) What is the achievable performance increase in terms of Strehl ratio, resolution, root mean square optical path difference (OPD) and run time when an open-loop phase diversity algorithm is implemented?
   (b) What is the achievable performance increase in terms of Strehl ratio, resolution, root mean square optical path difference and run time when a closed-loop phase diversity algorithm is implemented?

Two key concepts in this project are "open-loop configuration" and "closed-loop configuration". In the context of this thesis, an open-loop configuration is a configuration in which the phase diversity algorithm is executed only once to estimate the wavefront error in the system. The estimate is then used for post-processing of the results, i.e. correcting the images so that details lost through the imaging process can be restored. An open-loop configuration is a configuration in which the estimate of the wavefront error is used to control the active optics, i.e. the DM and the primary mirror segment control mechanism, so that the wavefront error can be actively corrected. This process can be executed in an iterative fashion in order to further reduce the wavefront error in the system [35] [36] [37] [38].

The primary research question represents the engineering dimension of this project, contributing towards the design of an aberration control strategy for the Deployable Space Telescope that is optimum in terms of performance, and cost, and enables the system to meet the optical performance requirements. Answering this question is, therefore, the main goal of this thesis.

1.5.2. Secondary Research Questions

In addition to answering this primary research question, the project also aims to answer two secondary research questions which focus more on the scientific side of phase diversity algorithms:

1. Can the phase diversity algorithm performance be increased by including multispectral channel measurement data in the estimation?

2. Can the phase diversity algorithm performance in the context of Earth Observation be increased by implementing a subframe selection algorithm for determination of the subframe to which the PD algorithm is applied?

Since this project is done at an academic institution, the author has decided to explicitly include an academic dimension, represented by the secondary research questions. These questions cover novel topics in the field of phase diversity, as far as the author is aware, and could provide useful insights not just for the DST but also for other scientific and engineering teams working on phase diversity algorithms for Earth Observation. The motivation behind secondary research question 1 is the presence of the multispectral channels in the DST design. These channels are present regardless of the form of aberration correction that will be implemented. It is therefore interesting to see if the measurements acquired using these channels can be exploited for better PD algorithm performance. Secondary research question 2 has been formulated while the project was already underway. Through preliminary test simulations performed it has been discovered that the phenomena most detrimental to the performance of the phase diversity algorithm are the effects around the edges of the subframe to which the algorithm is applied. These phenomena are explained later in this report. It is hypothesized that the impact of these edge effects can be reduced by selecting a subframe with low intensity at the edges of the frame relative to the intensity at the frame's center.

Since hardware for testing is still unavailable and very expensive, this project aims to find an answer to the research question through end-to-end simulation of the imaging and phase diversity processes. Based on optical and imaging theory a software tool was developed for estimation of the phase diversity performance.

1.6. Chapter Summary

This chapter has outlined the need for the Deployable Space Telescope as well as the project mission and the current state of the design. To increase the temporal resolution and coverage of ultra-high resolution satellites, larger constellations are required. To achieve this the cost of a unit satellite should be reduced. The DST project, a project conceived at TU Delft that involves, students and academic staff members, aims to build a low mass telescope with deployable optics to reduce its launch volume. An optical design for this system has been made by Dolkens [9]. To keep mass and complexity low, the mechanical tolerance budgets are relaxed to such extent that additional correction aberration correction is required in order to meet the optical performance requirements. It was decided that the use of sensors would add too much mass to the system so it has been decided to use sensorless wavefront error estimation. An indirect method based on assessing the relative sharpness of scenes after correction with a DM was developed by van Marrewijk [19]. Although this method shows promise, convergence time is long and it is suggested by Dolkens and van Marrewijk that additional methods are studied as well. Either as an alternative to SGD or as an addition to the method. Another candidate method for wavefront estimation is using either an open-loop or a closed-loop phase diversity algorithm, a method borrowed from the field of ground-based astronomy. Investigating this possibility is the topic of this thesis, which aims to *determine whether the implementation of Phase Diversity algorithms is a suitable strategy for aberration correction for the Deployable Space Telescope* through performing a series of end-to-end simulations of the system. Before the simulation tool and the simulation strategy will be discussed, a summary of the optical theory necessary for understanding phase diversity algorithms is provided in the next chapter.

2

Theory

The last chapter established the need and setup for the DST project, as well as the need and goal for this thesis project. Before the work done is discussed, a summary of the underlying theory will be provided. To understand the concept of phase diversity it is necessary to first understand the imaging process. While it is not required to understand the entire optical chain it is important to understand the relation between the wavefront shape of the light wave in the exit pupil of the system, which is the location of the output of the chain of optical elements, and the intensity distribution in the image plane. To get a better understanding of this relation, a short introduction to Fourier Optics, the branch of optics that deals with the wave nature of light, is given in section 2.1. After a basic understanding is established the discussion moves on to the topic of phase diversity algorithms, the main focus of this project, in section 2.2.

2.1. Fourier Optics

To explain the concept of Fourier Optics, an explanation drawing extensively from the book *Introduction to Fourier Optics* by Goodman is provided [5]. Even though phrasing, order, and symbols may differ, all of the concepts explained in this section are taken from this book except when another source is explicitly mentioned. Images are provided by the author of this report unless mentioned otherwise.

2.1.1. Imaging

As a starting point, a general schematic representation of an optical channel is presented in figure 2.1. In this figure, the box represents an arbitrary chain of reflective and/or refractive optical components that together make up the optical channel manipulating the incoming light waves. As can be observed from the figure there are four planes that are of interest. The first plane is the object plane where the object that is being imaged is located. Positions in the object plane are indicated with the (ξ,η) coordinates. Light waves enter the optical channel via the entrance pupil and leave the optical channel via the exit pupil. These pupils are the images of the aperture as seen from the object plane and the image plane respectively. Since both pupils are an image of the same aperture, only a single set of coordinates (x, y) is needed to indicate the position in the pupil plane. After leaving the exit pupil of the system light is captured by a detector located in the image plane. Image plane position is indicated with the (u, v) coordinates.

First, to obtain a basic understanding of the imaging process, a monochromatic light source, i.e. emitting light at a single wavelength, of wavelength λ is assumed, with all incident light rays approximately parallel to the optical axis. The optical axis is the axis perpendicular to the pupil plane, going through the center point of the pupil. When this is the case there is a time-invariant phase difference between any two points in the electromagnetic field. This type of light, schematically represented in figure 2.2 is called coherent light. For light to be coherent it should satisfy the condition of spatial coherence, a constant phase difference between any two points along the transverse directions of a wave, and temporal coherence, a constant phase difference between any two points along the propagation direction of a wave. The latter is satisfied when the light is monochromatic.

If the light is coherent and consequently the phase differences are invariant, the EM field can be described in terms of just the amplitude distribution U at each point in space. Assuming an amplitude distribution

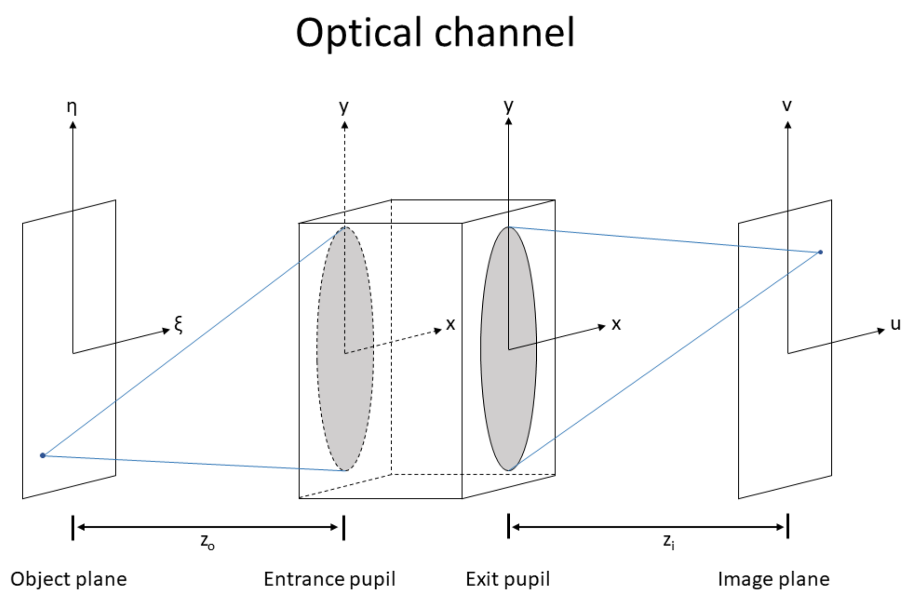

Figure 2.1: Schematic representation of an optical channel. Adapted from Goodman [5].

$U_o(\xi,\eta)$ in the object plane, the amplitude distribution in the focal plane can be expressed as shown in equation (2.1).

$$U_i(u,v) = \iint_{-\infty}^{\infty} h(u,v;\xi,\eta)U_o(\xi,\eta)\mathrm{d}\xi\mathrm{d}\eta \tag{2.1}$$

In this equation the function $h(u,v;\xi,\eta)$ is called the Coherent Point Spread Function (PSF) that describes how the field strength originating from object plane coordinates (ξ,η) is spread out over the image plane. For an aberration-free and space invariant imaging system, meaning aberrations and distortions are independent of the light source location (ξ,η) in the object plane, with magnification M this coherent point spread function is described by equation (2.2).

$$h(u,v;\xi,\eta) = h(u-M\xi, v-M\eta) = \frac{1}{\lambda^2 z_o z_i}\iint_{-\infty}^{\infty} P(x,y)\exp\left[-i\frac{2\pi}{\lambda z_i}[(u-M\xi)x+(v-M\eta)y]\right]\mathrm{d}x\mathrm{d}y \tag{2.2}$$

Here $P(x,y)$ is the pupil function related to the shape of the aperture. $P(x,y)$ has a value of 1 at locations in the pupil plane where light passes through and 0 at locations where light does not pass through. Furthermore, i indicates the imaginary unit. To simplify this relation, the entity $U_g(u,v)$ presented in equation (2.3) can be introduced, which is the amplitude distribution in the image plane predicted by aberration-free geometrical optics.

$$U_g(u,v) = \frac{1}{|M|}U_o\left(\frac{u}{M},\frac{v}{M}\right) \tag{2.3}$$

Then, using the changes of variables provided in equation (2.4) and substituting (2.3) into equation (2.1) equation (2.5) is acquired.

$$\bar{\xi} = M\xi\,;\ \bar{\eta} = M\eta\,;\ \bar{x} = \frac{x}{\lambda z_i}\,;\ \bar{y} = \frac{y}{\lambda z_i} \tag{2.4}$$

$$U_i(u,v) = \iint_{-\infty}^{\infty} h(u-\bar{\xi}, v-\bar{\eta})\left[\frac{1}{|M|}U_o\left(\frac{\bar{\xi}}{M},\frac{\bar{\eta}}{M}\right)\right]\mathrm{d}\bar{\xi}\mathrm{d}\bar{\eta} = \iint_{-\infty}^{\infty} h(u-\bar{\xi}, v-\bar{\eta})U_g\left(\bar{\xi},\eta\right)\mathrm{d}\bar{\xi}\mathrm{d}\bar{\eta} \tag{2.5}$$

Note that the scaling factor $|M|$ has been omitted here since in most application only the shape of interest and not the exact scaling. For the same reason, the scaling factor $\frac{1}{\lambda^2 z_o z_i}$ will be omitted for the Coherent

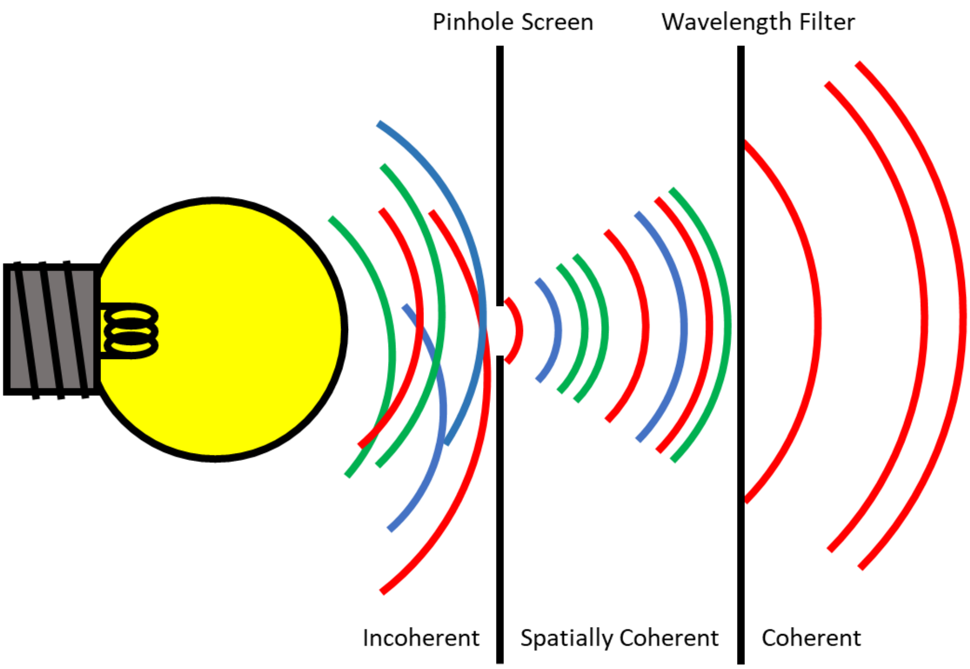

Figure 2.2: Schematic representation of coherence in light waves.

PSF $h(u,v)$ from now on. That the shape is irrelevant, is also true in the case of thesis project. It can be observed that the expression provided in equation (2.5) is the convolution between the coherent Point Spread Function $h(u,v)$ and the amplitude distribution in the image plane as predicted by geometric optics $U_g(u,v)$. A shorthand notation of this expression using the convolution operator is provided in equation (2.6).

$$U_i(u,v) = h(u,v) * U_g(u,v) \tag{2.6}$$

It is convenient to express the coherent PSF $h(u,v)$ in the spatial frequency domain, since the convolution from equation (2.6) can be solved by multiplication in the frequency domain, as observed in equation (2.7).

$$G_i(f_X, f_Y) = H(f_X, f_Y) G_g(f_X, f_Y) \tag{2.7}$$

Here G_i and G_g indicate the Fourier transforms of U_i and U_g respectively. The variables f_X and f_Y indicate the image plane spatial frequencies in the u and v directions, respectively. It should be noted that he Coherent Point Spread Function $h(u,v)$ is simply a Fourier transform of a scaled version of the Pupil function. Therefore the Fourier transform $H(f_X, f_Y) = \mathscr{F}\{h(u,v)\}$, called the Coherent Transfer Function (CTF), is simply a scaled version of the pupil function as shown in equation (2.8). This makes the calculation of the CTF from the pupil shape very convenient process.

$$H(f_X, f_Y) = \mathscr{F}\{h(u,v)\} = P(-\lambda z_i f_X, -\lambda z_i f_Y) \Rightarrow P(\lambda z_i f_X, \lambda z_i f_Y) \tag{2.8}$$

It is also assumed that the pupil is symmetric in both the X and Y directions so that the minus signs can be dropped, an assumption that is true for the aperture of the DST.

So far the light has been assumed to be coherent. While some light, most notably lasers or light originating from bright, far away point sources like the sun, is approximately coherent, most light sources are not. Especially extended scenes like the ones imaged by earth observation satellites display very low levels of coherence. In incoherent light, the correlation between the phases at different locations breaks down, and interference patterns cannot be observed anymore. In these cases, it is only possible to measure the intensity of the light. Any information about the phase of the wavefront in the pupil is lost. The intensity point spread function $s(u,v)$ can be expressed in terms of the coherent PSF as shown in equation (2.9).

$$s(u,v) = |h(u,v)|^2 = |\mathscr{F}\{H(f_X, f_Y)\}|^2 \tag{2.9}$$

Figure 2.3: Noisy image of Delft taken from wikipedia, photograph taken by Remi Jouan [6].

The Fourier transform of the PSF $S(f_X, f_Y) = \mathscr{F}\{s(u,v)\}$ is called the Optical Transfer Function (OTF) and can be expressed as the autocorrelation of the coherent transfer function $H(f_X, f_Y)$ as shown in equation (2.10).

$$S(f_X, f_Y) = H(f_X, f_Y) \star H(f_X, f_Y) \tag{2.10}$$

The intensity distribution in the image plane can then be expressed as shown in equation (2.11) (image domain) and equation (2.12) (frequency domain).

$$i_i(u,v) = s(u,v) * i_g(u,v) \tag{2.11}$$

$$I_i(f_X, f_Y) = S(f_X, f_Y) * I_g(f_X, f_Y) \tag{2.12}$$

Here, i_g denotes the intensity distribution as predicted by aberration-free geometrical optics and i_i the actual intensity distribution in the image plane taking into account diffraction.

Up until now, the assumption was made that the optical channel was free of aberrations and noise. In real-world applications, the imaging process is always degraded by noise. An example of an image degraded by Gaussian distributed imaging noise is presented in figure 2.3. Imaging noise can originate from many different sources and is not necessarily Gaussian distributed. This will be further elaborated on in section 3.1.2. The incoherent imaging of an object using a detector suffering from additive noise can be expressed as shown in equation (2.13).

$$i(u,v) = s(u,v) * o(u,v) + n_i(u,v) = g(u,v) + n(u,v) \tag{2.13}$$

It must be noted that here, and from now on $i(u,v)$ is used to indicate an intensity measurement in the image plane, $o(u,v)$ is the ideal geometric projection of the object on the image plane and $n(u,v)$ is the measurement noise. $g(u,v) = s(u,v) * o(u,v)$ is then used to indicate the noiseless but aberrated projection of the object on the detector. In the Fourier domain, this can be expressed as shown in equation (2.14).

$$I(f_X, f_Y) = S(f_X, f_Y)O(f_X, f_Y) + N(f_X, f_Y) \tag{2.14}$$

This concludes the discussion of aberration-free imaging, the next section will return to the topic of aberrations and the modeling of an optical channel degraded by aberration using Fourier optics.

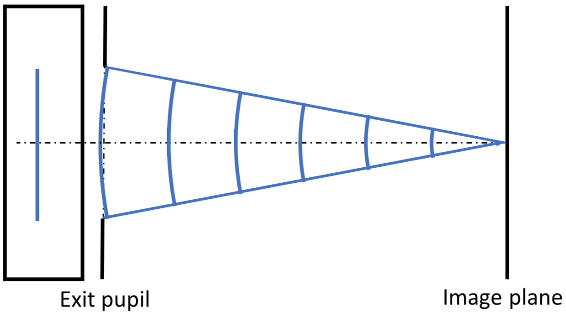

(a) Ideal optical system.

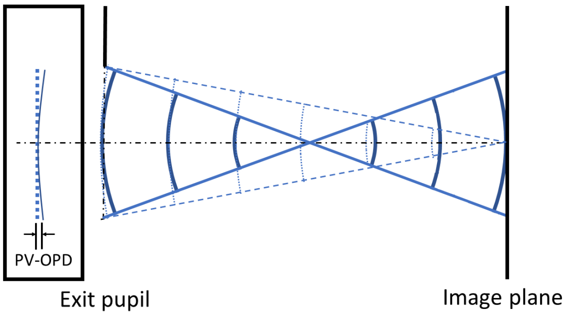

(b) Optical system in which a defocus aberration is present.

Figure 2.4: Schematic 2D representation of the wavefront in an ideal system and the wavefront in a system in which a defocus aberration is present.

2.1.2. Optical Path Difference

Up to this point, aberrations have only been discussed in the context of geometrical optics. Geometrical optics describe aberrations in terms of the locations where light rays hit the image plane. In contrast, Fourier optics describes aberrations in terms of the wavefront error in the exit pupil of the system. This is shown in figure 2.4. In this figure, two scenarios are presented. Figure 2.4a shows an unaberrated system where the wavefront is perfectly spherical with a radius such that the wave converges into a single point on the focal plane of the system. Note that the direction of propagation is perpendicular to the wavefront at every point. Figure 2.4b shows a system in which a defocus aberration is present. While the wavefront is still spherical the radius of the wavefront is too small resulting in convergence to a point which is located in front of the focal plane. In general, Fourier optics describes aberrations as deviations from the ideal spherical wavefront that converges to a single point on the image plane. For convenience, aberrations are usually defined as the optical path difference in the exit pupil of the system. As an example the peak-to-valley (PV) OPD value for the defocus aberration is presented on the left side in figure 2.4b.

In order to include the effect of aberrations into the Coherent Transfer Function, Optical Transfer Function and Point Spread Function, the OPD should first be expressed in the form of a wavelength-dependent phase difference $\theta(x,y)$, called the wavefront error. The relation between this phase difference and the OPD is provided in equation (2.15)

$$\theta(x,y) = \frac{2\pi}{\lambda}\mathrm{OPD}(x,y) \tag{2.15}$$

in this equation, the OPD is expressed in metres. The aberrated CTF can then be determined by multiplying the pupil function with a complex term $\exp\left[j\theta(x,y)\right]$ containing the wavefront error $\theta(x,y)$ expressed in radians. This leads to the coherent transfer function shown in equation (2.16).

$$H(f_X,f_Y) = P(\lambda z_i f_X, \lambda z_i f_Y)\exp\left[j\theta(\lambda z_i f_X, \lambda z_i f_Y)\right] \tag{2.16}$$

For the remainder of this report, a capital letter variable indicates the Fourier transform of a lower case variable unless indicated otherwise. For conciseness, the dependency of the variables described above will often be omitted. In summary, the intensity PSF can be calculated when the wavefront error is known. However, due to the incoherence of the light, phase information is lost in the process. This means that it is often difficult or impossible to estimate the original wavefront error when just the PSF is known since several wavefront errors can correspond to the same PSF.

2.1.3. Zernike Polynomials

For computational convenience and efficiency, it is generally desired to express the wavefront error $\theta(x, y)$ as a sum of basis functions rather than as a collection of individually defined data points. (2.17). A proper set of basis functions meets two criteria:

1. It can describe the distribution of interest with as little parameters as possible.
2. It is robust to overfitting of the data. Overfitting means that the all small peaks and troughs caused by noise or other perturbations are fitted as well, resulting in a loss of accuracy.

A set of basis function that is particularly well suited for the construction of wavefront errors is the set of Zernike polynomials, developed by Frits Zernike [39] [7]. The reason for this is that the shapes of the most common wavefront aberration types all have a corresponding Zernike polynomial that describes their shape. This significantly limits the number of basis functions required for an accurate wavefront error construction if the amount of higher order aberrations in the system is limited, as is the case in most imaging systems. Using Zernike polynomials, the wavefront error can be expressed using a set of wavefront coefficients $\{\alpha_j\}$. A construction of the wavefront error can be produced with these coefficients as shown in equation (2.17).

$$\theta(x, y) = \sum_{j=1}^{J} \alpha_j Z_j(x, y) \tag{2.17}$$

In this equation the Z_j terms amounting to J terms in total are the individual Zernike polynomials, the index j refers to the Noll index of each polynomial [40]. Each individual Zernike polynomial can be expressed as shown in equation (2.18), where m is the azimuthal frequency of the Zernike polynomial and n is the radial order of the Zernike polynomial.

$$\begin{aligned} Z_n^m(r,\theta) &= R_n^m(r)\cos(m\theta) \text{ for } m \geq 0 \\ Z_n^{-m}(r,\theta) &= R_n^m(r)\sin(m\theta) \text{ for } m < 0 \end{aligned} \tag{2.18}$$

The expression for R_n^m is then given by Equation (2.19).

$$R_n^m(r) = \sum_{l=0}^{\frac{n-m}{2}} \frac{(-1)^l (n-l)!}{l! \left[\frac{1}{2}(n+m) - l\right]! \left[\frac{1}{2}(n-m) - l\right]!} r^{n-2l} \tag{2.19}$$

The relation between the Noll term used in equation (2.17) and the m and n terms used in equation (2.18) is presented in tabular form in table 2.1. The Zernike modes up to radial order 10 are shown in Figure 2.5. This figure also provides some of the names of the most common types of phase aberration associated with specific Zernike polynomials. Overfitting of the wavefront error can be prevented by using only Zernike polynomials up to the highest order that corresponds to types of aberrations present in the wavefront error.

Table 2.1: Relation between n and m indices and Noll indices.

n,m	0,0	1,1	1,-1	2,0	2,-2	2,2	3,-1	3,1	3,-3	3,3
j	1	2	3	4	5	6	7	8	9	10
n,m	4,0	4,2	4,-2	4,4	4,-4	5,1	5,-1	5,3	5,-3	5,5
j	11	12	13	14	15	16	17	18	19	20

2.1.4. Strehl ratio and RMS error

One concept from Fourier optics that is used for assessing the quality of a certain optical system of optical algorithm performance is the Strehl ratio [41]. The Strehl ratio is a measure of the severity of the blur caused by aberrations in an optical system and is calculated by taking the ratio between the peak value of the actual PSF of the system and the peak value of the diffraction-limited PSF of a system with the same aperture, but no aberrations. This is mathematically expressed in equation (2.20)

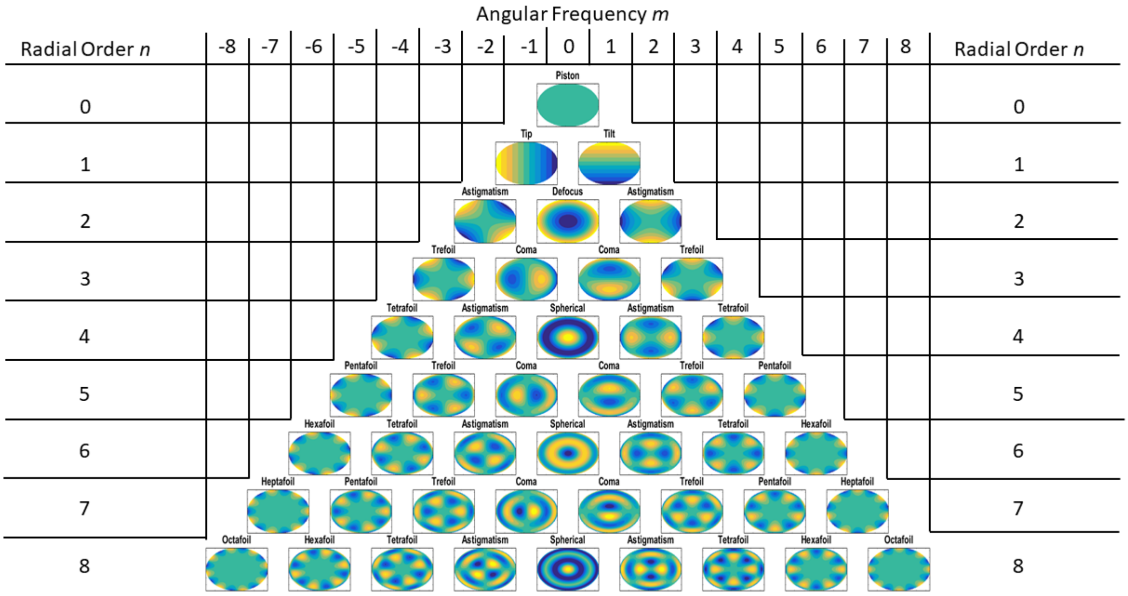

Figure 2.5: The Zernike modes up to order 8. Adapted from [7].

$$SR = \frac{max[s(u,v)]}{max[s_{aberration-free}(u,v)]} \tag{2.20}$$

A graphic representation of the Strehl ratio is presented in figure 2.6. Generally, when the Strehl ratio of a system is above 0.8 aberration effects do not noticeably affect the quality of the images, and the system is thus considered to be diffraction-limited. This is also from which **REQ-6** listed in section 1.2 is derived. The Strehl ratio is as an important figure of merit throughout this report.

A second figure of merit that is used throughout this project is the Root Mean Square of the wavefront error. The RMS value is computed by calculating the square of the wavefront error at every location after which all squares are summed and subsequently divided by the number of data points. The last step in calculating the RMS is taking the root of the mean of the squares resulting in the Root Mean Square. This is presented mathematically in equation (2.21).

$$\text{RMS} = \sqrt{\frac{1}{N}\sum_{n=1}^{N} x_n^2} \tag{2.21}$$

In this equation, N is the number of data points and x_n is the function value at the n-th data point. The Strehl ratio and the RMS are complementary figures of merit. The Strehl ratio, which is a measure of the amount of energy concentrated in the center of the PSF, is strongly correlated with the resolution and sharpness of the image. However, the Strehl ratio is not necessarily a perfect measure of the accuracy of the wavefront estimation, since multiple wavefronts can result in similar Strehl ratios. The RMS is a very accurate measure of the accuracy of the wavefront estimation, but a wavefront with a high RMS error might still result in acceptable image quality since not all aberration shapes cause large image blurs. In summary, the SR measures the PSF quality and the RMS measures the wavefront estimation accuracy.

Taking the concepts from Fourier optics described above, it is now possible to present a quantitative description of phase diversity algorithms.

2.2. Phase Diversity Algorithms

Determining the Point Spread Function of an optical channel when a small object, approximating a point source is imaged, is relatively straightforward. One just has to look at the blur resulting from the imaging of the single point, which directly provides the PSF of the system. This PSF can then be used to deconvolve any

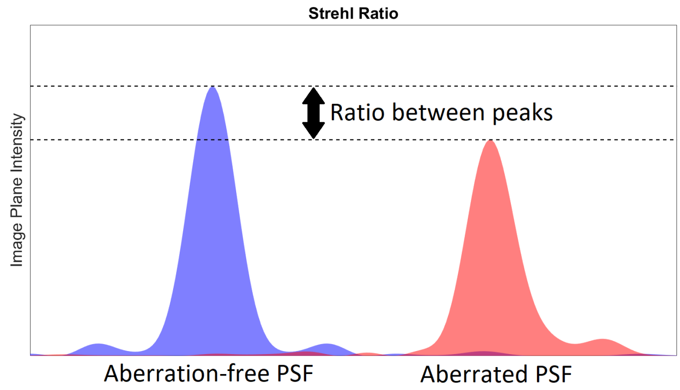

Figure 2.6: Graphical representation of the Strehl ratio calculation using the aberration-free PSF and the actual, aberrated PSF of the optical system.

subsequent images with the intention of constructing a more accurate estimate of the object that is being imaged. In the case of Earth observation, however, extended scenes are being imaged instead of point sources. The detailed composition of these scenes is unknown and therefore cannot be used for derivation of the PSF. A possible solution to this would be calibration with a phase retrieval algorithm using a point source like a star [42]. This would, however, require the satellite to rotate, which would require additional complexity in the design and possibly introduce additional misalignments and inaccuracies in the positions of the optical elements due to the movement. Therefore, this strategy is determined to be infeasible in the case of the DST, and thus a different method is required to determine the exact shape of the image blur.

To solve the problem of the unknown object, Robert Gonsalves proposed 1982 to use a second, out-of-focus, detector image to obtain an out of focus "diversity image" of the same object using the same optical channel [43]. These images would then suffer from the same aberrations, except for a known defocus aberration found in the diversity image. Gonsalves' work shows that it is possible to then find a Least-Squares objective metric that is independent of the object and depends only on the aberration coefficients. Using an optimization routine this metric can then be used to estimate the phase aberrations. While the out of focus image could be a time delayed image of the same scene taken with the same detector after it is displaced by a known distance along the optical axis, a technique called sequential diversity imaging, this is often impractical if not impossible for Earth Observation satellites that take images at high speed [44] [45]. Therefore, from now on it will be assumed that the second image is produced by a separate detector located in the same optical channel.

2.2.1. Reduced Gaussian Metric

To derive such an objective metric, one should first obtain some knowledge of the dominant type of noise affecting the detector signal. In an imaging system, this is usually either Poisson distributed Shot noise or Gaussian white noise. The method developed by Gonsalves can be adapted for both systems with Gaussian noise as well as systems with Poisson noise. However, as described by Dolkens the noise present in the case of the DST can safely be approximated using a Gaussian white noise model [46]. The reason for this is that extended scenes are imaged in daylight conditions. This leads to very high signal values at the detector. Even if Poisson noise would be dominant in this situation, for high signal values a Poisson distribution is virtually identical to a Gaussian distribution. The Gaussian noise version of the phase diversity algorithm allows for much easier computation of the gradients than the Poisson version, which makes the optimization process much less computationally intensive [47]. Therefore the following discussion will focus on the Gaussian metric.

Gonsalves' originally derived an object independent metric for the case of a two detector system with a single in-focus image and a single out-of-focus diversity image. Later, through the work of James Fienup and Richard Paxman, this metric was generalized to incorporate an arbitrary number of diversity images [48]. The derivation of the metric below is based on the derivation presented by Fienup and Paxman. In case of K detector planes corrupted by Gaussian noise, the probability of obtaining a specific set of intensity measurements $\{i_k(u,v)\}$ can be expressed as shown in equation (2.22).

$$Prob(\{i_k(u,v)\}; o(u,v); \alpha) = \prod_{k=1}^{K} \prod_{u,v} \frac{1}{\sqrt{2\pi\sigma_n^2}} \exp\left[\frac{(i_k(u,v) - g_k(u,v))^2}{2\sigma_n^2}\right] \tag{2.22}$$

In this equation σ_n^2 indicates the variance of the noise, the other variables are explained in section 2.1.1. Also, note that the coordinates u and v are not continuous in this case, instead they are integers indicating the pixel indices. If the natural logarithm of equation (2.22) is taken one arrives at equation (2.23).

$$L(\{i_k(u,v)\}; o(u,v); \alpha) = -\sum_{k=1}^{K} \sum_{u,v} \frac{1}{2} \ln[2\pi\sigma_n^2] + \frac{1}{2\sigma_n^2} [i_k(u,v) - g_k(u,v)]^2 \tag{2.23}$$

The inconsequential addition term that does not depend on the wavefront error and an inconsequential factor that does not influence the shape of the metric function can be omitted. Additionally writing $g_k(u,v) = s_k(u,v) * o(u,v)$ one arrives at the least squares estimator shown in equation (2.24).

$$L = \sum_{k=1}^{K} \sum_{u,v} [i_k(u,v) - \hat{s}_k(u,v) * \hat{o}(u,v)]^2 \tag{2.24}$$

In this equation and for the remainder of this report, a hat above a variable indicates an estimate of a parameter. Using Parseval's theorem this equation can be rewritten to a Fourier domain expression as shown in equation (2.25).

$$L = \sum_{k=1}^{K} \sum_{f_X, f_Y} \left[I_k(f_X, f_Y) - \hat{S}_k(f_X, f_Y)\hat{O}(f_X, f_Y)\right]^2 \tag{2.25}$$

To arrive at an object independent metric, this metric can be minimized with respect to the ideal object projection estimate $\hat{O}$ by differentiating with respect to $\hat{O}$ and setting the derivative to zero. This leads to an expression for $\hat{O}$ shown in equation (2.26). For convenience, all dependencies have been omitted.

$$\hat{O}_M = \begin{cases} \sum_{f_X, f_Y} \frac{\sum_{k=1}^{K} I_k \hat{S}_k^*}{\sum_{l=1}^{K} |\hat{S}_k|^2}, & \sum_{l=1}^{K} |\hat{S}_l|^2 \neq 0 \\ 0, & \sum_{l=1}^{K} |\hat{S}_l|^2 = 0 \end{cases} \tag{2.26}$$

The subscript M indicates that this expression minimizes the least squares expression. The superscript $*$ indicates the complex conjugate. The final step in the derivation of the metric is substituting equation (2.26) back into equation (2.25) which leads to equation (2.27).

$$L_M = \sum_{(f_X, f_Y) \in \chi} \sum_{k=1}^{K} |I_k|^2 - \sum_{(f_X, f_Y) \in \chi} \frac{|\sum_{l=1}^{K} I_l \hat{S}_l^*|^2}{\sum_{m=1}^{K} |\hat{S}_m|^2} \tag{2.27}$$

In this equation χ indicates the set of frequency pairs (f_X, f_Y) at which the term $\sum_{m=1}^{K} |\hat{S}_m|^2$ does not sum to zero. Omitting the frequencies where the sum of the absolute values of the OTFs sum to zero also has the added benefit of regularizing the metric, i.e. nothing but noise is expected at those spatial frequencies and omitting these spatial frequencies effectively filters noise out of the summation.

As can be observed, this metric only depends on the detector measurements and the set of OTF estimates $\{\hat{S}_k\}$ for the K detectors, which makes this metric much more useful for imaging unknown, extended objects as is the case in earth observation applications. This particular form of the Gonsalves metric, unregularized except that frequencies where all squared OTF moduli sum to zero are omitted, is called the Reduced Gaussian (RG) metric. As can be observed, the L_M metric will reduce to zero if either $K = 1$ or if the Optical Transfer Functions and consequently the measurements are identical for the different detectors. Therefore a known error ϕ_k, different for each individual detector k, has to be introduced. As a result, the Coherent Transfer Function of each detector can be expressed as shown in equation (2.28).

$$H_k(f_X, f_Y) = P(\lambda z_i f_X, \lambda z_i f_Y) \exp[j[\theta(\lambda z_i f_X, \lambda z_i f_Y) + \phi_k \lambda z_i f_X, \lambda z_i f_Y]] \tag{2.28}$$

Typically, this additional, known aberration is a defocus error generated by slightly displacing each detector along the optical axis. In most applications, two detectors are used for phase diversity algorithms, which means $K = 2$, where for one detector $\phi_k = 0$ and for the other detector $\phi_k \neq 0$. This will also be the case for the Deployable Space Telescope project. Since the relationship between the different OTFs $\{S_k\}$ is solely dictated by the known errors $\{\phi_k\}$, they do not have to be estimated independently. Only a single wavefront error, usually the OTF of the in-focus image with $\phi_k = 0$, is estimated and all other wavefront errors are calculated from this wavefront by adding the known errors. Estimation is done by estimating the coefficients corresponding to a set of basis functions, usually a set of Zernike polynomials.

Now that a first version of the optimization objective function is derived, it is interesting to take a closer look at the properties of the RG metric. In the next subsection, a method will be shown to derive an analytic expression for the gradient that can be used as an input for gradient-based optimization methods.

2.2.2. Gradient of the Reduced Gaussian metric

An analytic method for calculation of the gradient of the Reduced Gaussian method is presented by Paxman et al. [48]. Given a set of measurements and a set of basis functions, the goal of the optimization is to minimize the value of the RG metric provided in Equation (2.27) by finding the right weights α_j for the basis functions Z_j that together make up the phase aberration as shown in equation (2.17). It is thus interesting to find the gradients of L with respect to these parameters α_j. This is expressed mathematically in Equation (2.29).

$$\frac{\partial}{\partial \alpha_j} L_M^{RG} = \frac{\partial}{\partial \alpha_j} \sum_{(f_X, f_Y) \in \chi} \sum_{k=1}^{K} |I_k|^2 - \frac{\partial}{\partial \alpha_j} \sum_{(f_X, f_Y) \in \chi} \frac{|\sum_{l=1}^{K} I_l \hat{S}_l^*|^2}{\sum_{m=1}^{K} |\hat{S}_m|^2} \tag{2.29}$$

Since only the estimates of the Optical Transfer Functions $\hat{S}_k$ depend on the parameters α_j, the first term can be omitted, which leaves only the second term. In the following derivation, only a few important steps are shown, the rest can be found in the article by Paxman et al. [48]. The derivative of the second term can be expressed as shown in Equation (2.30) using elementary calculus of complex numbers.

$$-\frac{\partial}{\partial \alpha_j} \sum_{(f_X, f_Y) \in \chi} \frac{|\sum_{l=1}^{K} I_l \hat{S}_l^*|^2}{\sum_{m=1}^{K} |\hat{S}_m|^2} = \left(- \sum_{(f_X, f_Y) \in \chi} C_k \hat{S}_k' \right) + c.c. \tag{2.30}$$

Here the apostrophe indicates the derivative with respect to α_j. The variable $c.c$ denotes the complex conjugate of the first term. The variable C_k is given by Equation (2.31).

$$C_k(f_X, f_Y) \equiv \begin{cases} \frac{\left[\sum_{l=1}^{K} |\hat{S}_l|^2 (\sum_{m=1}^{K} I_m \hat{S}_m^*) I_k^* - |\sum_{n=1}^{K} I_n \hat{S}_n^*|^2 \hat{S}_k^*\right]}{\left(\sum_{q=1}^{K} |\hat{S}_q|^2\right)^2}, \ (f_X, f_Y) \in \chi \\ 0, \ (f_X, f_Y) \notin \chi \end{cases} \tag{2.31}$$

Here, dependency on u has been dropped for convenience of notation. The next step in determining the gradient is finding an expression for the derivative of $\hat{S}_k$ with respect to α_j. Noticing that S_k can be written as the discrete autocorrelation of the Coherent Transfer Function H as was shown in equation (2.10) and $\hat{H}_k$ can be written as shown in Equation (2.32).

$$H_k(f_X, f_Y) = P(\lambda z_i f_X, \lambda z_i f_Y) \exp \left[j \left(\phi_k \lambda z_i f_X, \lambda z_i f_Y + \sum_{j=1}^{J} \alpha_j Z_j (\lambda z_i f_X, \lambda z_i f_Y) \right) \right] \tag{2.32}$$

Using these equations the derivative can be written as shown in Equation (2.33).

$$\frac{\partial}{\partial \alpha_j} \hat{S}_k(f_X, f_Y) = \frac{j}{N^2} \sum_{f_X', f_Y' \in \chi} Z_j(\lambda z_i f_X', \lambda z_i f_Y') [H_k(f_X', f_Y') H_k^*(f_X' - f_X, f_Y' - f_Y) - H_k^*(f_X', f_Y') H_k(f_X' + f_X, f_Y' + f_Y)] \tag{2.33}$$

Here the term N is the number of samples/pixels in a single dimension assuming a square grid. The term originates from the expression of the discrete representation of the autocorrelation operation. Substituting equation (2.33) back into Equation (2.30) and performing some rearrangements and substitutions of variables, an analytic expression for the gradient is found, which is shown in Equation (2.34).

$$\frac{\partial}{\partial \alpha_j} L_M^{RG} = \frac{4}{N^2} \sum_{f_X', f_Y' \in \chi} Z_j(\lambda z_i f_X', \lambda z_i f_Y') \mathrm{Im} \left[\sum_{k=1}^{K} H_k(f_X' - f_X, f_Y' - f_Y)(C_k * H_k^*)(f_X', f_Y') \right] \tag{2.34}$$

This expression for the gradient provides the basis for the use of gradient-based optimization strategies for finding the minimum of the RG metric.

Since the concept was invented by Gonsalves, myriad research has been performed in the field of phase diversity algorithms. However, the fundamental theory behind these algorithms has not changed. Therefore, no additional examples of phase diversity metrics are presented here. However, in chapter 3 an elaborate discussion on the metric used in this project will be presented.

2.3. Chapter Summary

In this chapter, the necessary theory for understanding the working principles of phase diversity algorithms as well as an early example of a phase diversity algorithm was discussed. It was shown that using Fourier optics a quantitative description of the relation between the wavefront error in the exit pupil and the PSF, which describes the image blur shape, can be established. The larger the wavefront error differences along the wavefront of the light wave the larger the resulting blur in the image plane. While the PSF can be calculated from the wavefront error, phase information is lost in the process in the light source incoherent. In the case of EO the light source is always incoherent. Therefore calculating the wavefront error from the PSF is often difficult or impossible since typically, several wavefront errors could result in the same PSF. Typical wavefront error shapes are called wavefront aberrations. An efficient way of describing the wavefront error is in terms of Zernike polynomials, a set of 2D shape functions that correspond very well to the shape of wavefront aberrations commonly encountered in optical systems. Two effective ways of estimating the severeness of a wavefront error are introduced. The first is the Strehl ratio, which compares the severity of the blur to that of an ideal system. The second is the wavefront error RMS which is a measure of how much the error shape deviates from a flat wavefront. Phase Diversity algorithms, first described by Gonsalves, exploit the relation between the wavefront error and image blur [43]. Phase Diversity algorithms aim to find a wavefront error shape that minimizes a particular phase diversity metric, which is calculated based on a single in-focus detector measurements and a set of diversity detector measurements from the same channel to which know wavefront aberrations, typically defocus aberrations, have been added. Theoretically, the wavefront error that minimizes the metric corresponds to the actual wavefront error in the exit pupil of the system. For most phase diversity metrics an analytic gradient expression exists, which allows for the application of gradient-based optimization methods for finding the minimum. Now that the necessary theory has been established, the next chapter will discuss the end-to-end simulation tool that will be used for simulation of the phase diversity algorithms. The chapter will discuss both how simulation of the system will be performed and which phenomena will be taken into account, as well as the possible phase diversity algorithm configurations that will be integrated into the tool.

3

Phase Diversity Simulation Tool

The previous chapter discussed the theory behind Fourier optics and phase diversity algorithms necessary to understand the thesis topic. This chapter elaborates on the software that was used to answer the research questions. To obtain an estimate of the performance increase that can be achieved for the Deployable Space Telescope through the implementation of Phase Diversity, an end-to-end simulation tool was developed to be used as a test bench. Using this tool a large number of Phase Diversity algorithm configurations, borrowing features from a broad range of methods in the field of imaging theory, were tested in order to asses their performance in the context of the DST design. A schematic overview of the tool architecture is presented in figure 3.1. As can be observed the simulation tool consists of two distinct subroutines. The first subroutine simulates the imaging process on board the Telescope, taking hyperspectral image data as input and providing a detector measurement data array for every simulated detector as output. These simulated measurements are then used as an input for the second subroutine, the Phase Diversity algorithm. The PD algorithm consists of a gradient-based optimization routine that estimates the wavefront error present in the pupil of the panchromatic channel, and a deconvolution algorithm that aims to reconstruct the original scene imaged by the DST using the final estimate of the wavefront error.

The simulation tool was implemented in MATLAB since simulation of the DST optics is performed using the Fast Optical Ray Trace Application (FORTA) tool developed at Delft University of Technology by Dennis Dolkens [10]. The FORTA ray-tracing tool, which includes a complete geometric model of all the DST optical channels, was also implemented in MATLAB. This allowed for a convenient interface between the two software tools. In section 3.1 and section 3.2 respectively, the two subroutines are discussed in more detail.

3.1. Simulating Imaging for the DST

To maximize the accuracy of the tool the imaging simulation takes into account as many real-world physical phenomena that could influence the imaging process as possible without driving computation time to an unacceptable level. The most significant phenomena that were selected for implementation are:

1. A polychromatic light source
2. The field separation between the detectors
3. An unknown error in the exact amount of TDI-2 defocus
4. Shot noise and Gaussian distributed noise
5. Undersampling of the image
6. Dead pixels
7. Variation in the type of scene being imaged
8. Aberrations due to nonzero mechanical tolerances

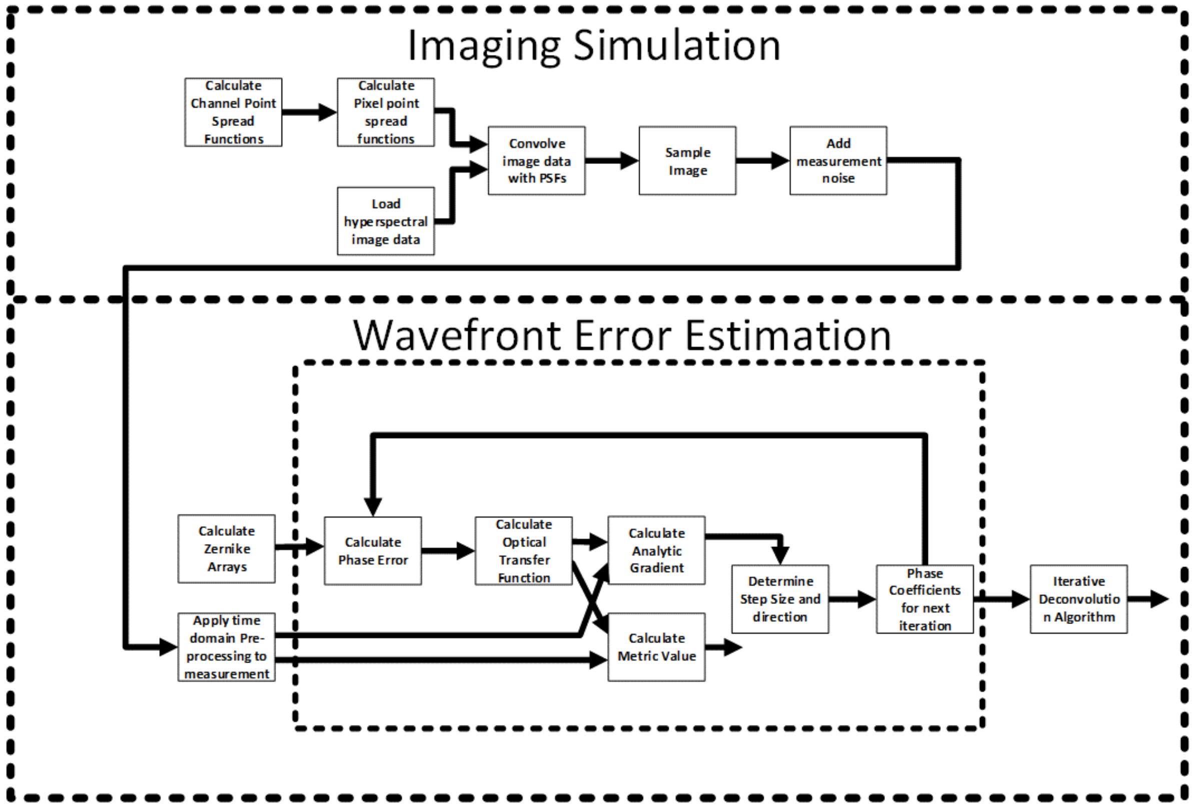

Figure 3.1: Schematic overview of the simulation tool architecture.

To realistically implement a polychromatic light source, a data set should be used that contains multispectral earth observation data, with a small spacing between the wavelength samples. It was therefore decided to use the hyperspectral AVIRIS (Airborne Visible/ Infrared Imaging Spectrometer) data set collected by NASA, which is freely available to the public [49]. The AVIRIS data samples the part of the spectrum that is received by the DST panchromatic channel, 450nm to 650nm, at 21 wavelengths. To simulate the imaging process of the scene represented by the AVIRIS hyperspectral image, two operations are performed on the data:

1. Projection of the scene on the image plane by convolving the AVIRIS data with the Pixel Point Spread Function. This takes into account:
   (a) Diffraction effects related to the aperture size and shape
   (b) Aberration effects primarily related to pointing, positioning and shape errors and instabilities in the optical components
   (c) Discrete sampling of the scene taking into account the finite, nonzero size of the pixels
2. Detector measurement simulation by addition of measurement noise and possibly dead pixels. In this particular case noise is modeled using two terms:
   (a) Poisson distributed Shot noise
   (b) A Gaussian distributed noise term to account for other noise sources

Note that there is no direct correlation between the actual resolution of the AVIRIS images and the simulated resolution of the DST. The side length of each pixel on the TDI detectors is assumed to correspond to 25cm on the ground. This will also be the case during operations at an orbital height of 550km if the pixel size remains at 5μm. Below, each individual step within the Imaging Simulation subroutine - as shown in 3.1 - is explained in greater detail.

3.1.1. Projection onto Image Plane

The first step, projecting the scene onto the image plane taking into account diffraction and aberration, is performed using the FORTA ray tracing application which contains the end-to-end model of the DST. FORTA is used to calculate the Point Spread Function of the DST panchromatic channel optics at each of the sampled wavelengths, taking into account the known defocus error for each of the detectors. The PSFs are all calculated on a common grid with spacing Δu using a constant pupil sampling distance Δx so that discrete convolution can be applied. This is achieved through zero-padding of the calculated wavefront error before applying the Discrete Fourier Transform and squaring the magnitude to obtain the PSF. Zero-padding indicates increasing the grid size of a 2D array in all four dimensions by adding an equal amount of zeros on all sides. The amount of zero padding required at each wavelength can be determined using the relation shown in (3.1) presented by Seldin et al. [50].

$$\Delta u = \frac{\lambda z_f}{N \Delta x} \tag{3.1}$$

Since the sample size N must be an integer and the distance between the image plane and exit pupil z_f is fixed, calculation of the PSFs can only be performed at wavelengths that result in an integer sample size N. As a result of this slight adjustments have to be made to the AVIRIS sample wavelengths, which slightly alters the original scene. However, for large sample size N the magnitude of these adjustments is negligible.

While the PSFs calculated using FORTA take into account diffraction and aberration effects caused by the telescope optics, they do not account for the negative effects resulting from sampling of the image by the detectors. A detector does not have an infinite resolution but instead integrates the image intensity over each of its pixels, which have a finite nonzero dimension. This can potentially lead to further deviation of the image from the ideal aberration-free image predicted by geometrical optics. This effect is accounted for in the model by calculation of a pixel PSF. This updated form of the optical PSF takes into account both diffraction and aberrations resulting from the optics, as well as effects due to the sampling by the detector. The expression for calculating this PSF is provided in equation (3.2). Proof in the form a derivation of the Pixel PSF is presented in appendix .

$$s_{pix}(\Delta u, \Delta v, u, v) = \iint_{-\infty}^{\infty} \Pi(\Delta u, \Delta v, u', v') s(u - u', v - v') \mathrm{d}u' \mathrm{d}v' \tag{3.2}$$

In this equation, Δu and Δv are the sampling distances in both directions. For this tool, square pixels are assumed which means $\Delta u = \Delta v$. A pixel PSF has to be calculated for each of the Λ wavelengths for each of the K detectors in the panchromatic channel, resulting in a set of $\Lambda \times K$ PSFs. The calculation of these PSFs is graphically summarized in figure 3.2. Once these K PSFs are calculated for each of the Λ sample wavelengths the PSFs are convolved with the scene corresponding to their respective wavelength resulting in a set of $\Lambda \times K$ images. For each detector, the aberrated images from all wavelengths are summed which eventually results in a set of K noiseless panchromatic detector images. To derive a set of noiseless detector measurements from these images, each of the K detector images is simply sampled at the locations of the pixel centers.

The tool also includes the possibility of calculating the measurements taken by the multispectral channels, so that the effect of including this data into the phase diversity algorithm can be determined. These measurements are calculated in exactly the same way as the panchromatic measurements. A pixel size four times the pixel size of the panchromatic pixels is assumed. This is in accordance with the design specification that the resolution of the multispectral channels should is four times lower than the resolution in the panchromatic channel, found in section 1.3.

3.1.2. Noise Addition

The second and last step in the DST imaging simulation is the addition of noise to the measurements. There are many imaging noise types, the most common noise types are listed below:

- **Gaussian noise:** A collection of all Gaussian distributed noise sources primarily related to the detector and amplifier circuitry, including the generally dominant Johnson-Nyquist noise [51]. Since modeling of the electronics is not a goal of this thesis project, all Gaussian noise sources are represented by a single Gaussian noise term with an arbitrary Noise Power [52]. The signal to Noise Ratio of the Gaussian noise is assumed to be 100 in accordance with values used by Dolkens and van Marrewijk [9] [19].
- **Poisson distributed Shot Noise:** Shot noise arises due to the particle nature of light [53]. The SNR for Poisson distributed Shot noise is equal to $\sqrt{N}$, where N is the number of photons per pixel. As will be

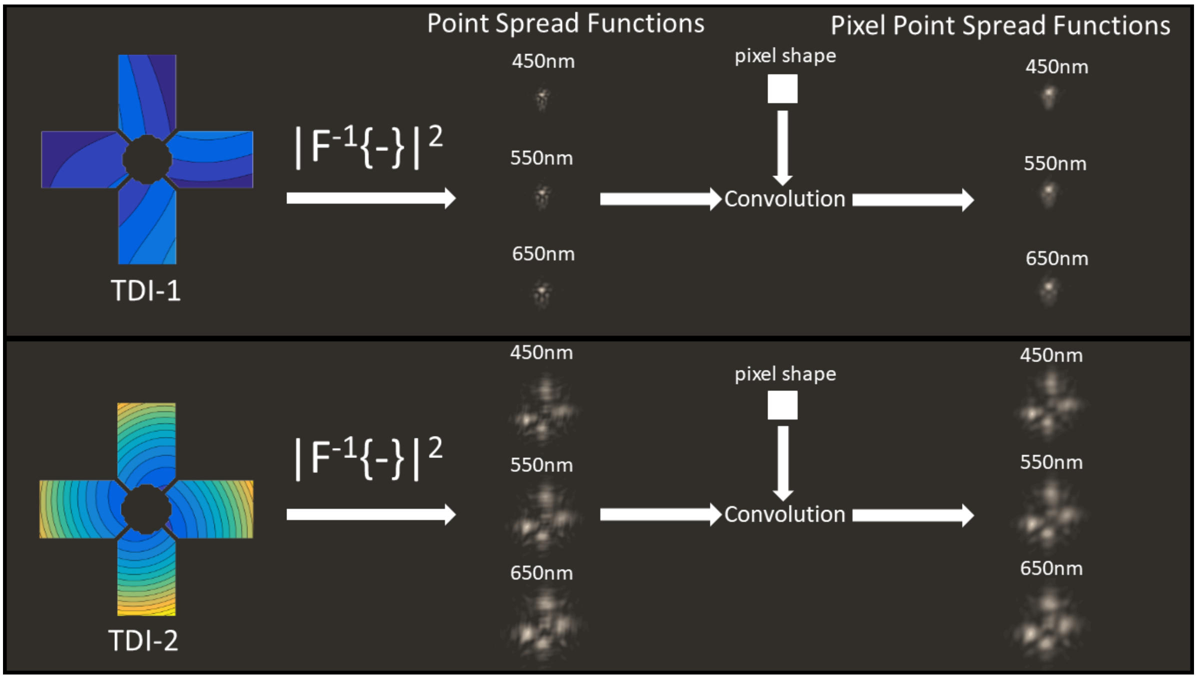

Figure 3.2: Graphical representation of the Pixel PSF calculation process. Here the colors of the PSFs correspond to the different wavelengths.

discussed in section 4.1, the average photon count per pixel is expected to be around 10^4 which would result in a SNR of about 100, the same as the SNR for the Gaussian distributed noise [46].

- **Salt-and-pepper noise:** impulsive noise that mostly arises in analog-to-digital conversion and bit errors during transmission causing random light pixels in dark areas and dark pixels in light areas [54]. Since the electronics and communication design is still at a very early stage with no details available and since it is likely that data will be processed on board, salt-and-pepper noise is not taken into account in the simulation. However, to quantify the effect of missing single pixel data, the simulation of dead pixels has been implemented so that a sensitivity analysis can be performed.

- **Quantization Noise:** Resulting from the quantization of an analog input signal. Typical TDI detectors quantize images from 8 bits to 16 bits. Since the quantization noise variance is $N_Q^2 = \frac{q^2}{12}$ where q is the quantization step, the quantization noise is expected to be negligibly low for high signal earth observation applications using a TDI detector [55].

- **Periodic Noise:** Noise that is usually generated through electromagnetic interference. The shape of periodic noise has a very high dependence on its source and therefore virtually impossible to predict without knowledge of interference sources. It is therefore assumed that the telescope, bus, and baffle designs will be such that the imaging electronics are shielded from electromagnetic interference from outside sources [54]. However, at a later stage of the project when more is known about the system and environment possible periodic noise sources should be identified and if necessary simulated.

The application of noise to the measurements is therefore performed in two steps. The first step is applying Poisson distributed, signal-dependent Shot noise to the noiseless measurement data. Because of the arbitrary scaling of the PSF, Shot noise is calculated by assuming a mean photon per pixel number for the detector measurement. The measurements are scaled such that the mean of all the photon per pixel values is equal to the desired mean. Because not much is known about the final detector choice and consequently the real photon per pixel count, a sensitivity analysis will be performed for this parameter. The second step in the noise simulation is the addition of zero mean Gaussian distributed, signal independent noise to the measurement. The signal-to-noise ratio of the Gaussian noise is set as an input parameter as it is dependent on the electronics. Making it adjustable allows simulation of different imaging electronics configurations, given that the noise statistics of the configurations are known.

The resulting set of K noisy TDI measurements plus the noisy multispectral measurements are the final output of the imaging simulation subroutine and is the input to the Phase Diversity algorithm.

3.2. Simulating the Phase Diversity Algorithm

The second subroutine consists of the phase diversity algorithm which aims to produce an accurate estimate of the wavefront error in the pupil based on the set of in-focus and phase-diverse detector measurements. The subroutine can be divided into the following steps:

1. Calculation of the basis functions for constructing the wavefront error estimate in the pupil. Since the basis functions are the same regardless of the input data, they can be stored in the satellite's on-board memory module. This means in operation, they do not have to be calculated every time the phase diversity algorithm is executed

2. In case apodization or other methods are used to mitigate the detrimental influence of edge effects on the wavefront error estimate, the image domain measurement is first pre-processed - e.g. through multiplication with an apodization window reducing the weight of pixels near the edges of the subframe in the case of apodization. This has to be done only once per optimization run.

3. Taking the (pre-processed) subframe and basis functions as inputs, a gradient-based optimization routine is executed that aims to find a set of wavefront error parameters that minimizes a broadband phase diversity metric. The set of parameters that minimizes the metric is then used to construct a final estimate of the wavefront error in the pupil.

4. The final estimate of the phase error is used to construct a broadband Point Spread Function. An iterative deconvolution algorithm is then executed to deconvolute the detector measurement and the estimated broadband Point Spread Function to obtain an estimate of the original scene that is being imaged

Again, a detailed overview of the above steps is provided in the following sections.

3.2.1. Construction of Basis Functions

As discussed in section 2.1.3, Zernike polynomials are well suited for expressing a wavefront error since Zernike polynomial shapes correspond to typical aberration shapes present in optical systems. Van Marrewijk found that to accurately fit all the minima and maxima of a typical wavefront error expected in the DST system during operation, Zernike polynomials up to and including 7 are required, which corresponds to 36 Zernike functions [19]. While using Zernike polynomials up to order 7 would thus be a logical starting point for the set of basis functions, a few adaptions are made to the standard set. A notable property of the Deployable Space Telescope is that it has a segmented primary mirror with segments of which piston, tip, and tilt can be adjusted separately. As a result, unwanted segment piston, tip, and tilt will also be introduced due to control inaccuracy, non-ideal hinges, thermal effects and compliance of support structures. In order to allow for effective wavefront error fitting, the three global piston, tip, and tilt Zernike basis functions are thus replaced by twelve basis functions accounting for the piston, tip, and tilt of each of the four primary mirror segments individually. The set of Global Zernike basis functions used is presented in figure 3.3, only polynomials up to order 4 are shown here for conciseness. The set of Segment Zernike basis functions is shown in figure 3.4. Removal of the global piston, tip and tilt basis functions is justified if it is noted that each of these modes can be easily reconstructed using the twelve segment piston, tip, and tilt modes.

3.2.2. Image Domain Pre-processing

The performance of phase diversity algorithms is generally reduced by two different types of edge effects:

1. Fourier domain artifacts due to the fact that the Discrete Fourier Transform (DFT) assumes the image is periodic and repeats itself at the frame's edges. This causes abrupt jumps at the edges in turn leading to artifacts that are detrimental to performance

2. Pixel illumination due to parts of the scene that fall outside of the subframe, but influence the measurements as a result of being smeared out by the PSF

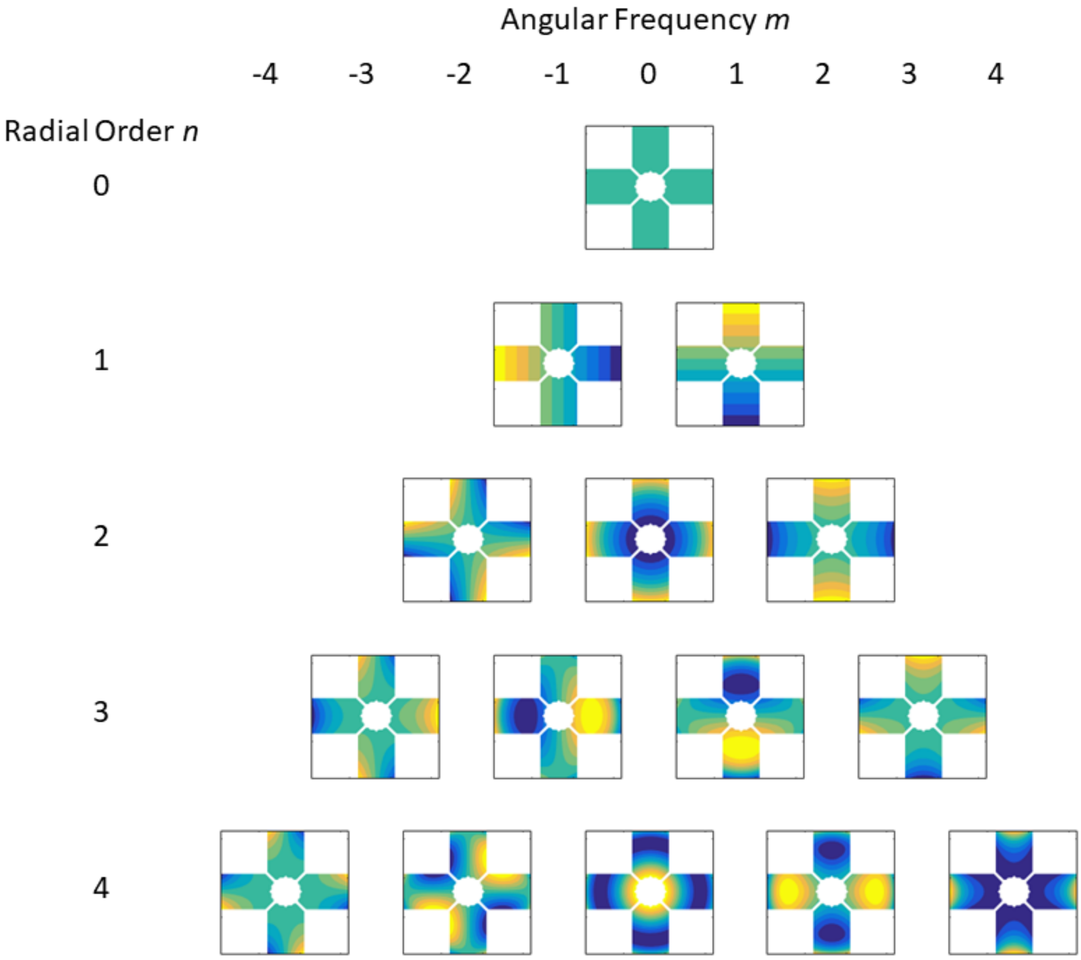

Figure 3.3: A graphical representation of the global Zernike basis functions used as a starting point for the phase diversity algorithm design.

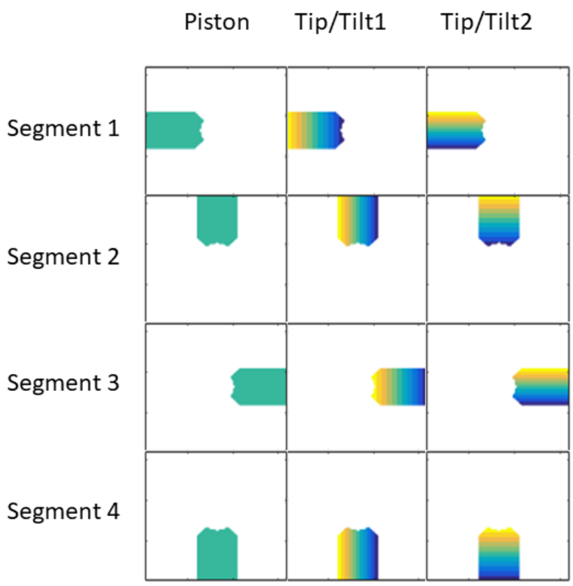

Figure 3.4: A graphical representation of the segment Zernike basis functions used as a starting point for the phase diversity algorithm design.

For the first of these two points an effective mitigation strategy, not used in the context of phase diversity algorithms before, was implemented in this tool, based on the method described by Mahmood et al. [56]. This method decomposes the Fourier transform of the image into two parts. A periodic part i_p that captures the essence of the image and a smoothly varying background i_s that captures the edge discontinuities. The periodic part, which is the part of interest, can be calculated as shown in equation (3.3)

$$I_p(p,q) = I(p,q) - I_s(p,q) \tag{3.3}$$

In this equation the indices n and m are the indices of the frequency domain arrays running from $(p,q) = (0,0)$ to $(p,q) = (N-1,N-1)$. The smooth term S can be calculated as shown in equation (3.4)

$$I_s(p,q) = \frac{B(p,q)}{2\cos\frac{2\pi p}{N} + 2\cos\frac{2\pi q}{N} - 4} \tag{3.4}$$

In this equation dependency on the indices is dropped. Term B is the Fourier transform of the edge discontinuities calculated as shown in equation (3.5)

$$b(n,m) = r(n,m) + c(n,m) \tag{3.5}$$

Here r and c are calculated as shown in equation (3.6). A visual representation of smooth decomposition is provided in figure 3.5.

$$r = \begin{cases} i(N-1-n,m) - i(n,m) & \text{, for } n = 0 \text{ and } n = N-1 \\ 0 & \text{, otherwise} \end{cases} \tag{3.6}$$

$$c = \begin{cases} i(n,N-1-m) - i(n,m) & \text{, for } m = 0 \text{ and } m = N-1 \\ 0 & \text{, otherwise} \end{cases} \tag{3.7}$$

The periodic term I_p calculated using equation (3.3), from which the edge artifacts are removed, is then used as the Fourier Transform of the image subframe during execution of the phase diversity optimization routine.

The second detrimental edge effect, the influence of parts of the scene that fall outside of the subframe on the measurement, is less straightforward to correct. One commonly used strategy is the application of image domain apodization to the subframe, which gradually reduces the pixel weight towards the frame edges with the aim of reducing the impact of 'corrupted' measurements at the boundaries. This is achieved by multiplication of the subframe with a 2D window function with values in the range $[0,1]$. The window function typically has higher values in the proximity of its center and gradually lower values towards its edges. Two examples of windows used for apodization in phase diversity algorithms are the Hamming window and the Paxman window. The Hamming window mathematically described in equation (3.8), a 1D represenation of the window is provided in figure 3.6a [57]. An adapted version window has been implemented in the context of phase diversity by Lofdahl and Scharmer [58]. The apodization window that they use consists of an unapodized square in the center of the frame with Hamming window apodization at the edges, as illustrated in figure 3.6b. This window was initially described by Luhe [59].

$$w(n) = 0.54 - 0.46\cos\left[\frac{2\pi n}{N-1}\right] \text{ for } n = 0,1,...,N-1 \tag{3.8}$$

The possibility of applying apodization to phase diversity has also been investigated by Paxman et al [60]. Instead of applying the apodization only at the edges, Paxman applies a window that apodizes the entire image. A mathematical description of the window used is provided by equation (3.9). A 1D graphic representation of the window is provided in figure 3.6c.

$$w = \begin{cases} \left[1 - \left(\frac{r}{r_c}\right)^2\right]^2, \text{for } r \le r_c \\ 0, \text{for } r > r_c \end{cases} \tag{3.9}$$

Since one of the high-level requirements for the DST is a ground resolution of below $25cm$, it is important that an apodization method preserves detail in the image. It was therefore decided to implement the

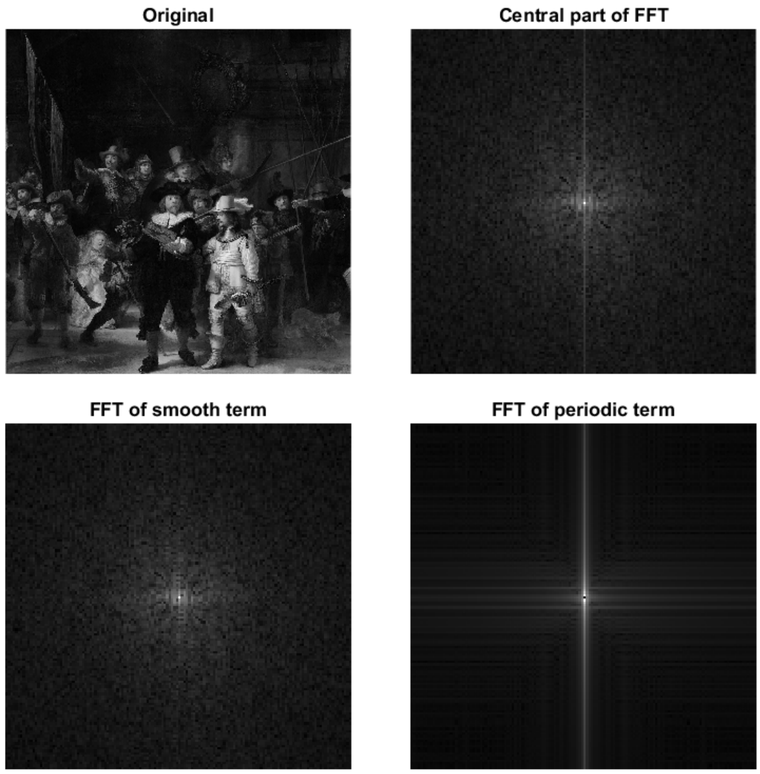

Figure 3.5: Example of smooth decomposition showing the original image in the top left corner, the central part of the Fast Fourier Transform (FFT) of the image in the top left corner, the FFT of the periodic term in the lower left corner and the FFT of the periodic term in the lower right corner. The painting shown is Rembrandt van Rijn's *Nachtwacht*, taken from the website of *Het Rijksmuseum* [8].

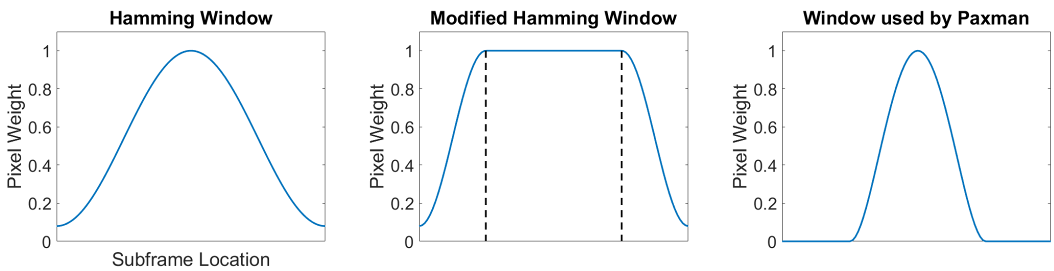

(a) The Hamming Window. (b) The modified Hamming Window [58]. (c) The window used by Paxman.

Figure 3.6: 1D representation of multiple apodization windows

approach as described by Lofdahl and Scharmer, which leaves most of the image unapodized. It was then determined through simulation if apodization increases the accuracy of the estimation.

A final method for mitigating the detrimental impact of edge effects is careful selection of the detector subframe to which the phase diversity algorithm is applied. The testing and comparison of several algorithms for selection of subframes was done. The results are further discussed in section 4.3.

3.2.3. Metric Calculation

The core of the phase diversity algorithm is the optimization routine that attempts to minimize the value of the phase diversity metric function in order to produce an accurate estimate of the wavefront error. The first step in setting up the optimization was the selection of the most suitable type of phase diversity metric. The TDI detectors in the panchromatic channel are sensitive to nearly all wavelengths in the visible spectrum. Because the performance of phase diversity algorithms that assume a monochromatic light source quickly degrade as the bandwidth of the light sources increases, it was decided to use the phase diversity optimization metric described by Seldin et al. [50], a method that was applied successfully by Bolcar as well [61]. Both have implemented the method in the context of ground-based-astronomy. This metric takes into account the broadband nature of the source. The form of the metric - shown in equation (3.10) - is the same as the 'Reduced Gaussian' metric discussed in section 2.2

$$L_M = \sum_{(f_X,f_Y)\in\chi} \sum_{k=1}^{K} |I_k|^2 - \sum_{(f_X,f_Y)\in\chi} \frac{|\sum_{l=1}^{K} I_l \hat{S}_l^{b*}|^2}{\sum_{m=1}^{K} |\hat{S}_m^b|^2} \tag{3.10}$$

The only difference between the two metrics is that for the broadband metric the set of monochromatic OTFs $\{S_k\}$ is replaced by the set of polychromatic or broadband OTFs $\{S_k^b\}$. The broadband PSFs are calculated by summing the monochromatic PSFs at each sample wavelength as shown in equation (3.11)

$$s_k^b(u) = \sum_{l=1}^{\Lambda} T_{kl} s_{kl}(u) \tag{3.11}$$

In this equation, the subscript l denotes the index of the sample wavelength. Central to the broadband phase diversity method described by Seldin is the gray world assumption. This assumption states that the spectral distribution of the light is identical for all pixels, which allows for the calculation of a single broadband PSF per detector. While this may seem like a bold assumption, it was found by Seldin that the assumption of a uniform spectrum bears a good resemblance to the real-world situation. Implementation of this assumption leads to the use of the T_{kl} terms in equation (3.11), which represent the product between the intensity and detector responsivity at a certain wavelength l, normalized so that the set $\{T_{kl}\}$ sums to 1. Two different settings for the set of scaling terms $\{T_{kl}\}$ have been implemented in the tool. The first option assumes a spectral distribution that is uniform over the part of the spectrum accepted by the panchromatic channel. The second option estimates the factor T_{kl} at each wavelength through cubic interpolation between the sums of the intensity received at each of the multispectral channel detectors. The results of a comparison between the performance achieved with each method are presented in chapter 5.

Due to the fact that the diffraction and aberration effects depend on wavelength, the $\{s_{kl}\}$ terms must be scaled by a known factor at each wavelength l. The first step is the scaling of the magnitude of the Coherent Transfer Function at each wavelength according to equation (3.12).

$$H_{kl}(f) = |H_{kl}| exp\left[i\frac{\bar{\lambda}}{\lambda}\left(\theta(f;\{\alpha\}) + \phi_k(f)\right)\right] \tag{3.12}$$

The parameter $\bar{\lambda}$, from now on called the base wavelength, is the wavelength in terms of which the wavefront error is defined. The parameter N is the one-dimensional size of the wavefront error array.

As stated before in section 3.1.1, to arrive at the wavelength dependent PSF the grid size on which the wavefront error is defined must be adapted before performing the Fourier Transform to achieve correct scaling of the PSF. The scale change resulting from the application of the Fourier transform is obtained by the relation shown in equation (3.13)

$$\Delta u = \frac{\lambda z_f}{N\Delta x} \tag{3.13}$$

The z_f is a physical design parameter of the system and is therefore fixed. The pupil sampling distance Δx is also constant because all PSFs are calculated from the same wavefront error estimate which has a fixed array size. The image plane sampling distance Δu is required to be the same at all wavelengths so that the monochromatic PSFs can be conveniently summed on the same grid. This leaves the ratio $\frac{\lambda}{N}$ as a parameter that can be used to control the scaling of the PSFs. Two factors are important in the selection of the values:

1. The set of sample wavelengths $\{\lambda\}$ should provide near uniform sampling of the panchromatic channel wavelength spectrum for accurate calculation of the broadband PSF
2. The sample size N has to be integer-valued

To find a set of wavelengths that adheres to these two requirements the following calculation steps are performed by the algorithm:

1. Generation of a preset number of wavelengths $\{\lambda\}$ uniformly sampled over the bandwidth accepted by the panchromatic channel and calculation of the corresponding set of array sizes $\{N_{kl}\}$ using equation (3.13)
2. Rounding of the array sizes N_{kl} to the nearest integer
3. Recalculation of the new corresponding set of wavelengths $\{\lambda_{kl}\}$ by inserting $\{N_{kl}\}$ into equation (3.13) again
4. Calculation of the PSFs at the adjusted wavelengths

The individual monochromatic PSFs can then be calculated by taking the Fourier transform of the Coherent Transfer function as shown in (3.14) and zero padded as shown in equation (3.15)

$$s_{kl}(u,v) = \left| h_{kl}(u,v)|^2 = | \sum_{f=0}^{N_{kl}-1} H_{kl}(f) \exp\left[i \frac{2\pi}{N_{kl}} \langle f, u \rangle \right] \right|^2 \tag{3.14}$$

$$s_{kl}(u,v) = \begin{cases} |h_{kl}(u,v)|^2 & \text{for } -\frac{N_{kl}}{2} \leq u \text{ and } v \leq \frac{N_{lk}}{2} \\ 0 & \text{for } -\frac{N}{2} \leq u \text{ or } v < -\frac{N_{kl}}{2} \text{ and } \frac{N}{2} > u \text{ or } v \geq \frac{N_{kl}}{2} \end{cases} \tag{3.15}$$

3.2.4. Gradient Based Optimization

The next step in designing the optimizer was the selection of the optimization strategy, in particular whether to use a gradient-based optimization method or a non-gradient-based method. Since the gradient provides additional information about the function it is expected that gradient-based methods generally converge faster than non-gradient based-methods, but if the computation time per iteration is higher gradient-based methods might still be slower. A few factors should be considered in the trade-off between gradient based and non-gradient-based optimization:

1. Is an analytic expression available for the gradient?
2. What is the computational cost for calculation of the gradient?
3. How smooth is the function?

The first two of these questions are related. The cost of calculating an analytic gradient is generally lower than the cost of calculating the numerical gradient since the latter requires at least one metric evaluation for each individual parameter that is optimized. However, depending on the form of the expression analytic gradients could also be costly to calculate. As with the original phase diversity algorithms developed by Gonsalves, Fienup, and Paxman, Seldin also provides an analytic expression for the analytic gradient of the broadband phase diversity algorithm. Although the expression for the gradient provided by Seldin contains some fundamental errors resulting in highly erronous values, a similar expression was derived by the author based on some of the elements and descriptions in the paper by Seldin. This expression is provided in equation (3.16)

$$\frac{\partial}{\partial \alpha_j} L_M = -4\bar{\lambda} \sum_{f'=0}^{N-1} \sum_{k=1}^{K} \sum_{l=1}^{\Lambda} \frac{1}{N^2 \lambda_l} \mathbf{Z}_{jl} \times \mathrm{Im} \left\{ \mathbf{H}_{kl}(f') \sum_{u'=-\frac{N}{2}}^{\frac{N}{2}-1} h^*_{kl}(-x') \sum_{f''=0}^{N-1} C^b_k(f'') \exp\left[i \frac{2\pi}{N} \langle f'', u' \rangle \right] \exp\left[-i \frac{2\pi}{N} \langle u', f' \rangle \right] \right\} \tag{3.16}$$

In this equation the term $\bar{\lambda}$ is the base wavelength at which the wavefront error is estimated. the boldface term $\mathbf{H}_{kl}(f)$ is the (discrete) Fourier transform of $h_{kl}(u)$ after zero padding to the size $N \times N$, mathematically expressed in equation (3.17)

$$\mathbf{H}_{kl}(f) = \sum_{u'=-\frac{N}{2}}^{\frac{N}{2}-1} \frac{1}{N_{kl}^2} \sum_{f=0}^{N_{kl}-1} H_{kl}(f) \exp\left[i\frac{2\pi}{N_{kl}}\langle f, u'\rangle\right] \exp\left[-i\frac{2\pi}{N}\langle u', f'\rangle\right] \tag{3.17}$$

Furthermore, expressions for the terms $C_k^b(f)$ and $\mathbf{Z}_{nl}$ are provided in equations (3.18) and (3.19) respectively.

$$C_k^b(f) = \frac{\sum_{j=1}^K |S_j^b(f)|^2 \left(\sum_{l=1}^K I_l(f) S_l^{b*}(f)\right) I_k^*(f) - |\sum_{j=1}^K I_j(f) S_j^{b*}(f)|^2 S_k^{b*}(f)}{\left(\sum_{j=1}^K |S_j^b(f)|^2\right)^2} \tag{3.18}$$

$$\mathbf{Z}_{jl} = \sum_{u'=-\frac{N}{2}}^{\frac{N}{2}-1} \frac{1}{N_{kl}^2} \sum_{f=0}^{N_{kl}-1} Z_j(f) \exp\left[i\frac{2\pi}{N_{kl}}\langle f, u'\rangle\right] \exp\left[-i\frac{2\pi}{N}\langle u', f'\rangle\right] \tag{3.19}$$

The full derivation of the expression for the analytic gradient is provided in Appendix B. Observing this analytic expression for the gradient, it can be observed that all the Fourier transforms and convolutions that have to be performed are independent of the wavefront error parameter for which the gradient is calculated. This means that these operations have to be performed only once per phase diversity algorithm iteration. Since the number of Zernike basis functions used for description of the wavefront estimation error will be >> 1, it is likely that calculation of this analytic gradient will be much faster than calculation of the numerical gradient, which has to perform multiple Fourier transforms for each of the Zernike basis functions.

The remaining question is then whether the function is sufficiently smooth to allow for efficient use of gradient based optimization. Several studies already proved that phase diversity algorithms using gradient based optimization can lead to good results. Some examples can be found in the references [48] [62] [61] [63]. It was therefore decided to use gradient based optimization for the tool. This decision is also retrospectively supported by results presented in chapter 5.

Concerning the choice of gradient based algorithms, an extensive comparison was performed by Ruder [64] who found that the *adam* gradient based optimization algorithm achieves the best general performance and *adam* was consequently selected as the optimization strategy for the phase diversity simulation tool. The algorithm, which originates from the scientific field of neural networks, was first presented by Kingma and Ba [11]. The acronym Adam stands for "adaptive moment estimation". The algorithm is a specific form of a Stochastic Gradient algorithm that updates its first and second moment estimates at every iteration. This results in a flexible, continuously updating learning parameter that adapts to the problem at hand. A representation of the algorithm in pseudo code, taken from [11] is provided in table 3.1. As a start the hyperparameter settings used in the original paper, i.e. $\beta_1 = 0.9$, $\beta_2 = 0.999$, $\epsilon = 10^{-8}$ and $\kappa = 0.001$ were selected. Results of a sensitivity analysis performed for the learning rate κ are presented later in chapter 5. Due to a large number of tunable parameters in this thesis project, it was decided to only change the learning rate κ and not the β_1 and β_2 hyperparameters, based on the fact that the original article also uses the learning rate as the primary means for tuning of the algorithm.

As a last step in the preliminary optimizer design, a stopping criterion for the optimizer was selected. A first attempt was made to use the step size as the stopping criterion. However, sudden jumps in the step size near the point of convergence, albeit small, resulted in unstable convergence behavior. Through trial-and-error the following stopping criterion was eventually found to be the most stable:

1. Subtract the metric value from iteration $iter - 2$ from the metric value at the current iteration $iter$
2. Normalize the result by dividing by the metric value at the start of the optimization: i.e. $iter = 0$
3. Compare the result to the (positive) stopping criterion
4. If the result is higher than the criterion, terminate the optimization

It was decided to use $iter - 2$ instead of the value at the last iteration $iter - 1$ because it was found that the metric value often oscillates slightly when near the point of convergence, and using $iter - 2$ has been found to prevent false positive convergence due to this oscillation.

Table 3.1: Pseudo Code representation of the Adam algorithm taken from [11].

Adam: An algorithm for stochastic optimization. g_t^2 indicates the element-wise square of g_t. Good default settings for the tested machine learning problems are $\kappa = 0.001$, $\beta_1 = 0.9$, $\beta_2 = 0.999$ and $\epsilon = 10^{-8}$. All operations on vectors are element-wise. With β_1^t and β_2^t, β_1 and β_2 to the power t are denoted respectively

Require: κ: stepsize
Require: $\beta_1, \beta_2 \in [0, 1)$: Stochastic objective function with parameters eta
Require: $f(\theta)$: Stochastic objective function with parameters theta
Require: θ_0: Initial parameter vector
$m_0 \leftarrow 0$ (initialize 1st moment vector)
$v_0 \leftarrow 0$ (Initialize 2nd moment vector)
$t \leftarrow 0$ (Initialize timestep)
while thetat not converged **do**
$t \leftarrow t + 1$
$g_t \leftarrow \Delta_\theta f_t(\theta_{t-1})$ (Get gradients w.r.t. stochastic objective at timestep t)
$m_t \leftarrow \beta_1 \cdot m_{t-1} + (1 - \beta_1) \cdot g_t$ (Update biased first moment estimate)
$v_t \leftarrow \beta_2 * v_{t-1} + (1 - \beta_2) \cdot g_t^2$ (Update biased second raw moment estimate)
$\hat{m}_t \leftarrow m_t / (1 - \beta_1^t)$ (Compute bias-corrected first moment estimate)
$\hat{v}_t \leftarrow v_t / (1 - \beta_2^t)$ (Compute bias-corrected second raw moment estimate)
$\theta_t \leftarrow \theta_{t-1} - \kappa \cdot \hat{m}_t / (\sqrt{\hat{v}_t} + \epsilon)$ (Update parameters)
end while
return θ_t (Resulting parameters)

3.2.5. Deconvolution

The last step in the reconstruction of the original scene is the deconvolution of the detector with the final estimate of the Point Spread Function. Deconvolution is the inverse of convolution and could be seen the "deblurring" of the image using an estimate of the PSF. A mathematical image domain expression of the deconvolution problem could be expressed as finding the object estimate $\hat{o}$ that satisfies the convolution equation shown in equation (3.20).

$$s * \hat{o} = i \tag{3.20}$$

However, as with all measurement processes the imaging process also involves the unavoidable addition of measurement noise to the measurement, which complicates the deconvolution problem. A generic measurement process such as imaging can be written as shown in equation (3.21)

$$\vec{i} = A\vec{x} + \vec{n} \tag{3.21}$$

In this equation, $\vec{i}$ is the vectorized detector measurement array, $\vec{x}$ is the vectorized object to be measured and $\vec{n}$ is the vectorized additive noise matrix. A is the measurement matrix that in the case of imaging would include the effects of diffraction, aberrations, and sampling. Since every measurement system has a finite cut-off frequency, the matrix A acts as a low pass filter filtering out the frequencies beyond the cut-off frequency of the system. If this is applied to imaging specifically: the aim of the phase diversity algorithm is to estimate the OTF of the system, which would thus approximately provide A. A logical first approach for deconvolution would then be right multiplying the measurment vector $\vec{i}$ with the matrix A^{-1}. In case the noise vector $\vec{n}$ is equal to $\vec{0}$, the original scene should indeed be retrieved. However, in practice noise is present. Since left multiplying with A acts as a low pass filter, right multiplying with A^{-1} acts as a high pass filter, amplifying exactly those frequencies at which nothing but noise can be expected. Therefore regularization methods should be applied for deconvolution to regulate noise amplification while preserving the high spatial frequencies in the signal and consequently fine details.

Two deconvolution approaches that involve regularization were studied for implementation: blind deconvolution using iterative algorithms and deconvolution using a Wiener deconvolution filter [65] [66]. A practical Wiener deconvolution filter such as the multiframe filter described by Yaroslavsky and Caulfield [67] uses an estimation of the object spectrum combined with knowledge of the noise power to apply a weight to each spatial frequency during deconvolution. The weights correlate positively with the SNR of the detector measurement at that frequency. This means that frequencies at which the SNR is low and noise is dominant, are suppressed during deconvolution. Frequencies at which the SNR is higher, which contain a lot of detail, are preserved. The mathematical formulation of the Wiener filter for a single frame as described by Wiener is provided in equation (3.22) [65], the expression for the set of multiframe Wiener filters $\{F_k\}$ - one for each channel k - as described by Yaroslavsky and Caulfield is provided in equation (3.23) [67]

$$F = \frac{1}{S}\frac{\text{SNR}}{1+\text{SNR}} \tag{3.22}$$

$$F_k = \frac{1}{S_k}\frac{\text{SNR}_k}{1+\sum_{k=1}^{K}\text{SNR}_k} \tag{3.23}$$

Two distinct advantages of this method are:

1. If the estimation of the Point Spread Function is accuracte this method can lead to an accurate reconstruction of the original object.
2. If any a priori data on the noise and object spectra is known, this information can be effectively incorporated to suppress noisy frequencies while preserving frequencies with significant signal components

After a few preliminary tests it was concluded that too little information about the object spectrum shape was available to produce an accurate object spectrum estimate, and consequently, no accurate frequency dependent SNR estimates $\{\text{SNR}_k\}$ could be found. In addition, it was found that the OTFs of the defocused detectors $\{S_{k\neq 1}\}$ degrade much faster with increasing frequency than the OTF $S_{k=1}$ due to the additional, known, aberrations. As a result, using them for calculation of the Multiframe Wiener Filter decreased the quality of the restoration rather than increasing it. It has therefore been decided to use only a single Frame Wiener filter as shown in equation (3.22) and to assume a constant SNR across all frequencies. The *deconvwnr()* algorithm from the MATLAB imaging toolbox provides this functionality and was therefore selected as one of the possible algorithms for deconvolution.

An alternative to Wiener deconvolution is blind deconvolution. Blind, iterative, deconvolution algorithms do use an initial estimate of the PSF as a starting point for deconvolution but update the PSF estimate at every iteration. A blind deconvolution method that is particularly popular is the Richardson-Lucy blind deconvolution algorithm, developed by Richardson and Lucy and presented in equation (3.24) [68] [69].

$$o_{n+1}(u) = \left[\left(\frac{i(u)}{o_n(u) * s(u)}\right) * i(-u)\right] o_n(u) \tag{3.24}$$

This method has two clear advantages and one clear disadvantage:

- **Advantages:**
  1. The smoothing properties of the algorithm are robust against incorrect lobes or spikes in the estimation of the Point Spread Function
  2. The algorithm is robust against noise if the number of iterations is restricted
- **Disdvantage:** Due to the smoothing properties described above, the algorithm is not very good at restoring fine details in case of an accurate Point Spread Function estimate

It was decided to implement the Richardson-Lucy algorithm through the use of the MATLAB algorithm *deconvblind()*. This algorithm is based upon a version of the Lucy-Richardson algorithm described by [70] which accelerates the algorithm to speed up convergence.

The difference in performance between the two algorithms was assessed during simulations in order to determine the preferred deconvolution method for the final design of the phase diversity algorithm. The results of this study are presented in chapter 5.

3.3. Chapter Summary

In this chapter, the simulation tool that was used for the end-to-end simulations of the system and phase diversity algorithms was presented. The simulation tool, of which the architecture is described in figure 3.1, consists of two distinct subroutines. The first subroutine simulates the imaging process on board the telescope and a second subroutine simulates the phase diversity algorithm that uses the simulated detector measurements to estimate the wavefront error. The first subroutine is built around the MATLAB based ray tracing tool FORTA that was developed by Dolkens specifically for simulation of the DST. FORTA simulates the optical system based on the mechanical tolerance budgets that are given as input and provides a set of Point Spread Functions, dependent on the detector, wavelength, and field angle. These PSF's are convolved with hyperspectral imaging data from NASA's AVIRIS dataset, acting as the scene, at several sample wavelengths to simulate the optical channel. Measurement noise is then added to the image to simulate the detector measurement at each detector. The added noise consists of Gaussian noise as well as Poisson distributed Shot noise. The second subroutine then applies pre-processing of these measurements in the image domain trough edge treatment and possibly apodization, after which gradient-based optimization is used to minimize a broadband phase diversity metric described by Seldin [50]. The gradient descent algorithm used for this is called *Adam* and is borrowed from the field of machine learning. As a final step, the estimated wavefront is used for deconvolution of the original measurement to produce a reconstruction of the original scene that was imaged. Most system and optimizer parameters are included as settings that can be changed so that a large number of configurations could be simulated and their performance compared.

A strategy for this comparison, so that the optimum configuration could be found and its performance analyzed, is described in the next chapter. This chapter will discuss how the software tool described was used to find answers to the research questions posed in section 1.5.

4
Simulation Strategy

The simulation tool discussed in chapter 3 provides the computational infrastructure for the comparison of different phase diversity algorithms. This chapter will describe the simulation strategy that was used for finding answers to the research questions posed in chapter 1. The strategy for obtaining relevant results that provide a definitive answer to the research questions can be divided into five steps:

1. First, a number of parametric studies were performed to determine the sensitivity of the algorithm's performance to design and environmental parameters as well as the optimum combination of optimizer settings. This was done through a set of Monte Carlo analyses. Each Monte Carlo analysis corresponded to a single parameter for which different settings were tested. The phase diversity algorithm was executed in an open-loop configuration which means that for each simulation the optimization was only executed once to produce a wavefront error estimate, no iterative approach based on a deformable mirror was used. At this stage, the performance of each of the simulations was expressed using the original and residual Strehl ratios as well as the iteration count and run times of the optimizations.

2. After the optimum settings were determined, these settings were applied to the algorithm and another Monte Carlo analysis was performed. The aim of this analysis was to compare two configurations for the optimizer, one configuration that assumed a uniform grey world spectrum and a second configuration that assumed a spectrum calculated based on the averaging of the multispectral channel measurements. This was done to test the hypothesis that the algorithm performance can be increased by including the multispectral channel data in the optimization. The residual Strehl ratio was used as the figure of merit for determining performance.

3. In the third step, the subframe selection algorithm that was developed was implemented to test whether performance can be increased by careful selection of the subframe to which the phase diversity algorithm is applied. This was tested by performing a Monte Carlo analysis comparing the performance of the optimum algorithm configuration without the subframe selection algorithms to the performance of the algorithms that used subframe selection. Again the Strehl ratio was used as the figure of merit

4. After the final configuration of the algorithm was selected, including decisions on using multispectral data and/or subframe selection, a more thorough analysis of the algorithm was performed by assessing not just the residual Strehl ratio, but also the RMS of the wavefront error as well as the quality of the image reconstruction obtained through deconvolution

5. Finally, the phase diversity algorithm was tested with a deformable mirror in the loop to see if the algorithm can be used for active control of the wavefront aberrations in the Deployable Space Telescope. Performance was measured using the residual Strehl ratio and the RMS value of the wavefront error

The next sections will elaborate on the steps presented above, with section 4.1 explaining the strategy for the parameter studies, 4.2 explaining the strategy for the multispectral data inclusion analysis, 4.3 elaborating on the strategy for the subframe selection algorithm analysis, section 4.4 setting out the strategy for the final Open-Loop performance analysis and section 4.5 dictating the strategy for the final Closed-Loop performance analysis. An overview of the MATLAB files that the toolbox consists of can be found in appendix D

4.1. Parametric Studies

To be able to draw conclusions that can aid in determining the optimum design of the system, the impact of critical system design parameters, as well as optimization settings on the performance of the phase diversity algorithm, have to be determined. To achieve this, a sequence of parametric studies was performed for the following system design parameters;

1. Number of Detectors
2. Pixel pitch
3. TDI-2 defocus
4. Along track field separation between TDI-1 and TDI-2
5. Mechanical tolerances
6. Unknown TDI-2 defocus error
7. Gaussian Signal to Noise ratio
8. Contrast in terms of mean photons per pixel
9. Chance of a dead pixel
10. Type of scene being imaged

In addition to the system design parameters, several setting parameters were tested for the phase diversity algorithm with the aim of finding the optimum configuration. These are:

1. Number of Zernike orders used
2. Optimizer learning rate η
3. Number of wavelength samples
4. Size of the subframe
5. Apodization ratio

To ensure the results could be effectively compared, a set of baseline settings was determined as a starting point for the parametric studies. These standard setting values are presented in table 4.1.

For each parametric study, a single parameter was changed while all the other settings remained constant. Based on the results the relation between the parameter values and the algorithm performance could then be established. An overview of the parameters that were studied including the parameter values for which simulations were run is provided in table 4.2. For each step of the Monte Carlo analysis, the wavefront error was calculated based on the mechanical tolerance settings. A wavefront estimation was then produced for each of the parameter values through optimization with the phase diversity tool. This was repeated many times for each of the parameter studies. Performing a large number of runs with varying wavefront errors mitigates the effects of accidental peaks or troughs in performance for configurations that generally perform poorly or very good, respectively. In a trade-off between statistical power and computational efficiency, it was decided to run 50 simulations for every parameter.

During earth observation, several types of scenes with significantly different landscapes could be encountered. In order to simultaneously study the performance of the algorithm for different types of scenes, five scenes were selected for imaging simulation from the AVIRIS dataset. The 50 runs that were performed for each Monte Carlo analysis were evenly distributed over the five scenes, resulting in 10 runs per scene. The scenes and their names are presented in figure 4.1

As stated earlier the performance of the method was measured by recording the original and residual Strehl ratios of each of the simulations. The original Strehl ratio was simply be calculated as explained in section 2.1. For calculation of the residual Strehl ratio, the estimated wavefront error was subtracted from the actual wavefront error as shown in equation (4.1).

$$\theta_{res}(x,y) = \theta_{act}(x,y) - \theta_{est}(x,y) \tag{4.1}$$

Table 4.1: Table of standard settings for the parametric studies.

Parameter	Value	Unit
Number of detectors	2	-
Pupil Sampling Distance FORTA	1.02	mm
Tolerance Type	Drift (see table 1.3)	-
Number of Discrete Field Angles for PSF calculation	3	-
TDI 2 defocus	0.5	wavelengths
Phase Diversity Subframe Size	128	pixels
Detector Pixel Pitch	5	μm
Average photon count per pixel	10^4	-
Gaussian Noise SNR	100	-
Zernike Polynomials	36 (= 45 basis functions)	-
Apodization ratio	0	$\frac{pixels_{apodized}}{pixels_{unapodized}}$
Learning Rate κ	0.001	-
Max Number of Iterations	1000	-
Defocus Error	0	μm
Step Tolerance (Fraction of initial Metric Value)	$1 \cdot 10^{-7}$	-

Table 4.2: Parameters for which a parameter study has been performed and the corresponding values for these parameters.

Parameter	Values	Unit
Number of Detectors	$[2,3]$	-
Pixel pitch	$[5,8,11]$	μm
TDI-2 defocus	$[0.01,0.25,0.5,0.75,1]$	mm
Field separation between TDI-1 and TDI-2	$[1,1.5,2,2.5]$	x normal separation
Mechanical tolerances	$[1,1.5,2,2.5]$	x nominal
Unknown TDI-2 defocus error	$[0,1,2,3,5]$	μm
Gaussian Signal to Noise ratio	$[100,75,50,10]$	-
Contrast in terms of mean photons per pixel	$[1e2, 5 \cdot 10^2, 1 \cdot 10^3, 5 \cdot 10^4, 1 \cdot 10^4]$	photons/pixel
Chance of a dead pixel without correction	$[0\%, 0.1\%, 1\%, 10\%]$	%
Chance of a dead pixel with correction	$[0.1\%, 1\%, 10\%]$	%
Type of scene being imaged	[Farm, Sea, Storm, Mountains, City]	Type
Number of Zernike orders used	$[1,2,3,4,5,6,7,8]$	-
Optimizer learning rate	$[1 \cdot 10^{-4}, 5 \cdot 10^{-4}, 1 \cdot 10^{-3}, 5 \cdot 10^{-3}, 1 \cdot 10^{-2}]$	-
Number of wavelength samples	$[1,3,7,11,15]$	-
Size of subframe	$[64,128,256]$	pixels
Apodization ratio	$[0.0,0.25,0.5,0.75,1.0]$	$\frac{pixels_{apodized}}{pixels_{unapodized}}$

(a) Farm (image taken above Michigan).

(b) Storm (image taken above Arizona).

(c) Sea (image taken above Gulf of Mexico).

(d) Mountains (image taken above New Mexico).

(e) City (image taken above San Diego).

Figure 4.1: Scenes used for the imaging simulation.

The residual wavefront error was then used to calculate the residual PSF, of which the peak value was then divided by the peak value of the aberration-free PSF to arrive at the residual Strehl ratio as shown in equation (4.2)

$$\mathrm{SR}_{res} = \frac{max[s_{res}(x,y)]}{max[s_{aberration-free}(u,v)]} \tag{4.2}$$

The results of the parametric studies are presented in section 5.1.

4.2. Multispectral Data

To test whether the inclusion of the multispectral channel measurement data can increase the performance of the phase diversity algorithm, another Monte Carlo analysis was performed. Again 50 runs were executed, divided equally over the five scene types. For each of the 50 wavefront errors that were generated using FORTA, the phase diversity algorithm was run twice. Once with the assumption that the grey world spectrum of the scene was uniform, i.e. all T_{kl} coefficients are equal. This was already implicitly assumed in all the previous simulation runs executed in the parametric studies done up until this point. The second time the algorithm was run values for the coefficients T_{kl} were calculated by simulating the multispectral channel measurements of the multispectral channels defined in table 1.2. Simulation of the measurements was performed using the following steps:

1. First the Multispectral channel PSFs were simulated by convolving the TDI-1 PSFs at each wavelength with a pixel with dimensions that are four times the dimensions of the TDI-1 pixel dimensions. The assumption of a multispectral channel pixel with four times the size of a panchromatic channel pixel was made based on the fact the resolution of the multispectral channels will also be four times lower than the resolution of the panchromatic channel

2. After that, the multispectral pixel PSF at each sample wavelength was convolved with the image at the same wavelength and then added to the measurement corresponding to that sample wavelength as indicated by table 1.2

3. As the last step in simulating the measurements the intensity measurement array in each of the channels was divided by the number of sample wavelengths in that band to compensate for the fact that some of the multispectral channels contain more sample wavelengths than others

4. To arrive at the set of T_{kl} values, each of the intensity measurement arrays was summed to arrive at a non-normalized value for T_{kl} and subsequently divided by the sum of these non-normalized T_{kl} values to enforce the requirement that $\sum_{l=1}^{\Lambda} T_{kl} = 1$

This calculation implicitly assumes that the wavefront errors in the multispectral channel and panchromatic channel are identical. This will not be the case during operation. However, since the point spread function influences only the spatial distribution of the intensity in the image plane and not the spectral content, the effect of this assumption on the result was expected to be negligible.

Comparison of the two configurations was again done using the residual Strehl ratio as the figure of merit. The results of the study are presented in section 5.2.

4.3. Subframe Selection

Preliminary runs of the phase diversity tool showed that edge effects are prime contributor to estimation errors. While image domain pre-processing was already implemented to mitigate edge artifacts resulting from the application of the FFT algorithm, it was expected that the influence of edge effects on the estimation could also be decreased by careful selection of the subframe to which the phase diversity algorithm is applied. It was expected that better performance would be achieved if the ratio of intensity in the middle of the subframe over intensity around the boundaries of the subframe was maximum. To find a subframe with a high center intensity over boundary intensity, two different selection algorithms were proposed:

1. The *Bright Peak* algorithm. This algorithm simply searches for the point in the image with the highest intensity and selects this point as the center of the subframe.

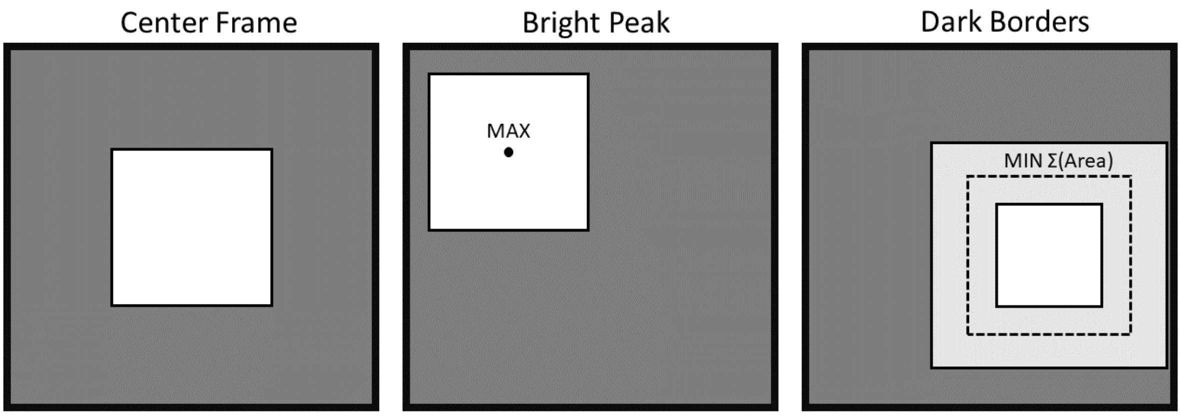

Figure 4.2: Schematic representation of the three subframe selection methods.

2. The *Dark Borders* algorithm. This algorithm convolves the image with a square array of a slightly larger size than the subframe. The has value 1 around the edges of the subframe and value 0 in the center. The result is then cropped to remove the convolution results at the boundaries. The last step is the selection of the point of minimum intensity in the convoluted array, which corresponds to the point where the sum of the intensity in the region around the boundaries of the subframe is minimum. This point is then selected as the center point for the subframe.

Through simulation, these two algorithms were tested against each other and against the standard center frame selection approach, i.e. selecting the central frame of the image as the frame to which phase diversity is applied without taking into account the intensity distribution over the image. A schematic representation of these three selection methods is presented in figure 4.2. A comparison was done through a Monte Carlo analysis. The figure of merit was once again the residual Strehl ratio.

4.4. Open-Loop Performance

After the final configuration of the algorithm was determined based on the parametric studies, the multispectral measurement inclusion studies and the subframe selection studies, a final set of open loop tests was executed to assess the performance of the algorithm. The performance was more extensively analyzed than in the previous studies so that a more complete overview of the strong points and flaws of the algorithm was obtained. The figures of merit that were used are:

1. The residual Strehl ratio
2. The RMS OPD in terms of wavelengths of $450nm$
3. A qualitative comparison of the original scene, the TDI-1 measurements and the deconvolution results

The reason for the selection of these figures of merit was that they allow for convenient verification with respect to the functional system requirements presented at the beginning of this report. In addition, assessing a wavefront error in terms of both RMS as well as Strehl ratio is robust since Strehl ratio focuses more on the image quality, and RMS focuses more on the wavefront shape estimation accuracy.

While sufficient discussion on the topic of the residual Strehl ratio has already been provided earlier in this report, it is necessary to elaborate a bit further on the topic of the Root Mean Square calculation. While the basic concept was already discussed in section 2.1, an additional pre-processing step was included in the calculation of the RMS value after the residual wavefront error was calculated by subtraction of the wavefront error estimate from the actual wavefront error. The residual wavefront error still contains global tip/tilt and piston terms that will add to the RMS value. However, a global piston error in the wavefront error is inconsequential in the calculation of the resulting image since it will not cause any blur or shift. While global tip/tilt does cause distortion of the image, it does not cause a blur and the resulting loss of information. To ensure that the RMS value is an actual measure of the optical performance of the system, it is therefore important to remove the global tip/tilt and piston terms from the residual wavefront error before calculating the RMS, this was done during the algorithm' open-loop performance assessment.

After the open-loop algorithm results were assessed in terms of the residual Strehl ratio and RMS error, a qualitative analysis of the simulations that resulted in a poor wavefront error estimate was performed. Based on this analysis the algorithm was updated and a second assessment of the results was performed.

Finally, the qualitative comparison of the deconvolution results was performed by comparing the original scene, the TDI-1 measurements, the Richardson-Lucy reconstructions and the Wiener Filter reconstructions for four representative cases.

4.5. Closed-Loop Performance

Finally, after the optimum design parameters and optimizer parameters were established, a closed-loop phase diversity algorithm was simulated that includes a deformable mirror in the loop for active correction of the wavefront error. The active optics elements that were used for control of the wavefront error in the simulations are:

1. The M1 segment control system which controls the tip, tilt, and piston of each of the four primary mirror segments. The control position for these four controllers is derived from the estimated segment tip, tilt and piston terms.
2. An ideal deformable mirror located at the position indicated in figure 1.9 that is controlled using a modal control scheme. A set of global Zernike coefficients is provided as input, resulting in a mirror shape that is a weighted linear combination of Zernike polynomials. The input coefficients are determined from the global shape parameters estimated by the phase diversity algorithm.

The simulations were executed by Dolkens using FORTA in combination with the PD toolbox developed in this project. Three distinct configurations were modeled:

Configuration 1: A configuration in which the mechanical tolerance budgets presented in table 1.3 were assumed as a starting point. This means that the performance of the first iteration was expected to be similar to the performance predicted by the open-loop performance analysis results in section 5.4.

Configuration 2: A configuration similar to configuration 1. in all aspects, except that a different, updated set of mechanical tolerance budgets was assumed. This set of tolerance budgets is presented in table 4.3. The value that has been changed with respect to the old *Drift* tolerance budgets is the tilt around Z for the M1 mirror.

Configuration 3: A configuration in which a calibrated system is assumed. Such a system is generated in two steps. First the *Deployment and Coarse Alignment* budgets from table 1.3 are assumed for generation of the wavefront error. After that calibration using a quick phasing algorithm based on the use of the piston camera measurements is executed. This phasing method is described by Dolkens [71]. Finally, the *Drift* tolerances as presented in table 4.3 are added. The resulting system will then form the starting point for the closed-loop performance simulations. This configuration is fundamentally different from the other configurations since simulation starts from a situation in which the deformable mirror and primary mirror segments are already set at a nonzero position.

For each of these configurations, 100 simulations will be run, and each simulation will count seven iterations, i.e. seven PD algorithm executions and subsequent active optics reconfiguration steps. Performance of the closed-loop simulations was measured in terms of the RMS error and the residual Strehl ratio. A comparison will be made between:

1. The initial performance of the optical system

Table 4.3: Overview of the updated mechanical tolerance budgets used for configuration 2 in the closed-loop performance simulations.

Element	**Position [µm]**			**Tilt [µrad]**			**Radius [%]**	**Shape Error [nm]**
	X	**Y**	**Z**	**X**	**Y**	**Z**		
Deployment and Coarse Alignment Tolerances								
M1	2	2	2	2	4	50	$1\cdot10^{-3}$	50
M2	15	15	10	100	100	100	$1\cdot10^{-2}$	25
M3	4	4	4	10	10	50	$1\cdot10^{-3}$	10
In-Orbit Drifts								
M1	$2\cdot10^{-2}$	$2\cdot10^{-2}$	$2\cdot10^{-2}$	$1\cdot10^{-2}$	$2\cdot10^{-2}$	$5\dot{1}0^{-2}$	$1\cdot10^{-4}$	5
M2	4	4	2	6	6	12	$1\cdot10^{-4}$	5
M3	$1\cdot10^{-1}$	$1\cdot10^{-1}$	$1\cdot10^{-1}$	1	1	5	$1\cdot10^{-4}$	5
Stability Budget								
M1	$5\cdot10^{-3}$	$5\cdot10^{-3}$	$5\cdot10^{-3}$	$2.5\cdot10^{-3}$	$1\cdot10^{-2}$	$5*10^{-1}$	n/a	n/a
M2	1	1	$5\cdot1^{-1}$	1.5	1.5	3	n/a	n/a
M3	$2.5\cdot10^{-2}$	$2.5\cdot10^{-2}$	$2.5\cdot10^{-2}$	$2.5\cdot10^{-1}$	$2.5\cdot10^{-1}$	1.25	n/a	n/a

2. The performance of the optical system after the seven iterations have been completed

3. The performance at the iteration where performance was optimum

4.6. Chapter Summary

This chapter established the strategy that was used for answering the research questions using the simulation tool described in chapter 3. This strategy can be separated into five distinct steps. The first step was determining the sensitivity of the algorithm performance to environmental parameters such as noise and contrast as well as design parameters such as the pixel size. In addition, a broad range of settings parameters for the algorithm was tested so that the optimum configuration for the algorithm could be determined. These first studies are called parametric studies.

The second step and third step were aimed towards answering the secondary research questions. Step two compared the performance between a configuration in which the grey world spectrum of the image was assumed to be uniform to a configuration which calculated a grey world spectrum based on the measurement data from the multispectral channels. Step three compared several methods for selection of the subframe to which the phase diversity algorithm is applied.

Based on the results from the first three steps a final open-loop PD algorithm configuration was determined of which a more in-depth performance analysis was performed in step four, including assessment of the quality of deconvolution results. This performance analysis involved a second iteration in which the performance was reassessed after the application of a post-processing algorithm.

Finally, a closed-loop configuration was simulated in which the wavefront error estimate was used as input for the deformable mirror after which the algorithm was executed again. This was done for five iterations after which the final system performance was assessed.

The next chapter will present the results of the simulation steps described in this chapter.

5

Results and Discussion

In the last chapter, a simulation strategy for answering the research questions was outlined. In this chapter, the results of these simulations are presented. The results are presented and discussed in five parts. Section 5.1 treats the results of the parametric studies, section 5.2 discusses the results of the multispectral data inclusion study, section 5.3 presents the results of the subframe selection study, section 5.4 will deal with the results of the open-loop performance analysis and section 5.5 deals with the results of the closed-loop performance analysis. The results are all presented graphically in this chapter, but the reader is referred to Appendix C for tabulated results including information about the run times and iteration counts, the latter indicates the number of iterations it took the algorithm to converge.

5.1. Parametric Studies

In the following sections, the results of the parametric studies are presented, accompanied by a discussion on the implications the results have for the system design and optimizer settings. The results are tabulated in appendix section C.1.

5.1.1. Number of Detectors

Two different configurations were compared. A three detector configuration and a three detector configuration. The defocus errors used in these configurations are presented in table 5.1. Details on the performance of the simulations are graphically represented in figure 5.1, which show a histogram plot of the Strehl ratio and the Strehl ratio increase for each of the configurations.

From the results, it is apparent that the addition of a third detector does slightly increase the overall performance of the algorithm, albeit at the cost of additional computation time. A closer look at table C.1 shows that the larger run time for the 3 detector configuration is the result of the additional time it takes for calculation of the metric and gradient.

It can be observed that both the absolute performance of both configurations as well as the performance relative to the other configuration also changed depending on the type of scene. For the *Farm* and *Mountains* scenes, scenes that could be classified as colorful and smooth natural landscapes, the performance for both configurations was around 0.8 on average. This indicates diffraction-limited imaging, and the difference between their performance seems to be negligible. For the *Storm* scene the overall performance of the algorithm was less, resulting in a significantly lower residual Strehl ratio, only marginally better than the original Strehl ratio. Two possible causes of this are:

1. Due to the uniform nature of the scenes differences in measured values between adjacent pixels is

Table 5.1: Known detector defocus errors.

Configuration	**Known Defocus Errors** $[mm]$			**Relative Field Angle** $[mrad]$		
	Detector 1	**Detector 2**	**Detector 3**	**Detector 1**	**Detector 2**	**Detector 3**
2 Detectors	0	0.5	-	0.3479	0.3778	-
3 Detectors	0	0.5	0.25	0.3479	0.3778	0.3178

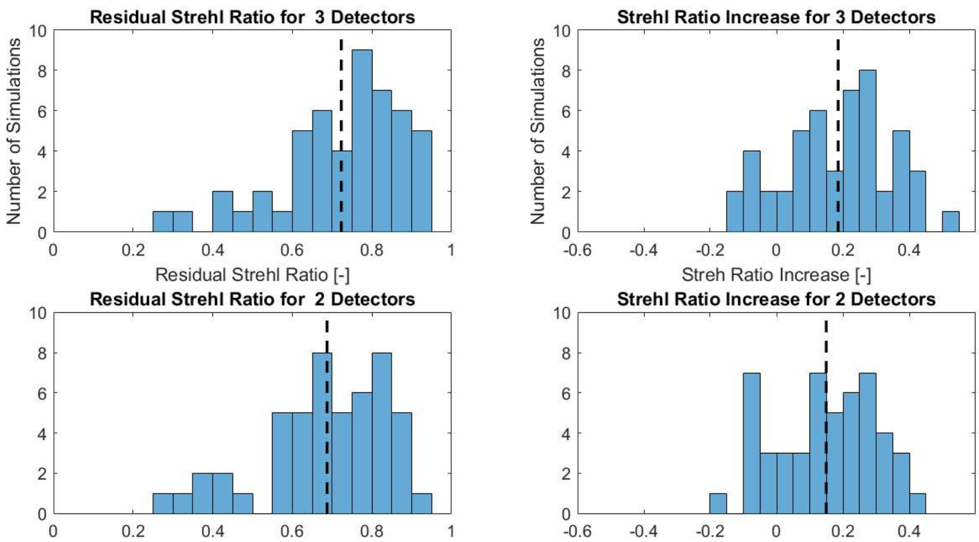

Figure 5.1: Residual strehl ratio and strehl ratio increase distribution resulting from the simulations.

smaller than in other scene types. The ratio between the average difference between two pixels over the image noise is thus effectively smaller. This increases the impact of noise

2. Distinct features in a scene make it easier to identify the Point Spread Function footprint. As an example, the limit case of individual bright starts against a dark background is taken. In these images, the shape of the Point Spread Function is very recognizable.

In general, it can be observed that the better overall performance of the 3 detector configuration was mostly the result of the superior performance for the urban area and ocean type scenes. The performance increase comes at the cost of a higher computational load, weight, volume, and complexity of the design, in discussions with Dolkens it was decided that the addition of the third detector is therefore not feasible.

5.1.2. Pixel Pitch

The three different pixel pitches that were simulated are $5\mu m$, $8\mu m$ and $11\mu m$. Figure 5.2 presents a histogram representation of the residual Strehl ratio and Strehl ratio increase distributions per configurations.

It can be observed that the time per iteration was approximately the same for each of the simulated pixel pitches, which was expected since the size of the subframe to which the phase diversity algorithm is applied remains the same in terms of pixel number. It can be observed that on average the $8\mu m$ pitch configuration took fewer iterations to converge, but the run time of the other two configurations was only about $6s$ or 6.7% higher.

In line with expectations, the smaller pixel pitch performed better than the larger pixel pitches, because the extent to which the image was undersampled is less. The decrease in Strehl ratio was very steep with a decrease in the average residual Strehl ratio of 0.15 when the pitch was increased from $5\mu m$ to $8\mu m$. It should be noted that the *Sea* scene presents an interesting anomaly, for this scene the largest pixel pitch, $11\mu m$, outperformed the $5\mu m$ configuration. It is expected that this is coincidental and caused by a different noise distribution. Due to the limited time available and the low urgency of this particular question, no further studies will be performed to investigate this phenomenon.

5.1.3. TDI-2 Defocus

The performance of the configuration, with TDI-2 defocus varying from $0.01mm$ to $1mm$ is presented graphically in figure 5.3.

It can be observed that the performance was highest for the $0.25mm$ and $0.5mm$ configurations, which both showed an average residual Strehl ratio of 0.69. The $0.25mm$ showed better performance for the *Sea* scene type, but the $0.5mm$ showed superior performance on the *storm* scene type. While performance in

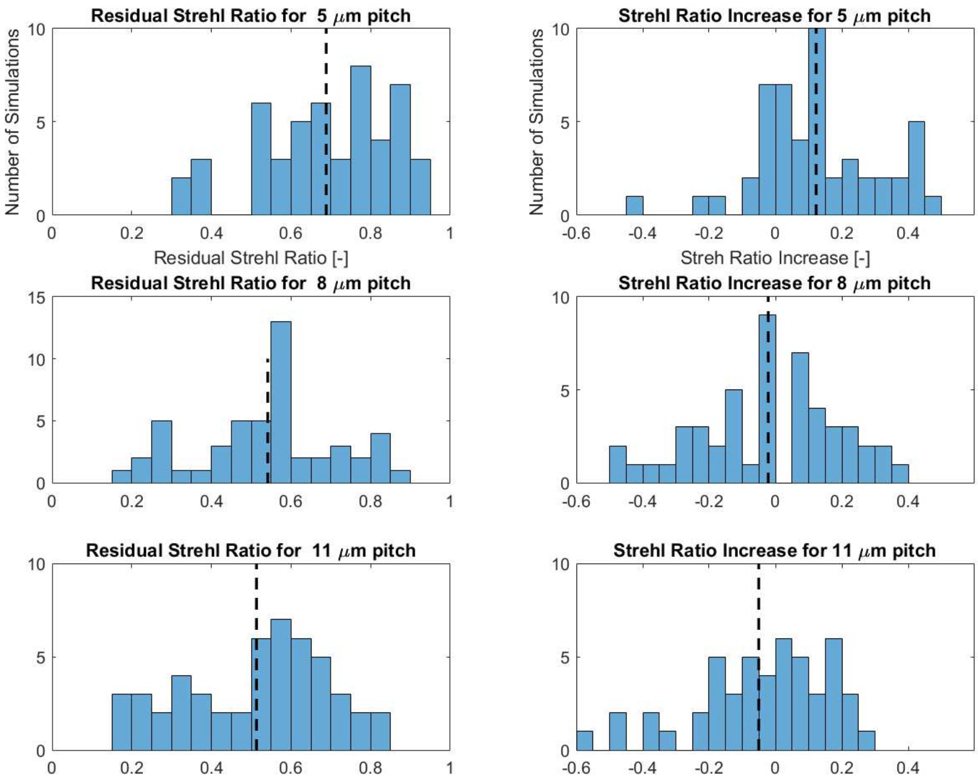

Figure 5.2: Residual strehl ratio and strehl ratio increase distribution resulting from the simulations.

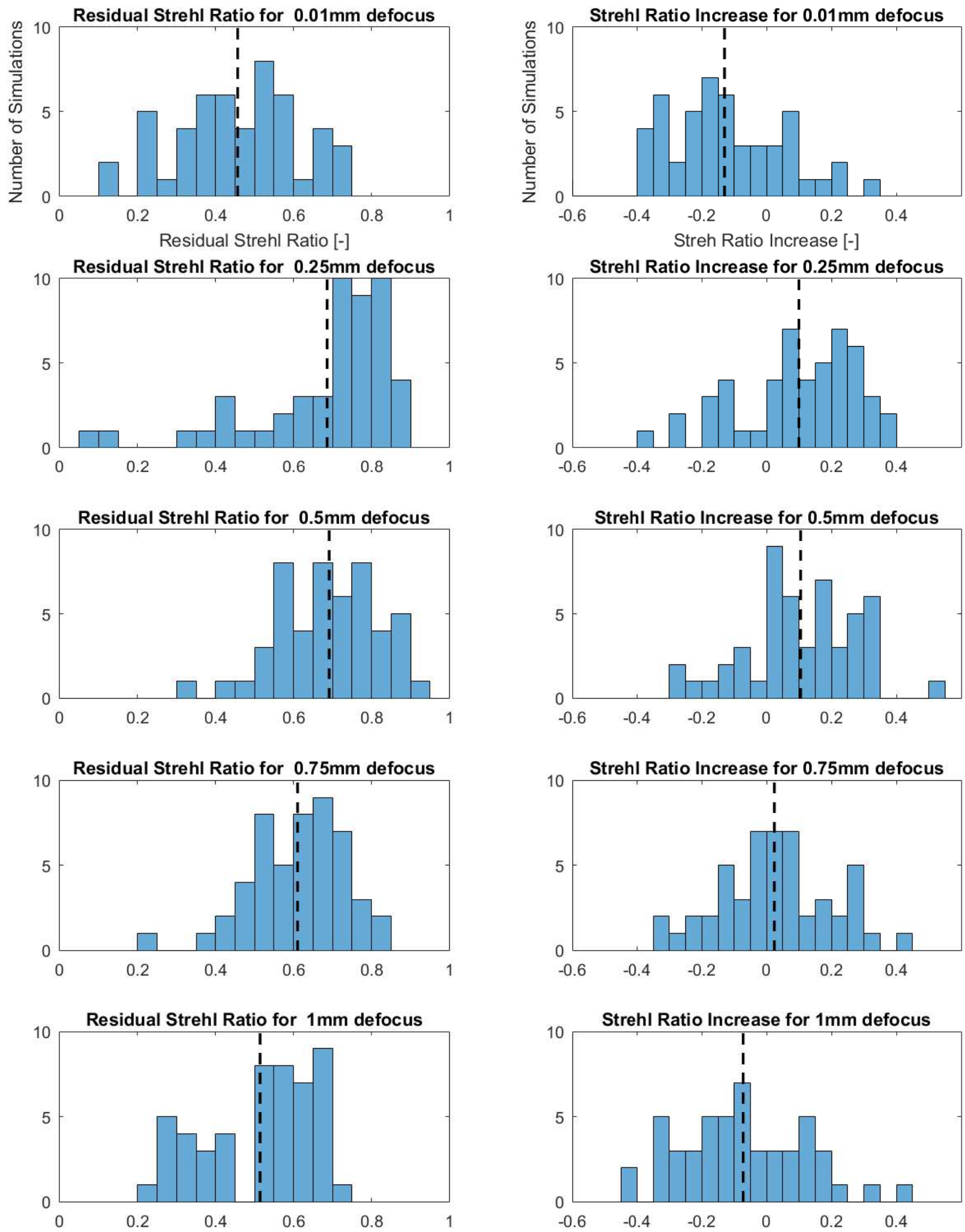

Figure 5.3: Residual strehl ratio and strehl ratio increase distribution resulting from the simulations.

terms of average residual Strehl ratio was similar for both configuration the $0.25mm$ showed better performance when the run time is also taken into accounts. Convergence for the $0.25mm$ configuration was about $102s$ on average which is $10s$ faster than the $0.5mm$ configuration. This is due to the fact that the $0.25mm$ defocus configuration takes fewer iterations to converge. The difference is small and the exact reason for this is difficult to determine due to the complexity of the algorithm.

5.1.4. Field Separation

Simulations were performed for the nominal field separation between the detectors in the along-track direction, 1.5 times the nominal separation, 2 times the nominal separation and 2.5 times the nominal separation between detectors. The results are presented in figure 5.4.

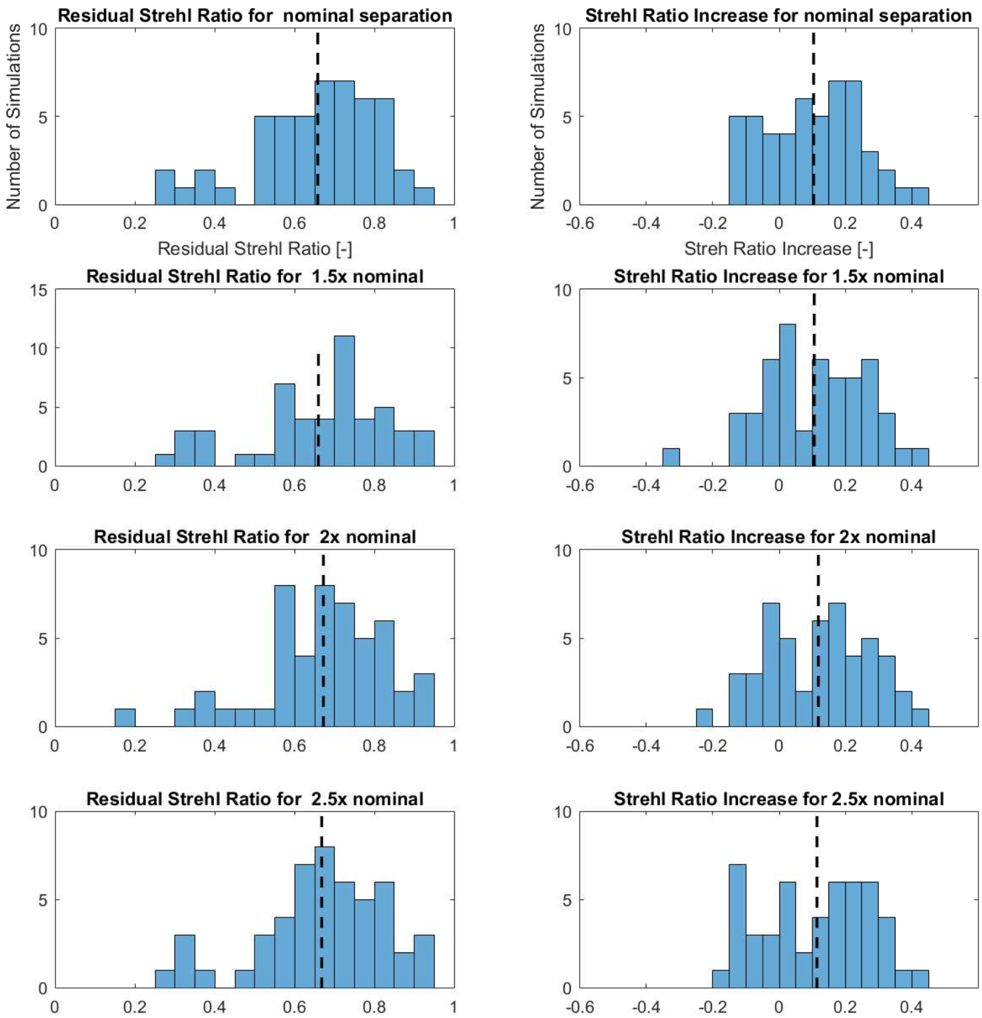

Figure 5.4: Residual strehl ratio and strehl ratio increase distribution resulting from the simulations.

From these results, it can be observed that increasing the field separation between the detectors in the along track direction up to a factor of 2.5 did not noticeably affect the performance in terms of residual Strehl ratio or run time. This indicates that the wavefront error could be considered field independent within the interval tested. Therefore the field separation can be changed if desired for decreasing weight, volume, complexity or manufacturability of the system.

5.1.5. Mechanical Tolerances

For this analysis, the Mechanical *Drift* tolerance budgets were multiplied by a factor 1, 1.5, 2 and 2.5 respectively. The results of this analysis are presented in figure 5.5.

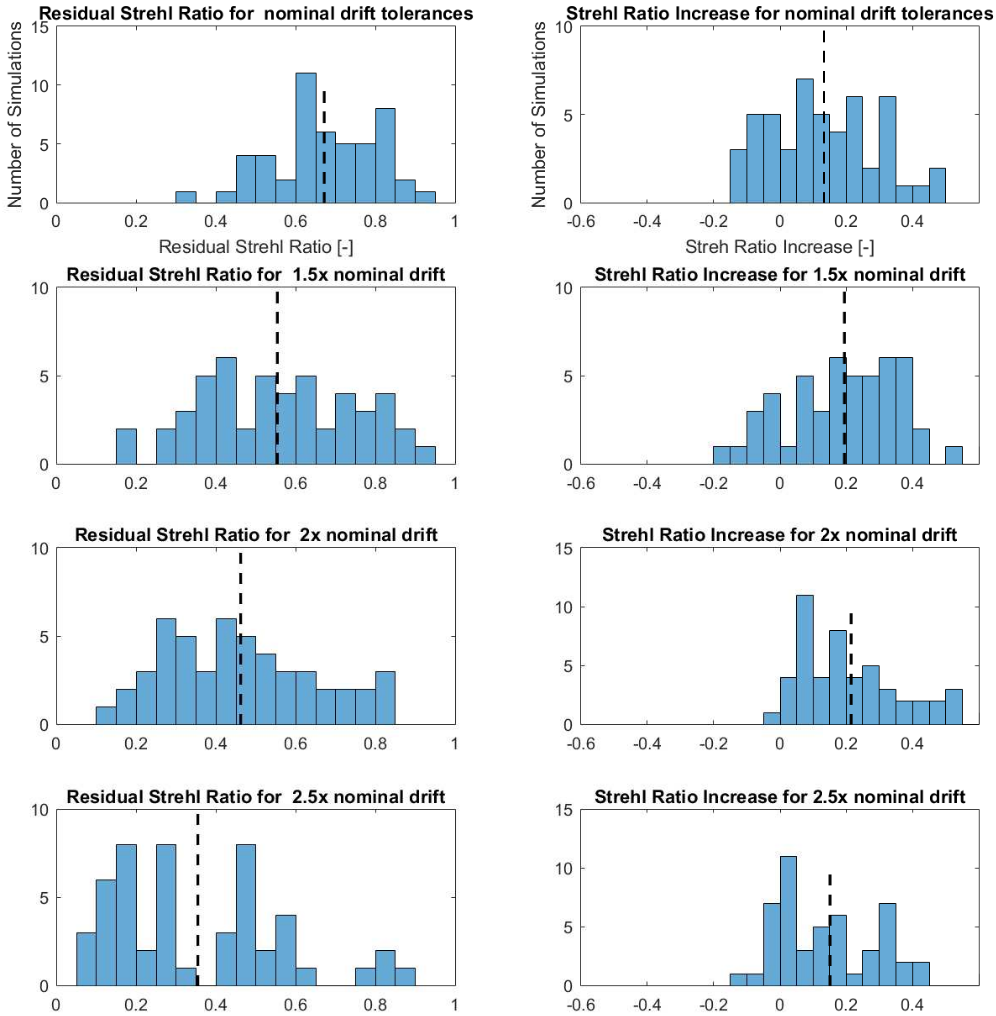

Figure 5.5: Residual strehl ratio and strehl ratio increase distribution resulting from the simulations.

While, as expected, the average residual Strehl ratio decreased steeply with the relaxation of the mechanical tolerance budgets for all scene types, it is interesting to note that the average increase in Strehl ratio achieved through the application of phase diversity did not noticeably decrease. The average Strehl ratio increase is actually higher for the cases of 1.5 and 2 times the nominal tolerances, and slightly higher for the 2.5 case. This could be explained by the fact that Strehl ratio does not increase linearly with decreasing wavefront aberrations, but increases more slowly with RMS error as the RMS error becomes smaller. However, the increase in Strehl ratio, even for relaxed tolerances, has interesting implications for a possible closed-loop aberration correction system where phase diversity is used to estimate a wavefront error that is then used as a control input for the DM. Since an increase in Strehl ratio can still be achieved if the tolerance budgets are multiplied by at least 2.5, it might be possible to achieve a stepwise increase in the Strehl ratio up until a high residual Strehl ratio, starting from a low original Strehl ratio. However, a few test runs showed that no increase in Strehl ratio is achieved on average if the *Deployment and Coarse Alignment* budgets from table 1.3 are applied, which suggest the algorithm performs poorly when wavefront errors are very large.

With regard to convergence, it can be observed from the number of simulations that converged in less than 1000 iterations that convergence becomes slightly slower for higher tolerances.

5.1.6. Unknown TDI-2 Defocus Error

Performance is again presented graphically in 5.6 for configurations that include an unintended TDI-2 defocus error ranging from $0\mu m$ tot $5\mu m$.

From these results, it can be observed that an error in the position of the TDI-2 detector up to $5\mu m$ is unlikely to have any significant detrimental effect on the performance of the phase diversity algorithm. The run times listed also show no noticeable differences between the time required for the algorithm to converge. This means that the positioning tolerance of the TDI-2 detector does not have to be tighter than $5\mu m$. At a later stage, this study should be repeated for even larger error values than $5\mu m$, because pixel pitch generally correlates negatively to the price of a detector.

5.1.7. Gaussian Signal to Noise Ratio

An overview of the performance for configurations with Signal to Noise ratios of 100, 75, 50 and 10 is presented in figure 5.7.

Quite surprisingly, figure 5.7 shows no significant reduction when the SNR was reduced from 100 to 75 and 50 and only a slight reduction in the residual Strehl ratio when the SNR was further reduced to 10. No significant differences in the run times for the different configurations could be observed.

However, it can be observed that the impact of a reduction of the SNR is dependent on the type of scene that is being imaged. The performance was similar for most scenes. For the *Farm* scene type the low SNR case even outperformed the higher SNR case, although this seems to be due to an incidental spike in performance. The SNR = 10 residual Strehl ratios, however, were consistently and significantly lower than those of the other three cases for the *Storm* scene. A possible explanation is the smaller variation per pixel in terms of signal due to the relatively uniform nature of the scene. Because variations are small, its harder to differentiate noisy variation from actual details. The effective SNR of the scene could thus be considered lower.

5.1.8. Contrast

Results of the Monte Carlo analysis for the contrast in terms of the mean photon count per pixel are presented graphically in 5.8.

There was virtually no difference in performance between the configuration with a mean photon per pixel count of 10^4 and the configuration with a mean photon per pixel count of 5×10^3. However, when the photon count was decreased to 10^3 there was an observable decrease in performance, albeit small. This is expected to be due to a decreased SNR and thus a higher impact of noise on the estimation. At this stage, not enough analyses have been performed to provide an accurate estimate of the expected mean photon count that will be experienced during operation. However, when such an estimate is available at a later stage of the project, the result of this parameter study should be reviewed. If the mean photon per pixel count is well above 10^3 no mitigation strategy is required. However, if the mean photon per pixel count is 10^3 or lower it might be necessary to implement a mitigation strategy to prevent a reduction in performance.

5.1.9. Dead Pixels

Although dead pixels are not included in the general simulation tool due to the fact that nothing is known yet about the TDI detectors that will be selected, a sensitivity analysis was performed in the form of a Monte Carlo analysis. During each simulation step, the residual Strehl ratio was calculated for seven distinct cases. A preset probability of a pixel being dead, different for each case, was used to simulate the dead pixels. The cases that have been simulated are 0%, 0.1%, 1% and 10% chance of a pixel being dead. For the 0.1%, 1% and 10% cases additional simulations were run where all zero valued pixels were replaced by the mean of their four direct neighbors. The former simulations are called the uncorrected cases, the simulations that implement averaging of neighbors are called the corrected cases. An overview of the performance of each of the configurations is presented in figures 5.9 and 5.10.

It can be seen that the performance of the algorithm deteriorated quickly with increasing probability of dead pixels. A 0.1% chance of a dead pixel already resulted in a significant decrease in residual Strehl ratio. However, the graphs on the right side of the figure show that performance using the measurements corrected through interpolation at the locations of dead pixels was virtually identical to the performance of the 0% dead

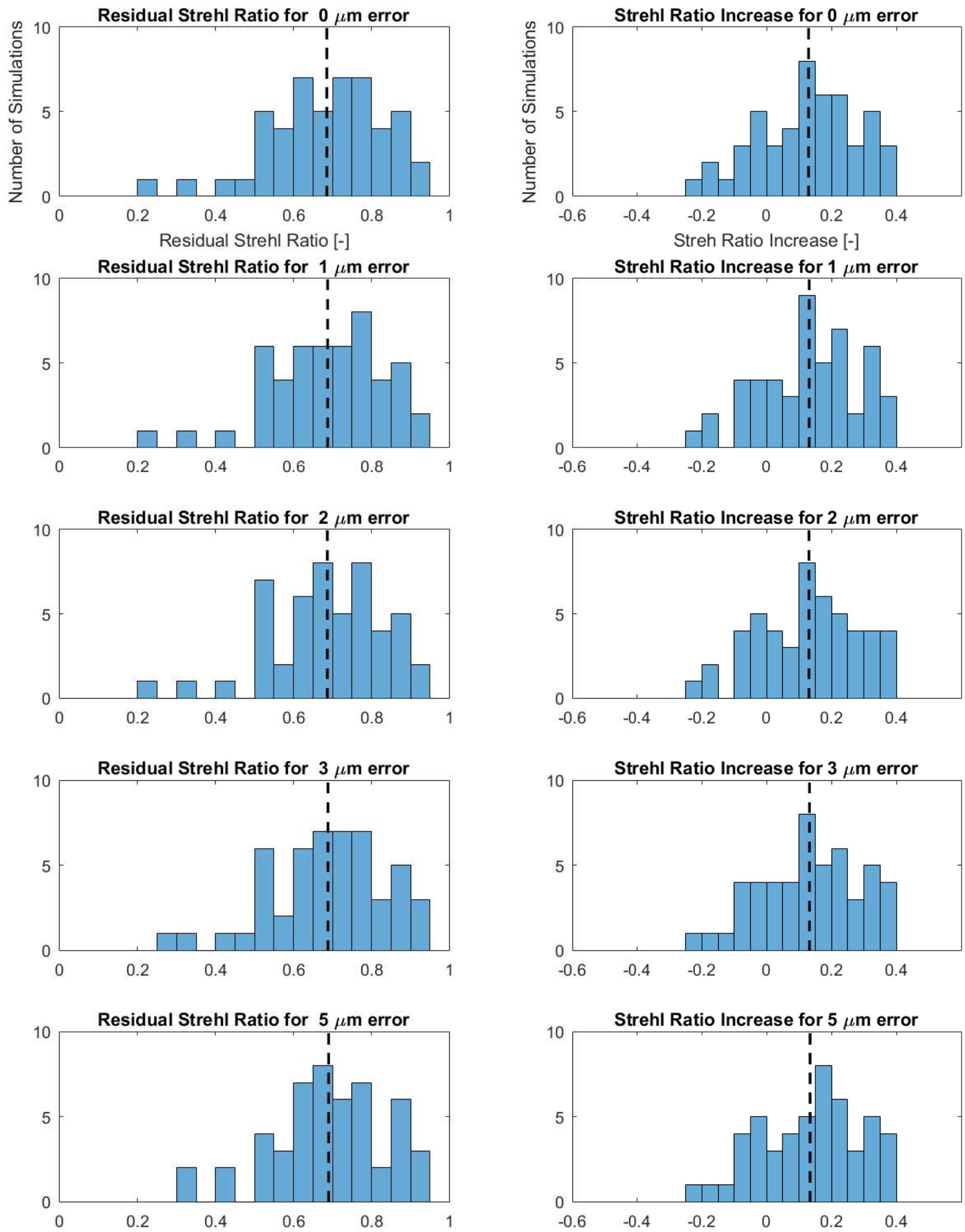

Figure 5.6: Residual strehl ratio and strehl ratio increase distribution resulting from the simulations.

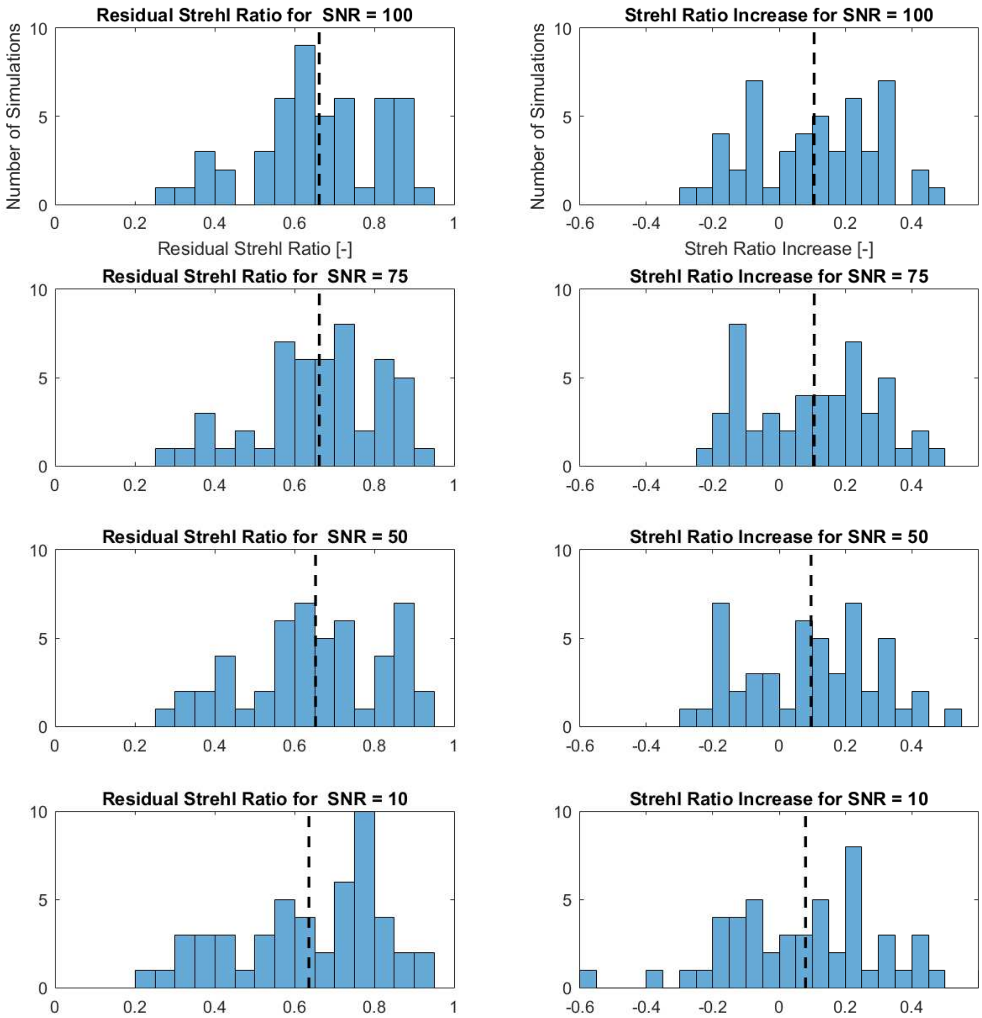

Figure 5.7: Residual strehl ratio and strehl ratio increase distribution resulting from the simulations.

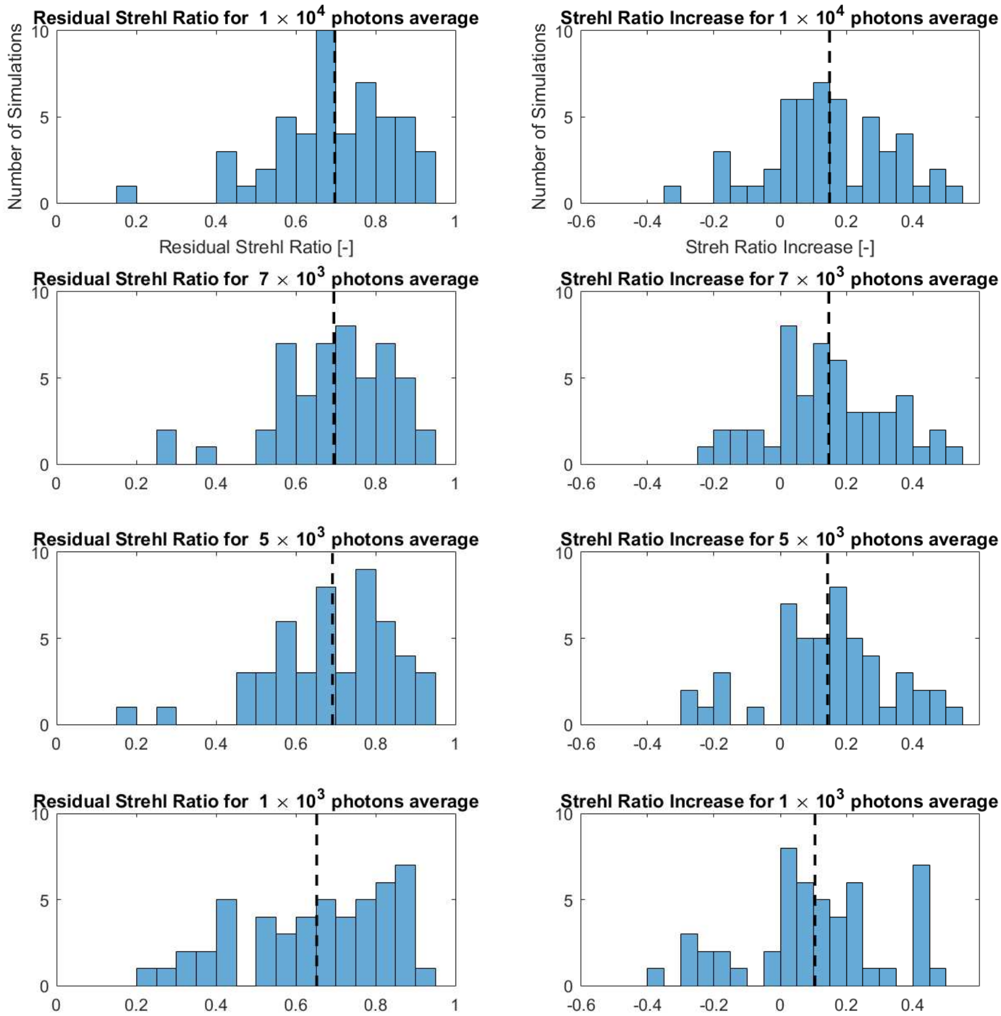

Figure 5.8: Residual strehl ratio and strehl ratio increase distribution resulting from the simulations.

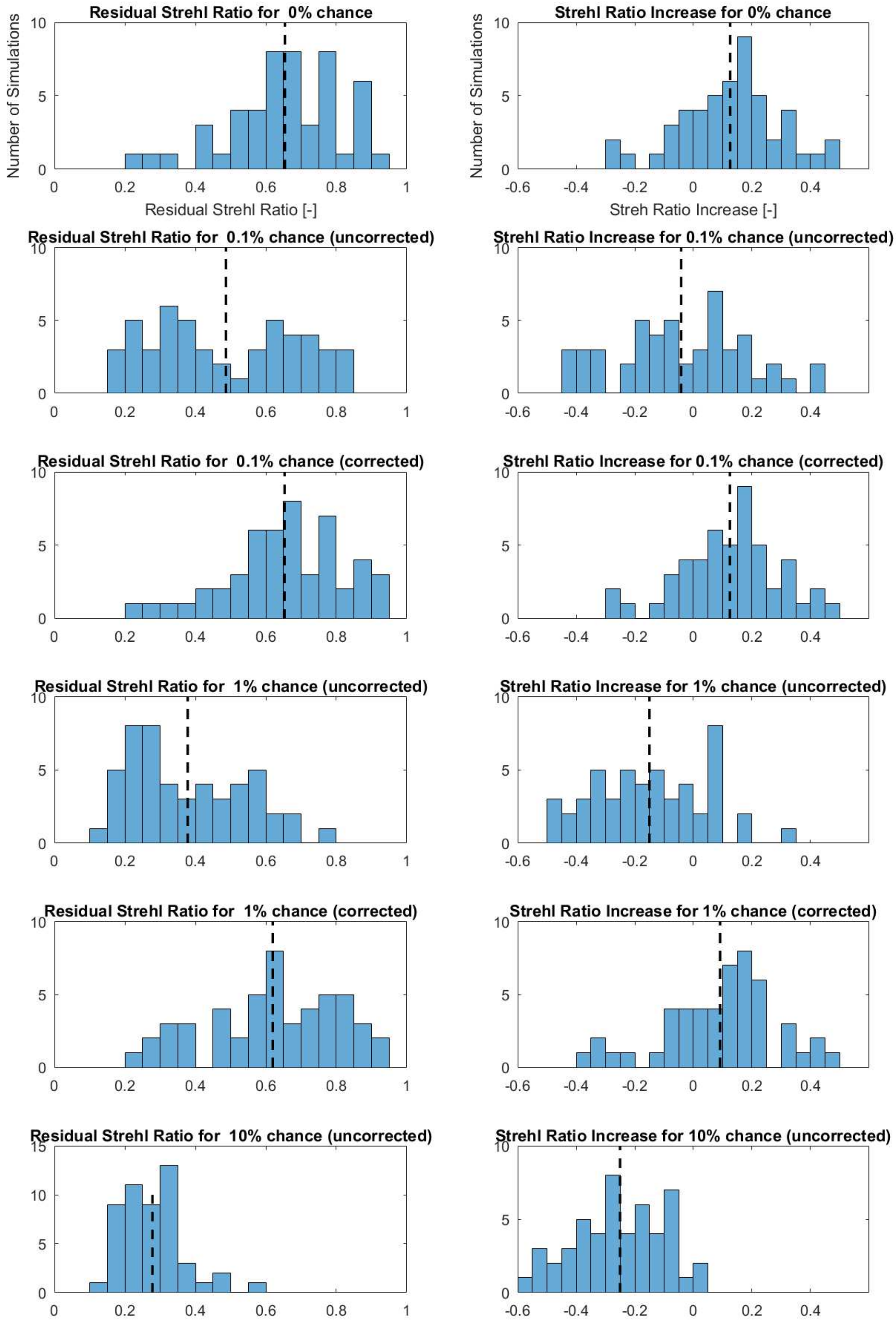

Figure 5.9: Residual strehl ratio resulting from the simulations for both uncorrected as well as corrected dead pixels (plot 1 of 2).

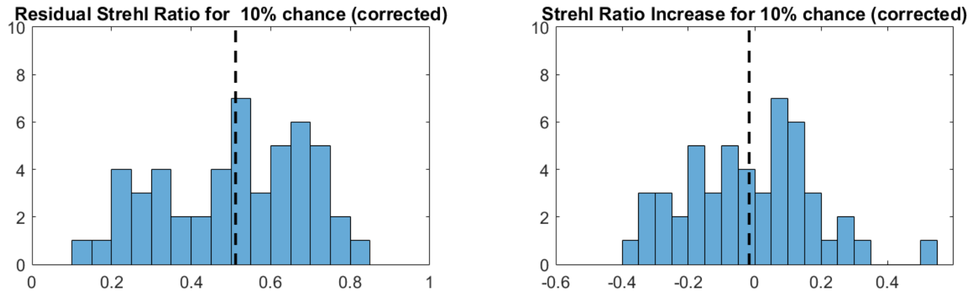

Figure 5.10: Residual strehl ratio resulting from the simulations for both uncorrected as well as corrected dead pixels (plot 2 of 2).

pixel case up until a 0.1% change of a dead pixel. Even for a 1% probability, the decrease in average residual Strehl ratio was only about 0.1 compared to the 0% case. This means that the performance of the algorithm is not significantly impacted when the percentage chance of a dead pixel is below 1%. If the chance of a dead pixel is found to be higher than 1% in a later stage of the design, this analysis should be repeated to quantify the loss in performance.

5.1.10. Scene Type

The results of the comparison study for the *Farm*, *Sea*, *Storm*, *Mountains* and *City* scene types are presented in histogram form in figure 5.11.

From these results it can be observed that the phase diversity algorithm performed best for *Farm* and *Mountains* scene types and worst for the *Sea* and *Storm* scene types. This suggests that the algorithm works better when smooth but colorful scenes with several distinct features are being imaged. The reasons for this might be the same as the reasons discussed in subsection 5.1.1, repeated here:

1. Due to the uniform nature of the scenes differences in measured values between adjacent pixels is smaller than in other scene types. The ratio between the average difference between two pixels over the image noise is thus effectively smaller. This increases the impact of noise

2. Distinct features in a scene make it easier to identify the Point Spread Function footprint. As an example, the limit case of individual bright starts against a dark background is taken. In these images, the shape of the Point Spread Function is very recognizable.

The poor performance for the *City* scene type is attributed to the fact that the subframe selected for the application of phase diversity has very bright borders and therefore suffers from severe edge effects. It can also be seen that convergence was also significantly slower for the the *Storm*, *Sea* and *City* scene types compared to the natural *Mountains* and *Farm* scene types. It is therefore expected that the highest system performance is achieved if the phase diversity algorithm is applied to smooth natural scenes as much as possible. This should be considered in the final design of the aberration correction strategy.

However, in the case of the *Sea*, *Storm* and *City* scene types the algorithm still achieved a residual Strehl ratio that is higher than the original Strehl ratio on average.

5.1.11. Zernike Order

The performance for the configurations that use Zernike polynomials up to order 8, 7, 6, 5, 4, 3, 2 and 1 respectively for estimation of the wavefront error are presented in figures 5.12 and 5.13.

Looking at these results, it can be seen that there were significant differences in performance between the different configurations, with a peak at Zernike order 4. It is expected that using Zernike polynomials up to order 4 provides a good trade-off between achieving enough fitting accuracy and prevention of overfitting. It would thus be a logical choice to use Zernike polynomials up to order 4 for construction of the wavefront error. However, looking at the optical system requirements it can be seen that one of the requirements for the system is that the RMS of the wavefront error in terms of the Optical Path Difference expressed in wavelengths $\lambda_0 = 450nm$, should be below 0.07. Therefore, it should be verified that the fitting error when using Zernike polynomials up to order 4 is well below $0.07\lambda_0$.

In order to check this, a decomposition algorithm was constructed that uses a gradient-based optimization scheme to find the set of Basis functions that lead to the lowest Least Squares fitting error. Once this set

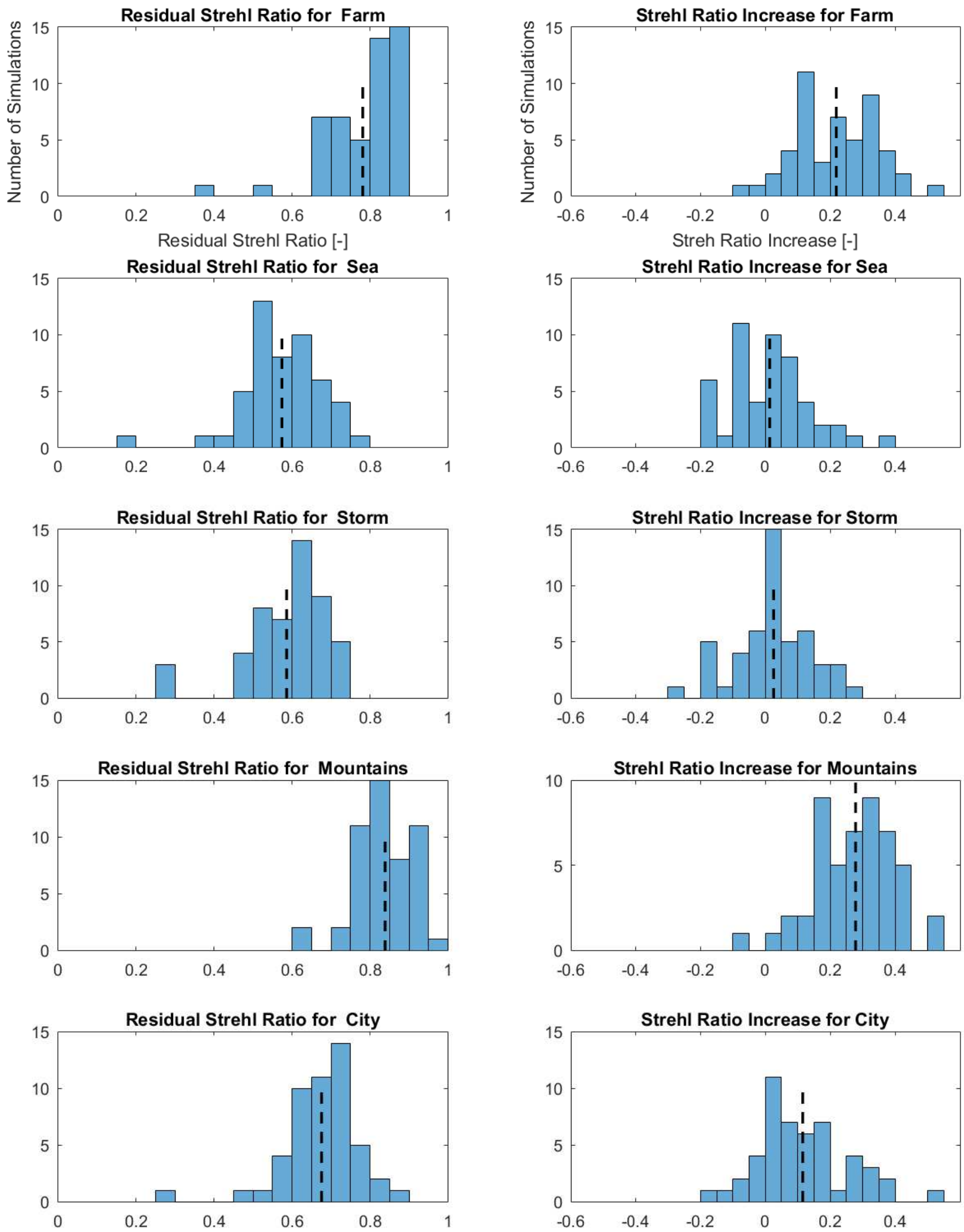

Figure 5.11: Residual strehl ratio and strehl ratio increase distribution resulting from the simulations.

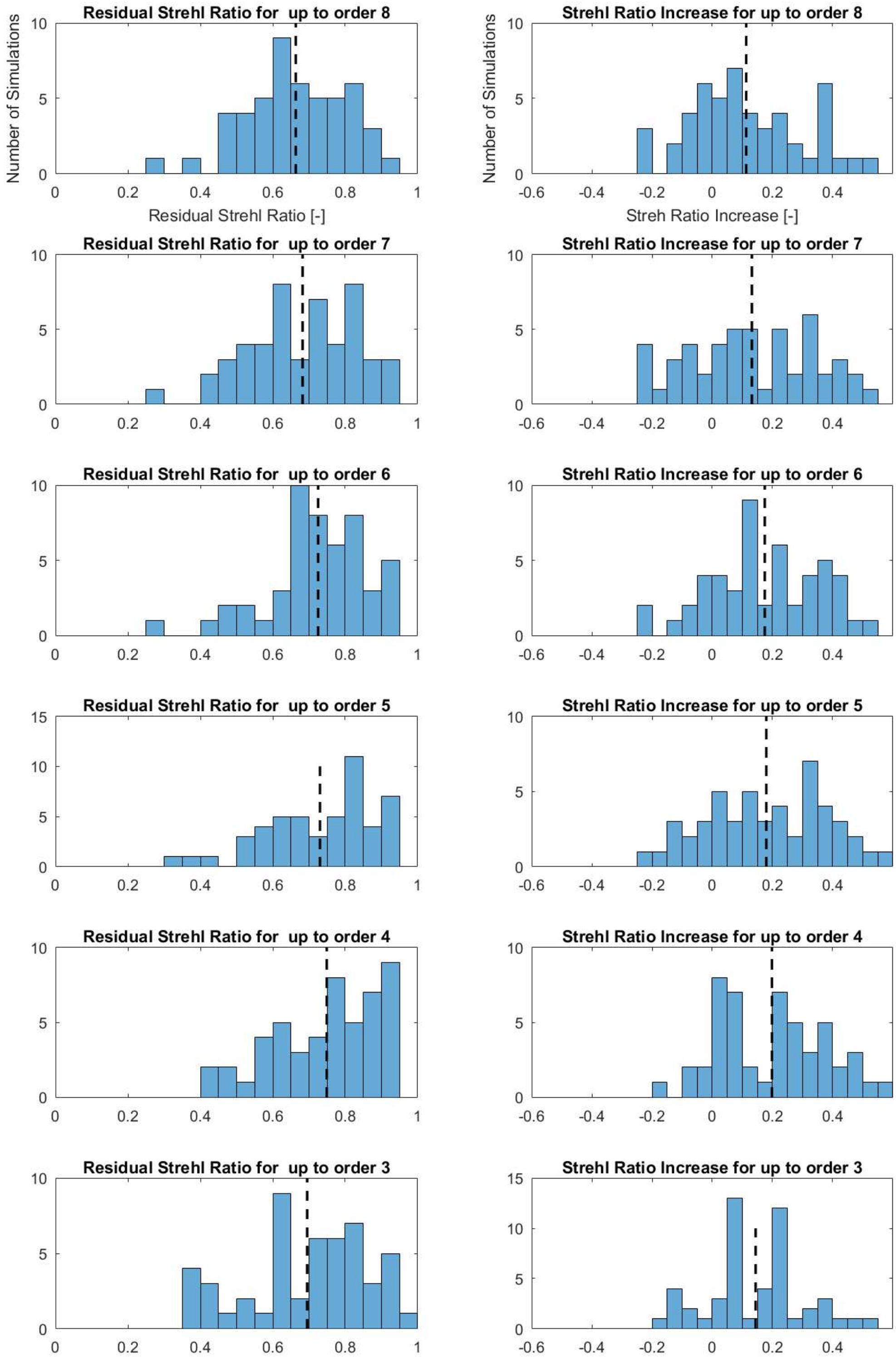

Figure 5.12: Residual strehl ratio resulting from the simulations for the number of Zernike polynomials (plot 1 of 2).

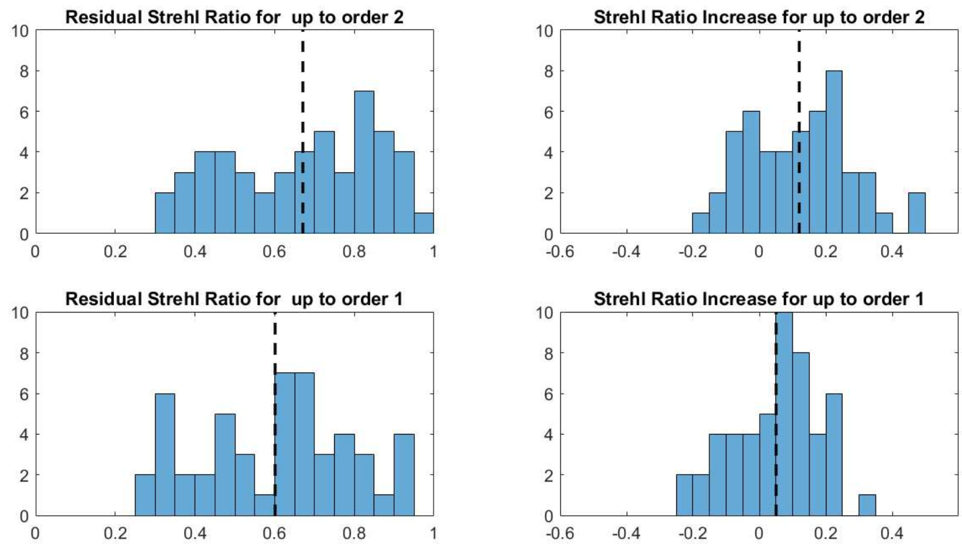

Figure 5.13: Residual strehl ratio resulting from the simulations for the number of Zernike polynomials(plot 2 of 2).

of Basis functions was found, a fitting was constructed and the residual error between the actual wavefront which measured in terms of RMS error expressed in λ_0. The basis functions used for decomposition were the same as the basis functions for the phase diversity algorithm, i.e. global Zernike polynomials with the global tip/tilt and piston terms replaced by tip, tilt and piston terms for each of the individual M1 segments.

Using FORTA, 50 different wavefront errors were generated. For each of these wavefront errors, the decomposition algorithm was executed twice. Once using Zernike polynomials up to order 5 and once using Zernike polynomials up to order 4. The resulting RMS distributions are presented in figure 5.14. As can be observed from the figure the residual error after fitting was well below a factor 20 smaller than $0.07\lambda_0$ in all cases. It can even be observed that the error was lower when using Zernike polynomials up to order 4 than when using Zernike polynomials up to order 5. However, this must be a result of the performance of the fitting algorithm, which apparently performs better when fewer basis functions are used, since the configuration with polynomials up to order 5 should by definition result in an equal or lower fitting error if a perfect fitting algorithm is used.

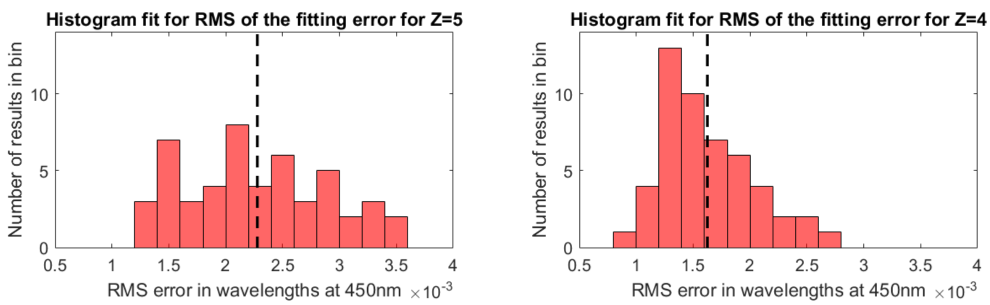

Figure 5.14: RMS in terms of $\lambda_0 = 450nm$ of the residual wavefront error after fitting using Zernike polynomials up to order 5 (left) and up to 4 (right).

Finally, it was decided that using Zernike polynomials up to order 4 is the preferred setting for the algorithm. This was verified later in the combined parameter tests in section 5.1.16

5.1.12. Learning Rate

The average residual Strehl ratios that have resulted from the Monte Carlo analysis with varying learning rate κ, which is defined in section 3.2.4. The results for learning rates 1×10^{-4}, 5×10^{-4}, $1 \cdot 10^{-3}$, 5×10^{-3} and 1×10^{-2} are presented in histogram form in figure 5.15.

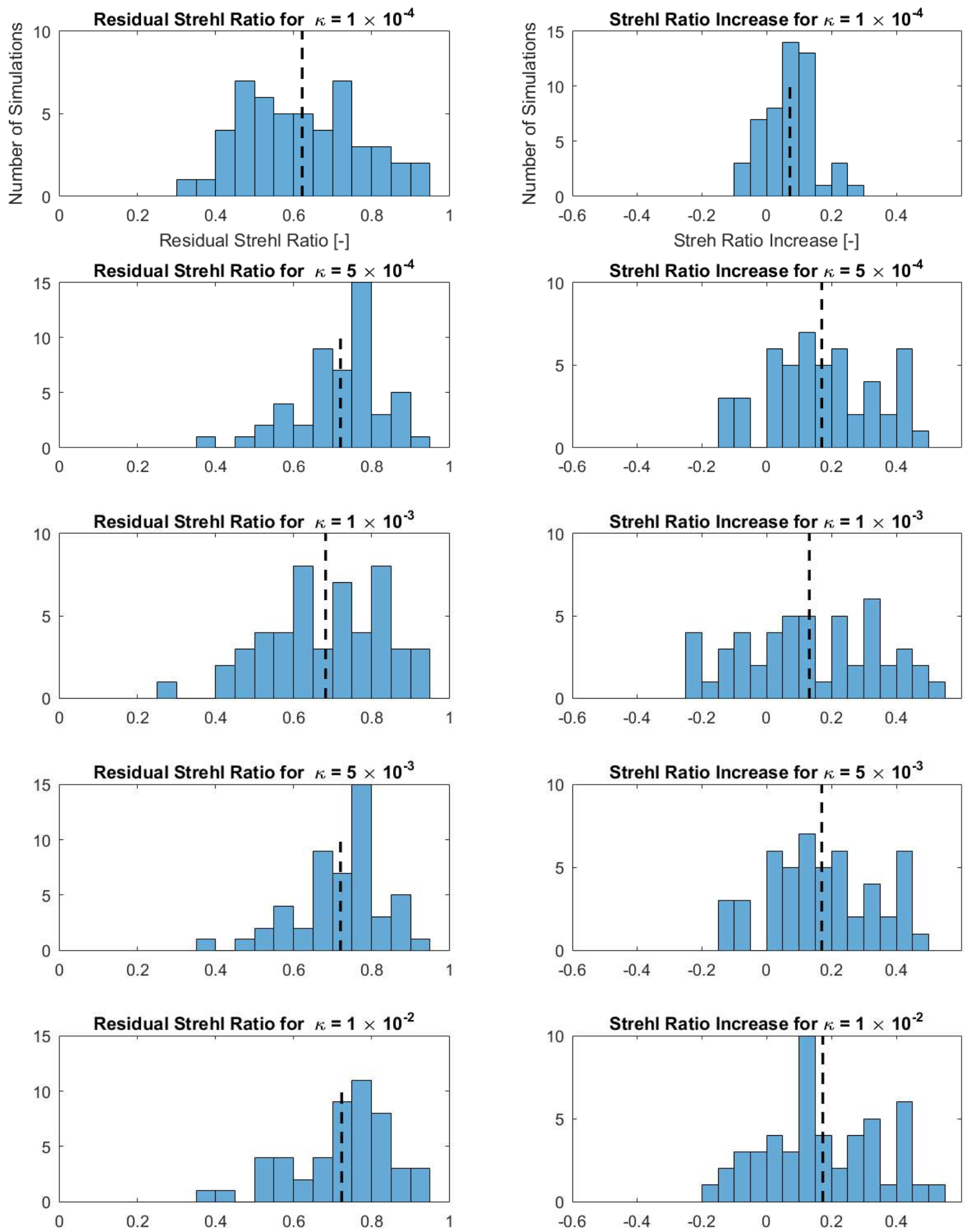

Figure 5.15: Residual strehl ratio resulting from the simulations for the learning rate.

It can be observed that the performance in terms of Strehl ratio was similar for most learning rates, with the exception of $\kappa = 1 \times 10^{-4}$ and $\kappa = 1 \times 10^{-3}$ for which a significantly lower average residual Strehl ratio can be observed. The difference becomes apparent when looking at the run times for the different learning rates. It can be seen that the configuration with a learning rate of 1×10^{-2} had a convergence time that was on average more than 6 times faster than the average convergence time of all the other configurations. This is attributed to the more aggressive convergence behavior resulting from a higher learning rate. It was therefore decided to use this learning rate during further analysis of the phase diversity algorithm.

5.1.13. Number of Wavelength Samples

The numbers of wavelength samples that were simulated are 1, 3, 7, 11 and 15. Information about the performance of the configuration is once again represented graphically in figure 5.16.

It was expected that increasing the number of wavelength samples used would increase the accuracy of the estimate at the cost of a linear increase of the computation time with the sample number. This is due to the fact that a gradient term has to be calculated for every wavelength sample. Looking at the run times an expected pattern can be observed, computation time per iteration increased more or less linearly with the number of sample wavelengths used. With respect to iterations, it can be seen that the configuration that used only a single wavelength sample required slightly more iterations to converge on average than the other four configurations. Among the other four configurations, there was no significant difference in terms of the number of iterations required.

Looking at the performance in terms of the residual Strehl ratio, the same pattern can be observed. While the single sample configuration was significantly outperformed by the other four configurations, only a slight difference was found among the other four in terms of performance. This was contrary to the expectations. This seems to suggest that using a broadband phase diversity algorithm does indeed make a significant difference in performance, but increasing the number of wavelength samples beyond three does not result in a further increase in performance. It was therefore decided to set the number of wavelength samples to 3 since it provides the optimum balance between performance in terms of Strehl ratio and convergence speed.

5.1.14. Subframe size

The Monte Carlo analysis done for the subframes with side lengths of 256, 128 and 64 pixels resulted in the performance presented in figure in figure 5.17.

While it can be observed from the table that the time per iteration was much higher for the larger subframe size, increasing the size of the subframe did have a noticeable positive effect on the performance of the algorithm. It can be seen that the configuration using a subframe with a side length of 256 pixels consistently outperformed the configurations with smaller side lengths. It is hypothesized that using a larger subframe reduces the impact of edge effects.

Because of the stringent requirements on the Strehl ratio and maximum RMS value for the wavefront error it was decided to further investigate the effect of increasing the subframe size to 256×256 pixels, which is further discussed later in this section. Due to the limited size of the images taken from the AVIRIS dataset, testing for even larger subframe size lengths was not possible, but it is possible that a further increase in the subframe size could lead to even higher performance at the cost of extra computation time.

5.1.15. Apodization

Five configurations have been simulated for configurations with apodization ratios of 0.0, 0.25, 0.5, 0.75. The results can be found in figure 5.18.

Looking at the average run times of the configurations it can be observed that, except for the poor convergence behavior of the 0.25 apodization ratio configuration, convergence behavior and iteration count were similar between the different configurations. In terms of residual Strehl ratio, it can be observed that both the 0.0 as well as the 1.0 ratio configuration stand out among the rest due to superior performance. It is suspected that the reason for this is the absence of sharp edges in both configurations since edge effects due to the implicit assumption of continuity by MATLAB's 2D FFT (*fft2*) algorithm are actively removed for the 0.0 ratio configuration using the method described in section 3.2.2. The 1.0 ratio configuration has no sharp edges due to the low steepness in the edges of the apodization window.

Since the performance of the 0.0 and 1.0 ratio configurations is very similar, it was decided to continue without apodization applied to the subframe. The reason for this is that a series of preliminary, non-documented tests showed the optimum apodization ratio to be very dependent on the settings parameters, while the edge treatment method developed by Mahmood showed excellent performance in all cases.

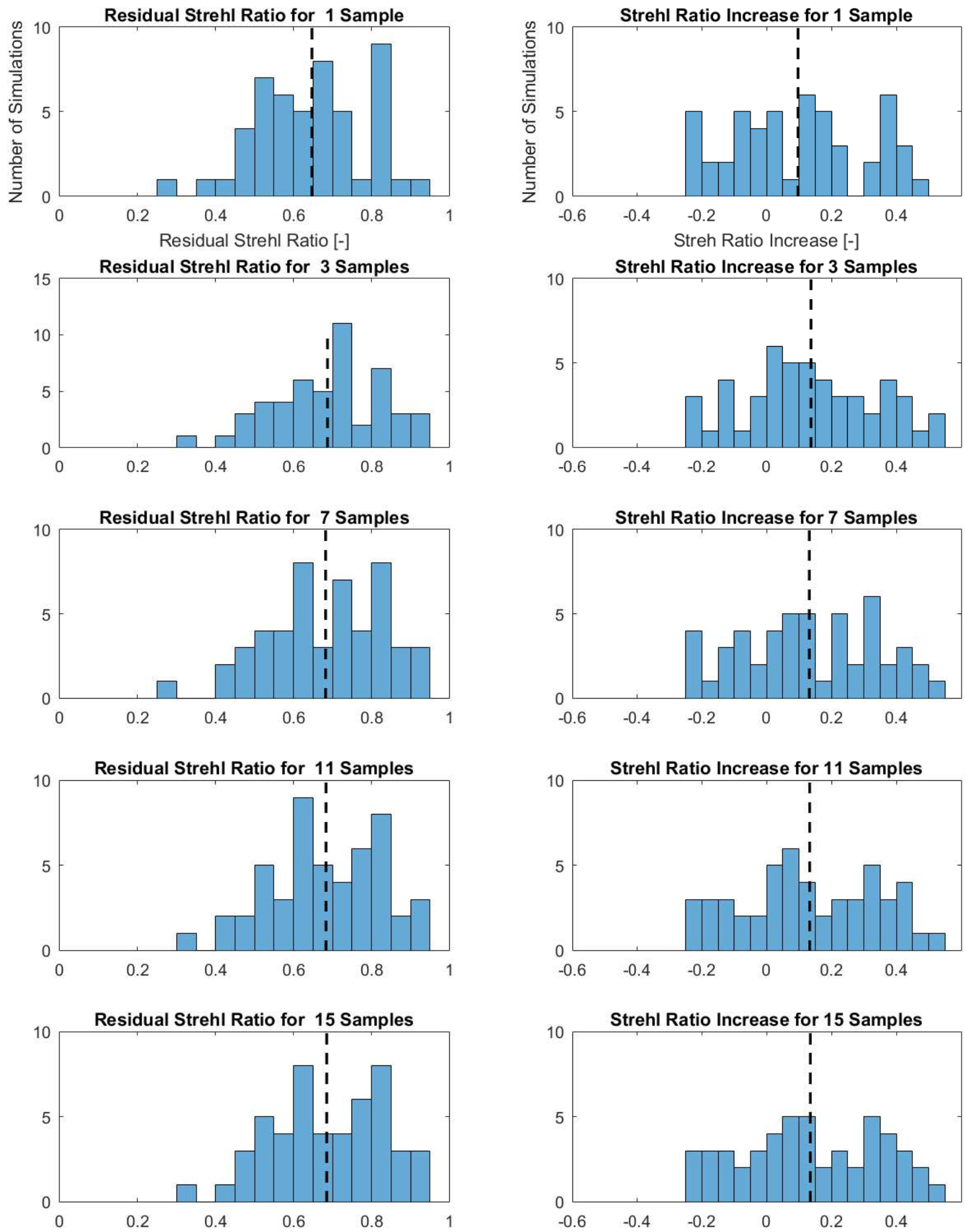

Figure 5.16: Residual strehl ratio resulting from the simulations for the number of wavelength samples.

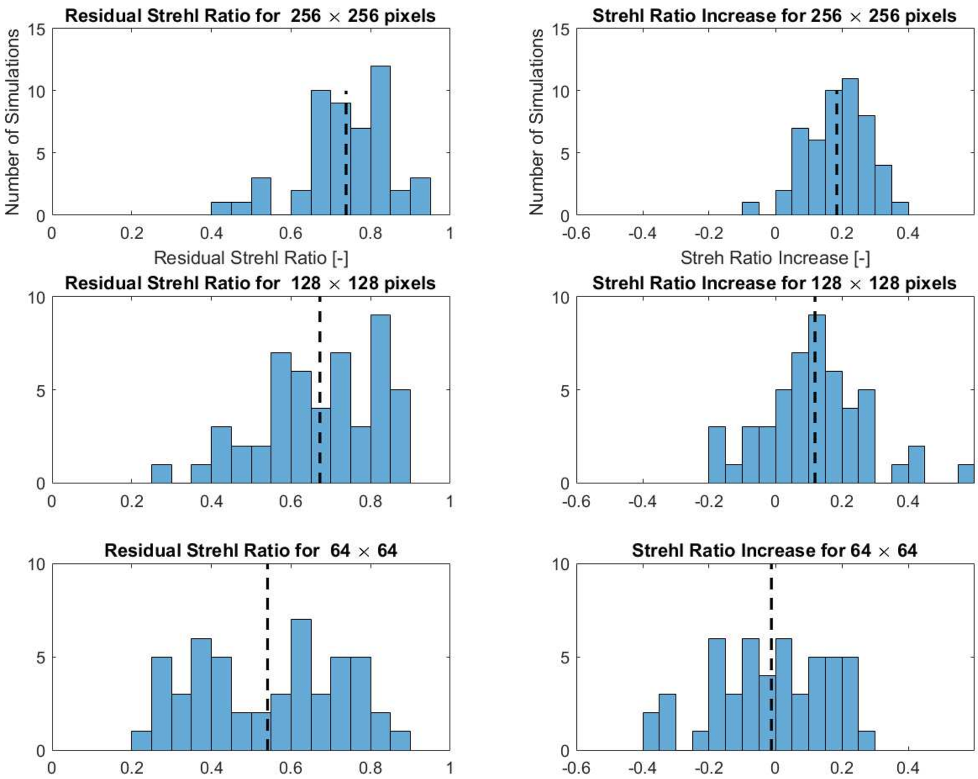

Figure 5.17: Residual strehl ratio resulting from the simulations for the subframe size.

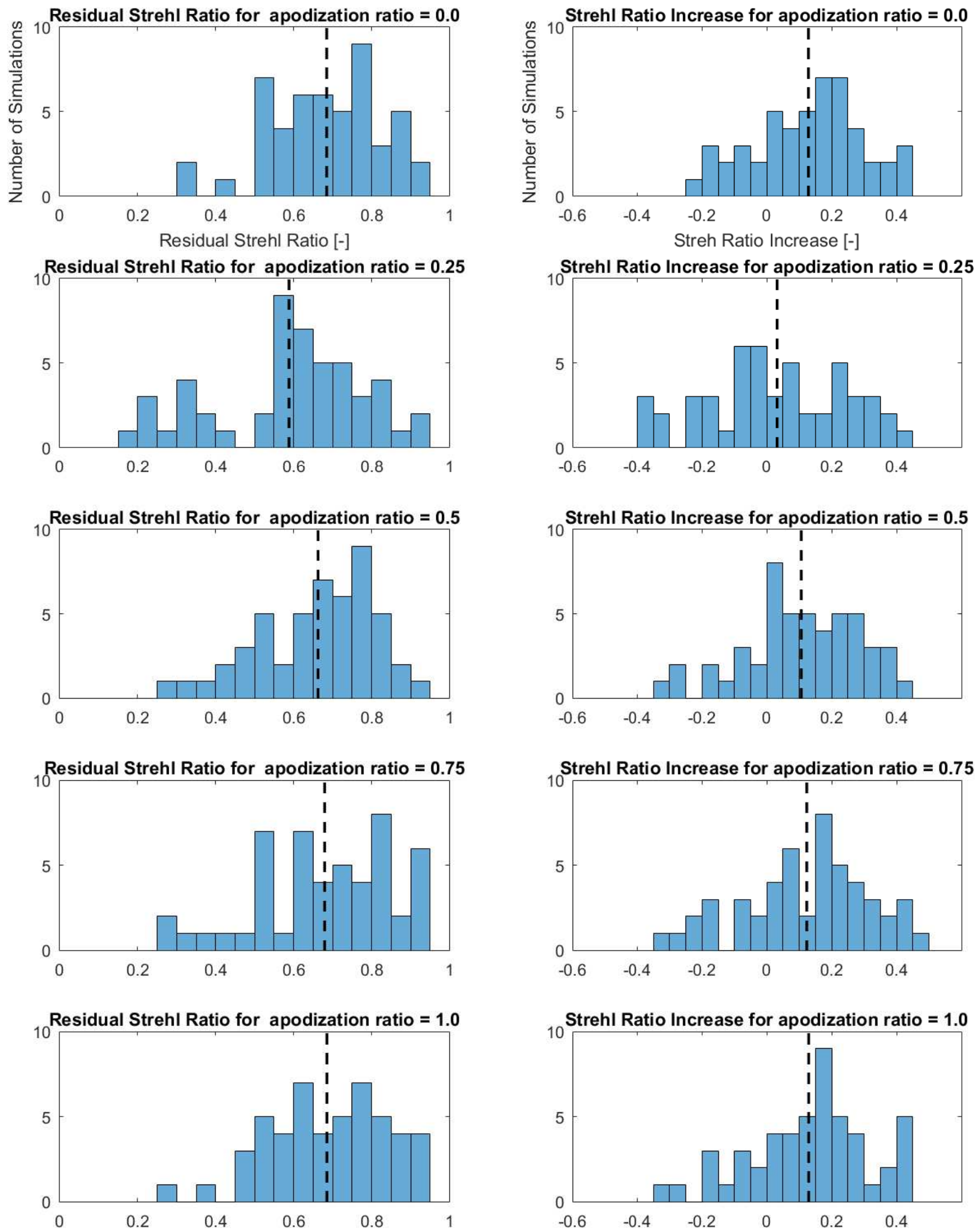

Figure 5.18: Residual strehl ratio resulting from the simulations for the apodization ratio.

Table 5.2: Configurations that are simulation in the combined parametric study.

Configuration no.	**d** (TDI-2 defocus in mm)	**N** (subframe side length in pixels)	**L** (no. of wavelength samples)	κ (Learning rate)
1	0.25	128	7	$1 \cdot 10^{-3}$
2	0.25	256	7	$1 \cdot 10^{-3}$
3	0.25	256	3	$1 \cdot 10^{-3}$
4	0.25	256	7	$1 \cdot 10^{-2}$
5	0.25	256	3	$1 \cdot 10^{-2}$
6	0.25	256	7	$1 \cdot 10^{-3}$
7	0.25	256	3	$1 \cdot 10^{-3}$
8	0.25	256	7	$1 \cdot 10^{-2}$
9	0.25	256	3	$1 \cdot 10^{-2}$

5.1.16. Combined

Up until now the parametric studies only studied the impact that changing a single parameter had on the overall performance of the algorithm. Since testing every possible combination of parameters was not viable due to the vast computational time that would be required, a selected number of configuration was compared through a Monte Carlo analysis with the aim of finding the parameter set that yields the optimum performance. The criteria for selection of these parameters were as follows:

1. The parameter study results show that performance is sensitive to changes in the parameter
2. The parameter changes lead to a design that could potentially meet the non-optical requirements as well (this is why the 3 detector configuration was left out for example)
3. The parameter changes are known to be realistic (for example, because of this criterion pixel pitch values of below $5\mu m$ and increasing the SNR budget were left out)

Based on these criteria the following parameters were selected:

1. The TDI-2 defocus (measured in mm). Changing this parameter does not add additional cost and has no consequence for any other subsystem.
2. The maximum Zernike order. A software setting that does not require any changes to the design.
3. The learning rate. Also, a software setting that requires no changes.
4. The number of wavelength samples. Software setting.
5. The size of the subframe to which the algorithm is applied. Software setting.

Several combinations of the optimum values found in the parametric studies were selected for the simulations. An overview is provided in table 5.2. Apart from the parameters mentioned here, all parameters values were identical to the values used for the baseline configuration described in table 4.1. It can be observed that for this first round of combined parametric simulations the TDI-2 defocus was kept constant at $0.25mm$, which is the optimum value found in the TDI-2 defocus study performed earlier. The configurations listed in the table were compared through a Monte Carlo analysis with the same set up as for the individual parameter studies: 50 runs were executed per configuration, distributed evenly over the five scene types. The performance for each of the configurations is presented graphically in figures 5.19 5.20.

It can be seen from these results that the highest performance in terms of residual Strehl ratio was achieved by configuration number 9. Results of this combined study were compared to the results of the learning rate study presented in figure 5.15, the subframe size study presented in figure 5.17 and finally the Zernike order study presented in figures 5.12 and 5.13. It was noted that the results do not show a noticeable improvement compared to the best results from these individual parameter studies. It was therefore decided to take the configurations with the best performance, configuration 9, and run a second Monte Carlo analysis in which the TDI-2 defocus was varied. The configurations that were tested in this analysis are presented in table 5.3. Results of this second combined study are presented in table C.16.

From these results two interesting observations can be made from these results:

1. The $0.5mm$ TDI-2 defocus configuration with subframe size $n = 256$ provided the best performance

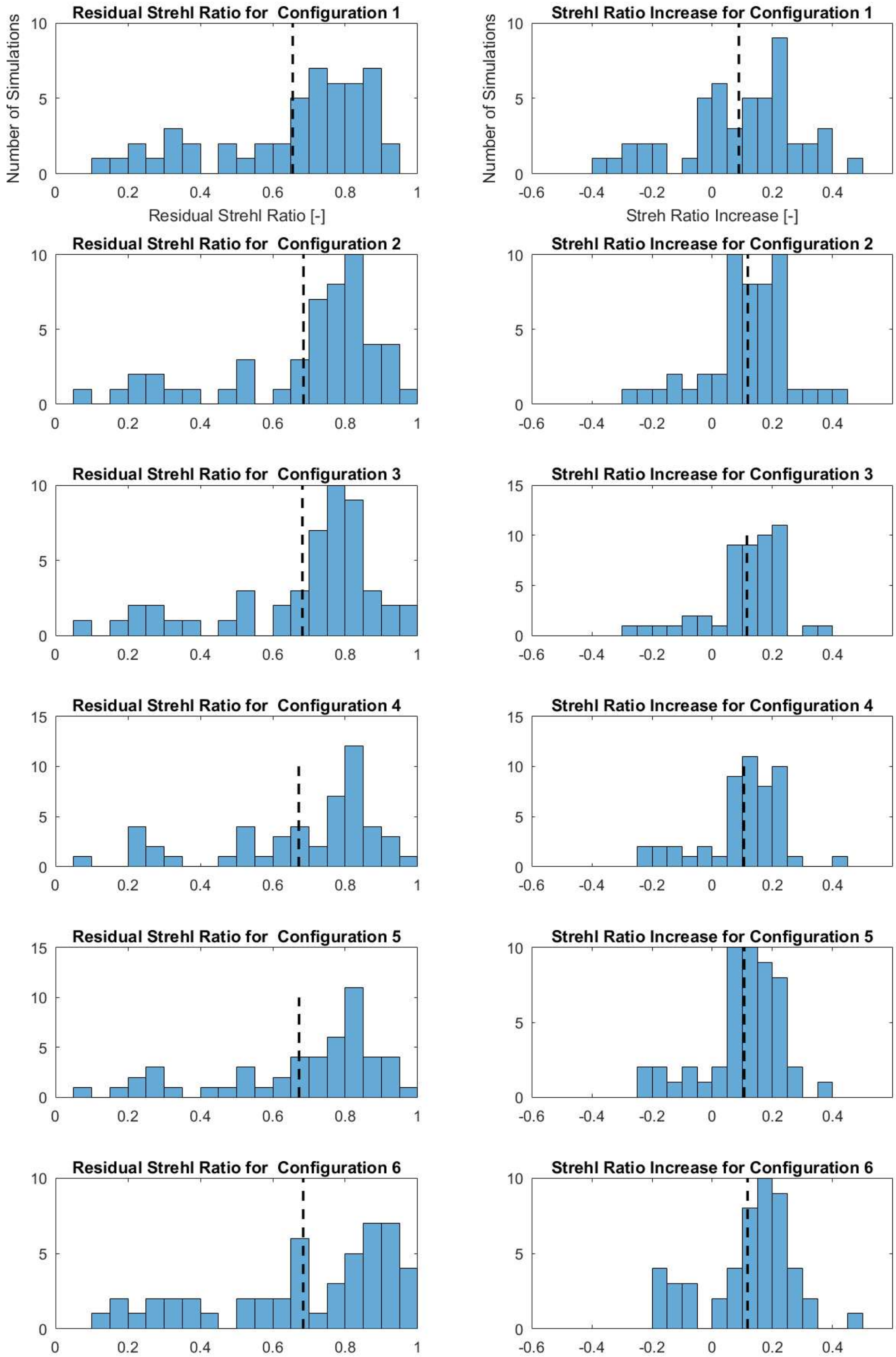

Figure 5.19: Residual strehl ratio resulting from the simulations for the combined configurations (plot 1 of 2).

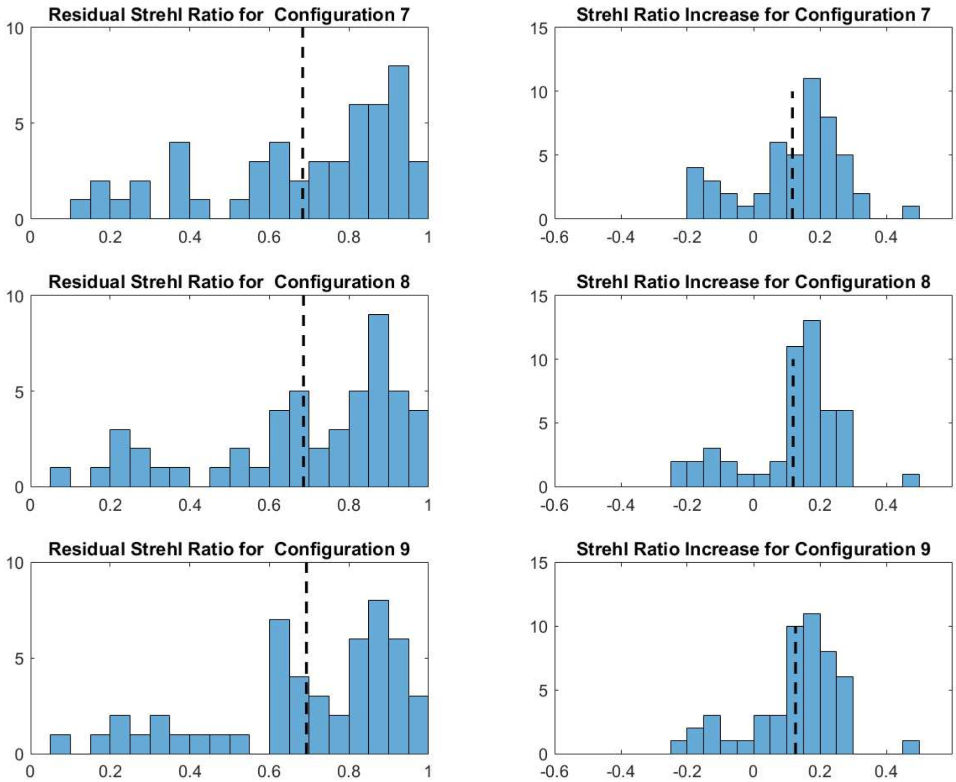

Figure 5.20: Residual strehl ratio resulting from the simulations for the combined configurations (plot 2 of 2).

Table 5.3: Configurations that are simulation in the second combined parametric study.

Configuration no.	**d** (TDI-2 defocus in mm)	**N** (subframe side length in pixels)	**L** (no. of wavelength samples)	κ (Learning rate)
1	0.25	128	3	$1 \cdot 10^{-2}$
2	0.25	256	3	$1 \cdot 10^{-2}$
3	0.5	256	3	$1 \cdot 10^{-2}$
4	0.75	256	3	$1 \cdot 10^{-2}$
5	1	256	3	$1 \cdot 10^{-2}$

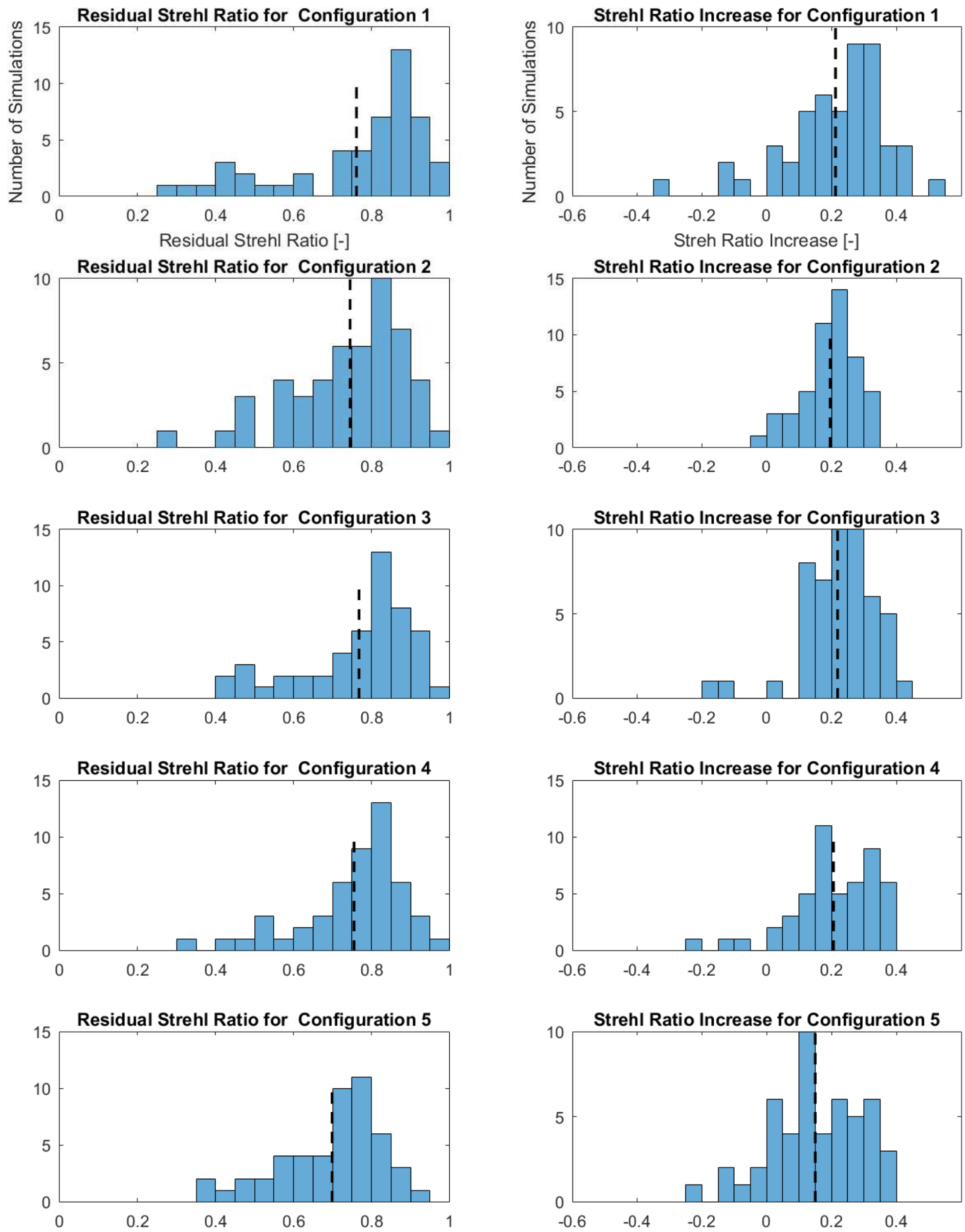

Figure 5.21: Residual strehl ratio resulting from the simulations for the combined configurations.

2. Performance of the Baseline configuration came in a close second in terms of Strehl ratio. However, when it came to run times, the baseline configuration with $0.25mm$ and $n = 128$ outperformed the other configurations by a factor of approximately 2

It was therefore decided to select two configurations for further analysis. An overview of both selected configurations is provided in tables 5.4 and 5.5 respectively.

Table 5.4: Parameter settings for phase diversity algorithm configuration 1.

Parameter	**Value**	**Unit**
Number of detectors	2	-
TDI-2 defocus	0.5	wavelengths
Phase Diversity Subframe Size	128	pixels
Detector Pixel Pitch	5	μm
Zernike Polynomials	15 (= 24 basis functions)	-
Apodization ratio	0	$\frac{pixels_{apodized}}{pixels_{unapodized}}$
Learning Rate κ	0.01	-
Max Number of Iterations	1000	-
Step Tolerance (Fraction of initial Metric Value)	$1 \cdot 10^{-7}$	-
Number of wavelength samples	3	-

Table 5.5: Parameter settings for phase diversity algorithm configuration 2.

Parameter	**Value**	**Unit**
Number of detectors	2	-
TDI-2 defocus	0.5	wavelengths
Phase Diversity Subframe Size	256	pixels
Detector Pixel Pitch	5	μm
Zernike Polynomials	15 (= 24 basis functions)	-
Apodization ratio	0	$\frac{pixels_{apodized}}{pixels_{unapodized}}$
Learning Rate κ	0.01	-
Max Number of Iterations	1000	-
Step Tolerance (Fraction of initial Metric Value)	$1 \cdot 10^{-7}$	-
Number of wavelength samples	3	-

5.2. Multispectral Data

The effect of inclusion of multispectral data on performance was estimated by using the setup described in section 4.2. A Monte Carlo Simulation analysis was performed comparing four configurations, the two configurations described in the previous section without using multispectral data and the same two configurations but with the inclusion of multispectral data in the algorithm. Information about the performance can be found in figure 5.22. The results are tabulated in appendix section C.2.

From the results of the Monte Carlo analysis, it can be seen that on average the performance of the phase diversity algorithm slightly decreased, although negligible, when the multispectral data was included in the calculation. While this may seem improbable, it must be noted that the broadband phase diversity metric is based on the grey world assumption. It might be possible that the theoretical optimum grey world spectrum that would lead to the best performance is not correlated with the average spectrum of the image. Due to time constraints, it was decided that this correlation would not be investigated further within the scope of this project.

Based on the results of this study it was concluded that performance cannot be increased by using just the multispectral measurement averages to estimate the grey world spectrum, although further research might indicate a different way in which multispectral data can be used for improving the phase diversity algorithm performance.

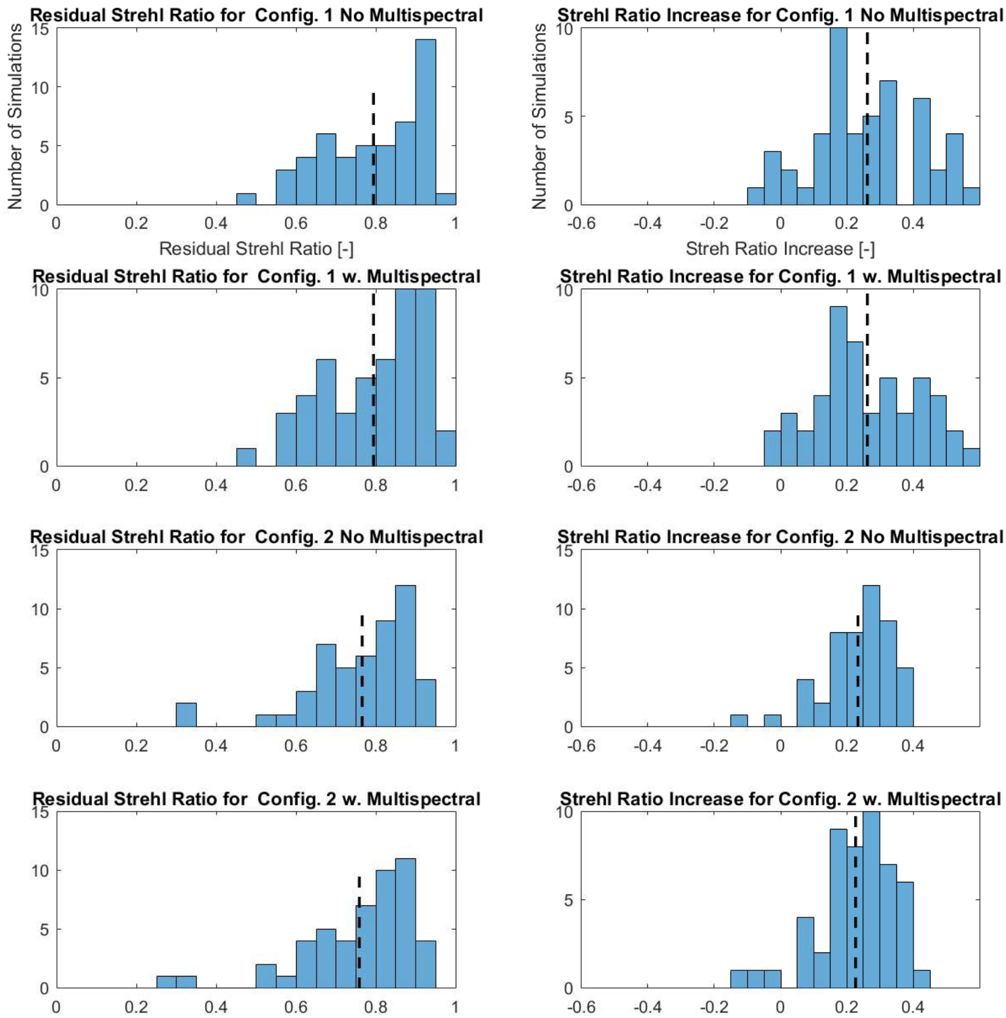

Figure 5.22: Residual strehl ratio resulting from the simulations for the Multispectral channel in-the-loop.

5.3. Subframe Selection

While two configurations were selected based on the results of the parametric studies, the limited size of the AVIRIS pictures made application of the subframe selection algorithms to a frame of size 256 × 256 infeasible. It was therefore decided to test the algorithms using only configuration 1, which applied phase diversity to a subframe of size 128 × 128. The average residual Strehl ratios as well as the run times and iteration counts for the simulations of subframe selection algorithms *Center Frame*, *Bright Peak* and *Dark Borders* can be found in figure 5.23. The results are tabulated in appendix section C.3.

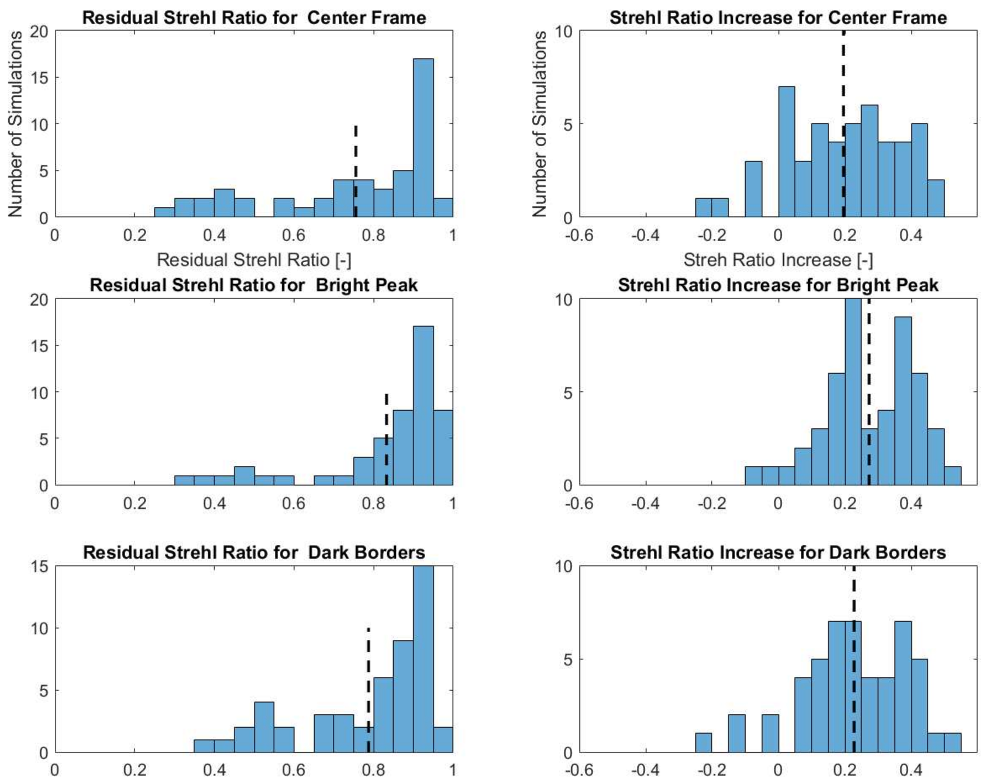

Figure 5.23: Residual strehl ratio resulting from the simulations for the selection algorithm.

Run times and iteration counts were virtually identical for all subframe selection algorithms. However, large differences can be observed between the residual Strehl ratios the three subframe selection algorithms. While both the *Bright Peak* and *Dark Borders* algorithms performed better than the original *Central Frame* algorithm, the *Bright Peak* performed significantly better than the *Dark Borders* algorithm. It is expected that this is due to the fact that selecting a point of high intensity at the center directly increases the ratio of the center intensity over border intensity for every point near the image borders. The *Dark Borders* algorithm however, minimizes the average intensity at the image borders. It could very well be that while the average intensity is low, some local peaks are present close to the borders, which would negatively impact performance.

It was decided to use the *Bright Peaks* algorithm for subframe selection during the closed-loop and open-loop performance tests.

5.4. Open-Loop Performance

To assess the performance of the final two configurations, which are the configurations presented in tables 5.4 and 5.5 without the inclusion of multispectral data in the estimation process and with the *Bright Peaks* algorithm for selection of the subframe, a Monte Carlo analysis of 400 simulation runs was executed. The results of the analysis are presented in the form of histograms that show the residual Strehl ratio as well as the Strehl ratio increase in figure 5.24. A histogram representation of the residual Root Mean Square error as well as the RMS error decrease is presented in figure 5.24. In these two figures, the lower and upper limit for the residual Strehl ratio and residual RMS error respectively, dictated by requirements, have been plotted as a solid red line. In addition to these results it was found that for configuration 1 and 2 the percentage of simulation runs that resulted in an estimation accuracy compliant with requirements are = 85.2% and = 82.8% respectively in terms of residual Strehl ratio, and = 79.4% and = 75.6% in terms of the residual RMS error. The values for the residual Strehl ratio were on average higher than in earlier simulations, this is expected to be due to the extra zero padding that was used for the calculation of the PSFs in this case in order to increase the accuracy of estimation. The absolute values of the Strehl ratios presented here are thus expected to be more accurate than the Strehl ratios presented earlier. The results are tabulated in appendix section C.4.

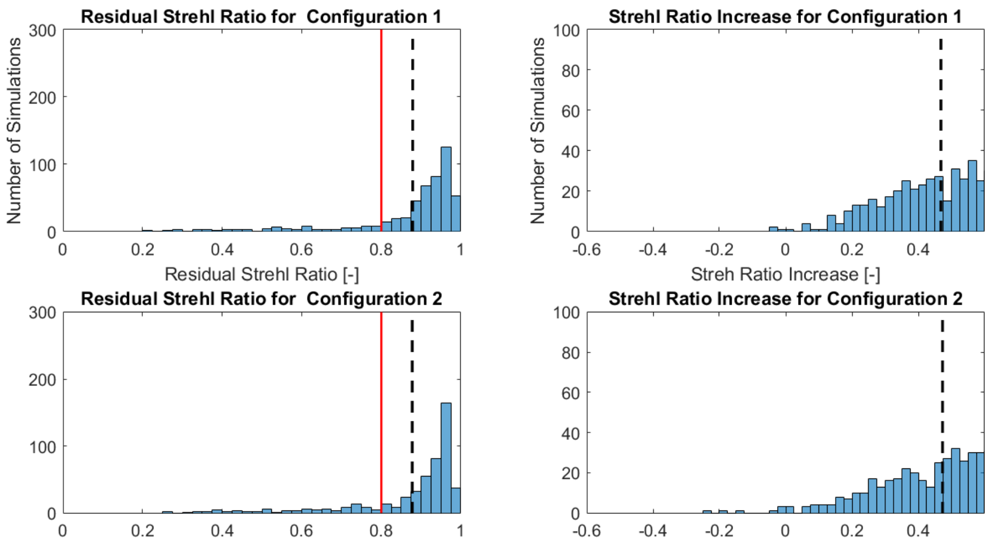

Figure 5.24: Histogram plots of the residual Strehl ratio and the Strehl ratio increase for the Open Loop performance analysis with 500 runs. The dashed black line indicates the average while the solid red line indicates the lower limit set by the requirements.

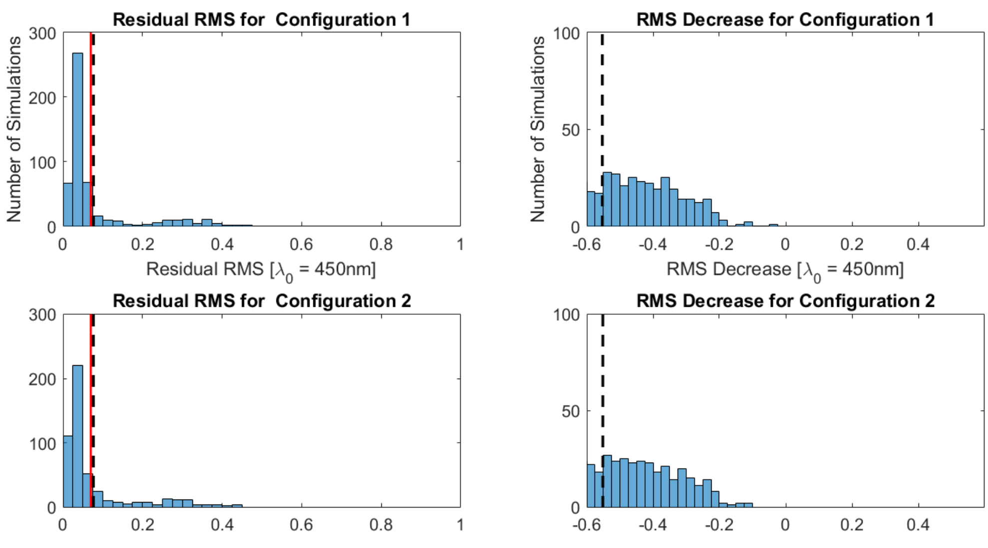

Figure 5.25: Histogram plots of the residual RMS error and the RMS decrease for the Open Loop performance analysis with 500 runs. The dashed black line indicates the average while the solid red line indicates the lower limit set by the requirements.

While it can be seen that the majority of cases resulted in an estimate well within the limits set by the requirements, in both the histogram representations of the residual Strehl ratios as well as in the histogram representations of the residual RMS errors a significant amount of runs with a low-quality result can be observed. To establish the reason for the poor performance of these estimations a large number of these results were inspected and compared to their corresponding simulated wavefront error. A typical example of such a case is presented in figure 5.26. As can be seen, the wavefront error estimate roughly resembles the actual wavefront error. However, at the top segment, a segment piston offset can be observed with respect to the actual wavefront shape. A similar estimation error, i.e. a segment piston offset on one or two segments, could also be observed in virtually all other estimates characterized by a low residual Strehl ratio and a high residual RMS error. It is hypothesized that the reason for these errors is the presence of local minima at locations of these inaccurate estimates.

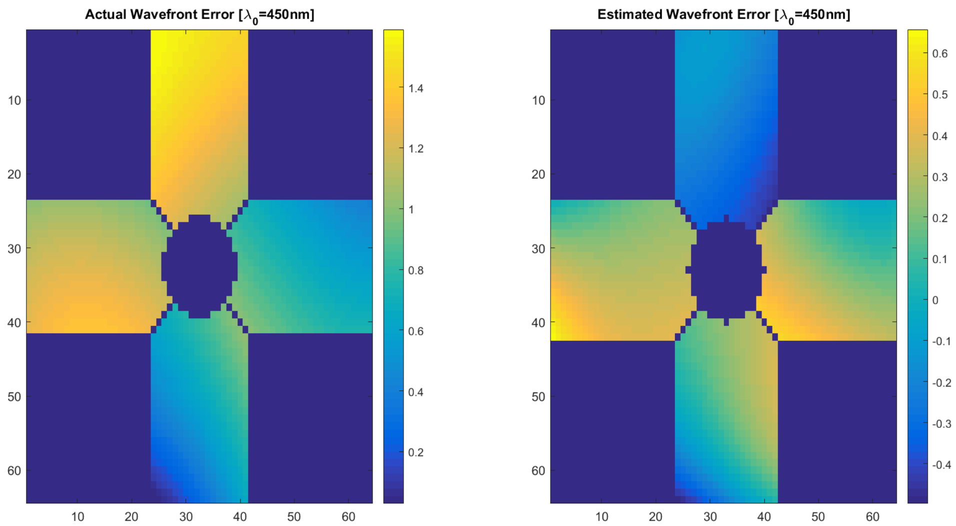

Figure 5.26: Example of a simulation resulting in a poor estimate (SR = 0.659 and RMS = 0.251).

To correct this, a mitigation strategy was proposed. The strategy is based on the observation that the current set of mechanical tolerance budgets generally leads to a simulated wavefront error with small differences in values between segments near the center, but with large differences in values between the segments near the outermost edges. The novel post-processing strategy employed uses the individual segment piston terms as well as the segment longitudinal tilt terms, around the axis parallel to the width dimension of each segment. A schematic representation of these basis functions is presented in figure 5.27. The post-processing method constructs a simplified wavefront error from the estimate, which is constructed solely from the segment piston and longitudinal tilt terms of the wavefront error. A line is drawn for each segment of this simplified wavefront error, running tangentially to the segment surface from the edge to the mid-point of the wavefront error. For each of the lines, the height of the point where the line crosses the center point is compared to the heights of the points where the other lines cross the center, resulting in a set of height differences $\{\Delta\}$. This is graphically represented in figure 5.28. If the height of the point of crossing of one or two segments differs significantly from the height of the point of crossing of the other segments, it is assumed that an erroneous segment piston term is estimated for this segment. If this is the case segment piston is added to these segments until the heights of all points of crossing are within a certain margin.

This corrected wavefront error is then used as the initial condition for a second PD algorithm execution. This post-processing algorithm was executed for all of the Monte Carlo analysis results to see if post-processing using a priori information about the expected wavefront error shape could indeed lead to improved performance. The results of the simulation are presented in figures 5.29 and 5.30.

As a result of the data post-processing, a slight increase in the average residual Strehl ratio could be observed for both configurations. The real improvement, however, can be observed when looking at the average residual RMS error, which is greatly reduced. This is mainly the result of the elimination of poor estimation, which can be seen when looking at the tails of the residual RMS error histograms. The size of the tails has been reduced significantly. In terms of percentages the fraction of configuration 1 and 2 estimation within

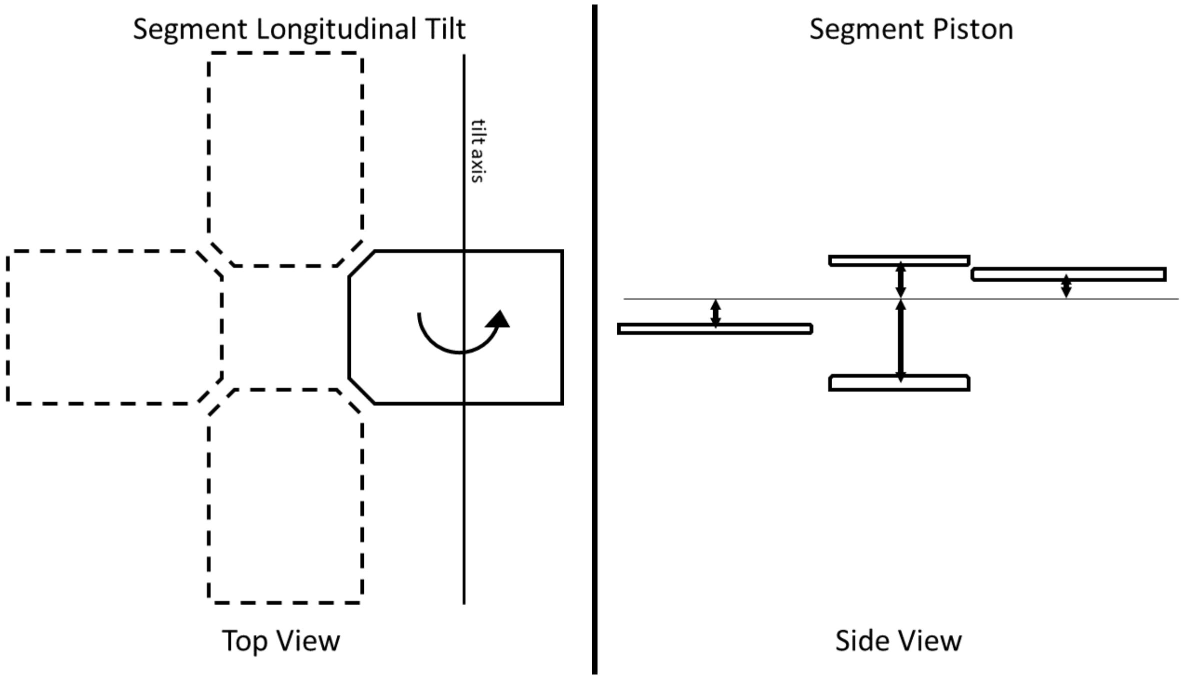

Figure 5.27: Relevant segment basis functions used by the post-processing algorithm.

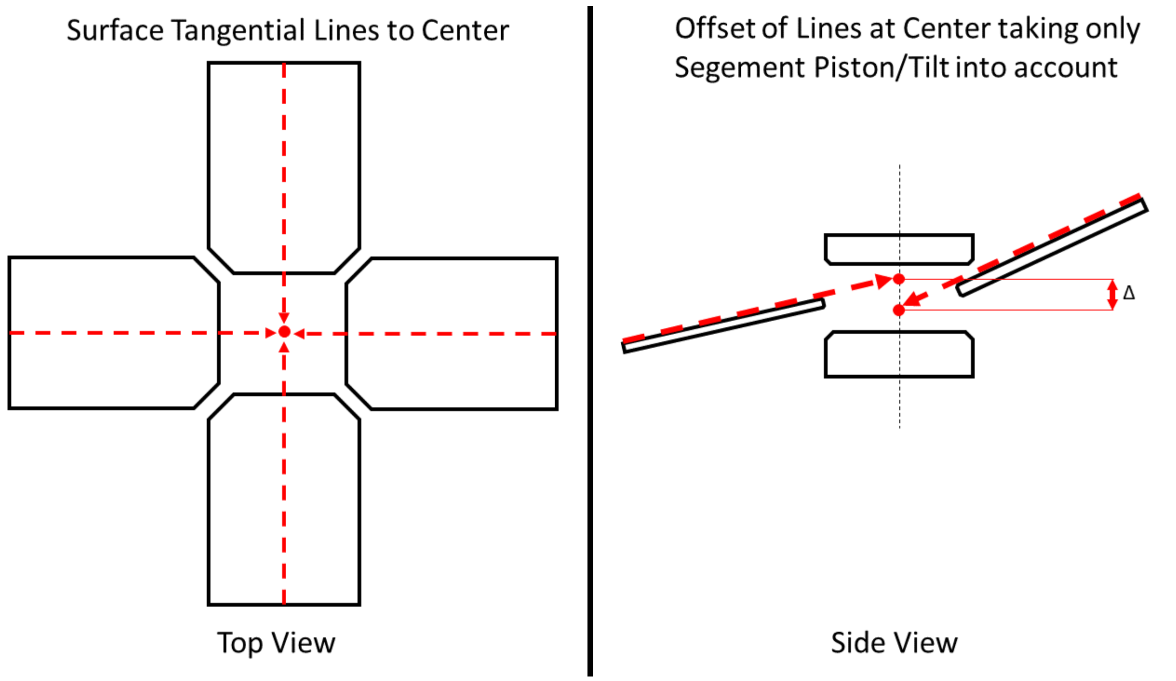

Figure 5.28: Visual description of the working principle of the post-processing algorithm.

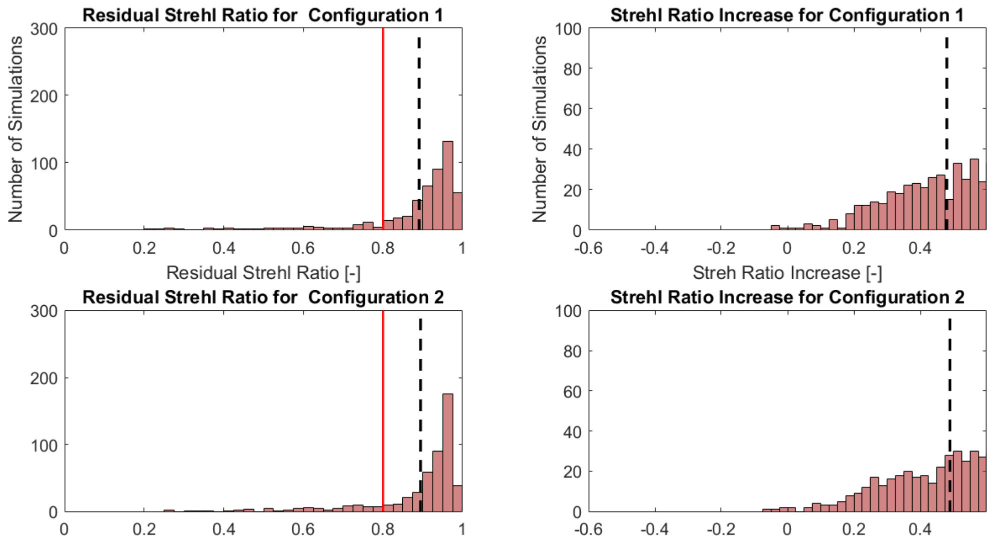

Figure 5.29: Histogram plots of the residual Strehl ratio and the Strehl ratio increase for the Open Loop performance analysis with 500 runs after correction. The dashed black line indicates the average while the solid red line indicates the lower limit set by the requirements.

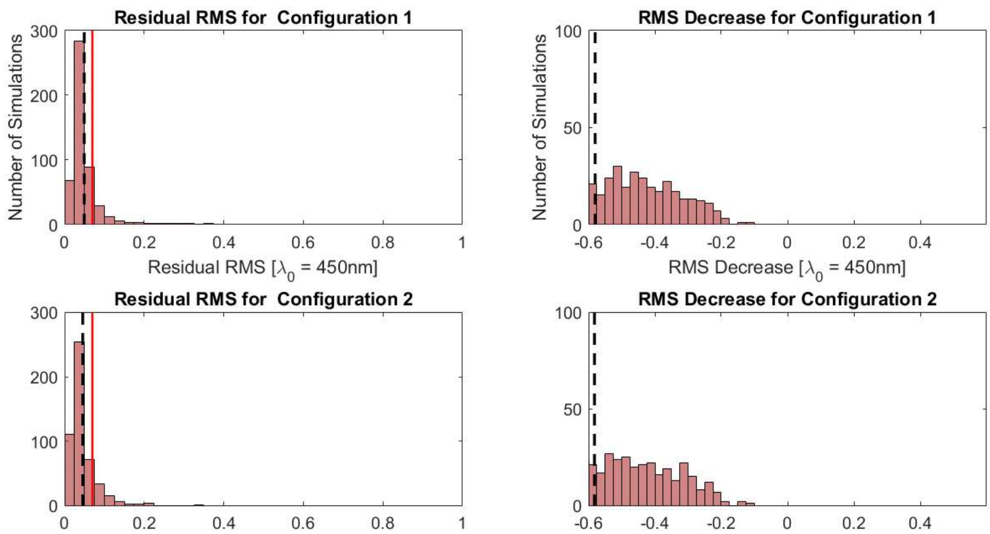

Figure 5.30: Histogram plots of the residual RMS error and the RMS decrease for the Open Loop performance analysis with 500 runs after correction. The dashed black line indicates the average while the solid red line indicates the lower limit set by the requirements.

the limits of the requirements is now 87.6% and 86% in terms of residual Strehl ratio and 86% and 85.6% in terms of residual RMS error. Inspection of the corrected estimates that previously showed a poor accuracy now indeed shows that segment piston estimation errors have been corrected in many cases. As an example the same wavefront error presented earlier in figure 5.26 is showed again in figure 5.31 for comparison. One curious thing to note here is that while the RMS decreased, the residual Strehl ratio of the estimation is slightly lower than for the uncorrected case. This happened only for a small number of simulations. In most cases, the Strehl ratio remained the same or increased, as can be observed from the average residual Strehl ratios provided in figure 5.29. The expected cause for the Strehl ratio decrease is that the value at the PSF peak is relatively insensitive to a segment piston error. Therefore, the slight decrease in Strehl ratio might be the result of incidentally poorer convergence behavior of the algorithm during the second optimization run. This could potentially result in a net decrease in the residual error terms.

Looking at the results it can be concluded that post-processing of the estimation using a priori knowledge about the expected wavefront error shape significantly improves performance. It should be noted, however, that if the mechanical tolerance budgets are changed at a later stage of the design the post-processing method has to be reassessed if it can still be applied in its current form. It could be possible that in the casing of different tolerance values a different shape property has to be exploited in post-processing or even that using a priori knowledge of the error shape will not result in any improvement at all.

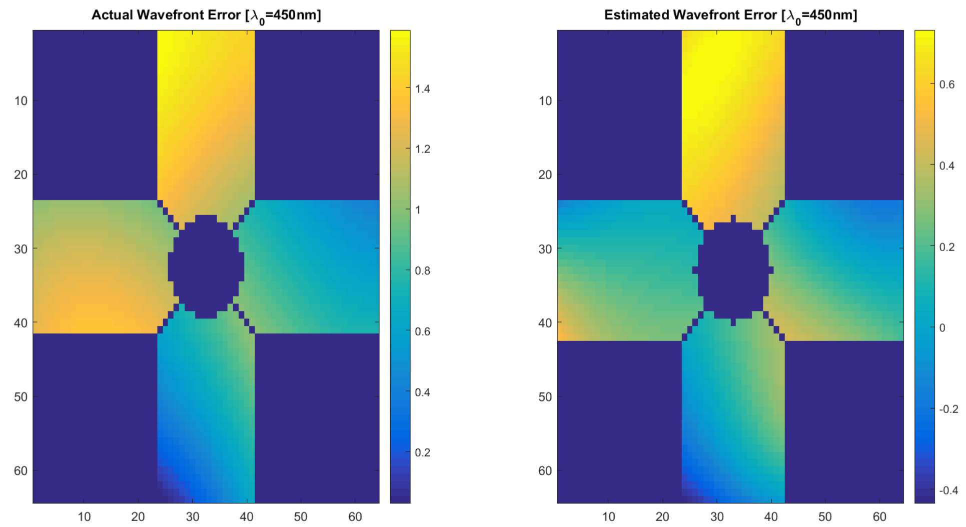

Figure 5.31: The new wavefront error estimate after the correction algorithm is run (SR = 0.595 and RMS = 0.108).

As a final assessment of the open-loop performance of the algorithm, a selection of the deconvolution results was analyzed. As described earlier in this report in section 3.2.5 deconvolution was performed using a Wiener deconvolution filter as well as an accelerated Richardson-Lucy algorithm. Because there is no robust method that can be used to quantitatively compare deconvolution results, a qualitative comparison was performed for four representative cases. These four cases, characterized by their original and residual Strehl ratios, are presented in figure 5.32. The top two rows show two cases with a similar original Strehl ratio while the bottom two rows show cases with a similar residual Strehl ratio. For each case, four images are presented: The original scene, the TDI-1 detector measurement, the result of deconvolution using a Wiener filter, and the result of deconvolution using the Accelerated Richardson-Lucy algorithm. The four cases are taken from the *Sea* scene type results because small details in the clouds are convenient for comparison. A few observations can be made:

1. The application of a deconvolution algorithm significantly increased the image quality in both cases
2. Wiener deconvolution significantly outperformed the Richardson-Lucy algorithm as can be observed from small gaps between clouds and the resolution of small details on the water
3. Gaps between clouds that could be resolved with the Richardson-Lucy are about one pixel, and smaller than one pixel for the Wiener algorithm. A single pixel corresponds to a distance of $25cm$

4. Both a higher original Strehl ratio as well as a higher residual Strehl ratio aid towards obtaining a better image quality through deconvolution

A final observation that can be made is the presence of some small artifacts after reconstruction through a Wiener filter. This is due to an intentional, slight underestimation of the Noise to Signal (NSR) ratio since it was found through trial and error that underestimation of the NSR to a reasonable extent allows for the preservation of small details.

These results show that phase diversity algorithms can significantly improve the resolution of the telescope, even if just passive reconstruction of the object through post-processing is applied.

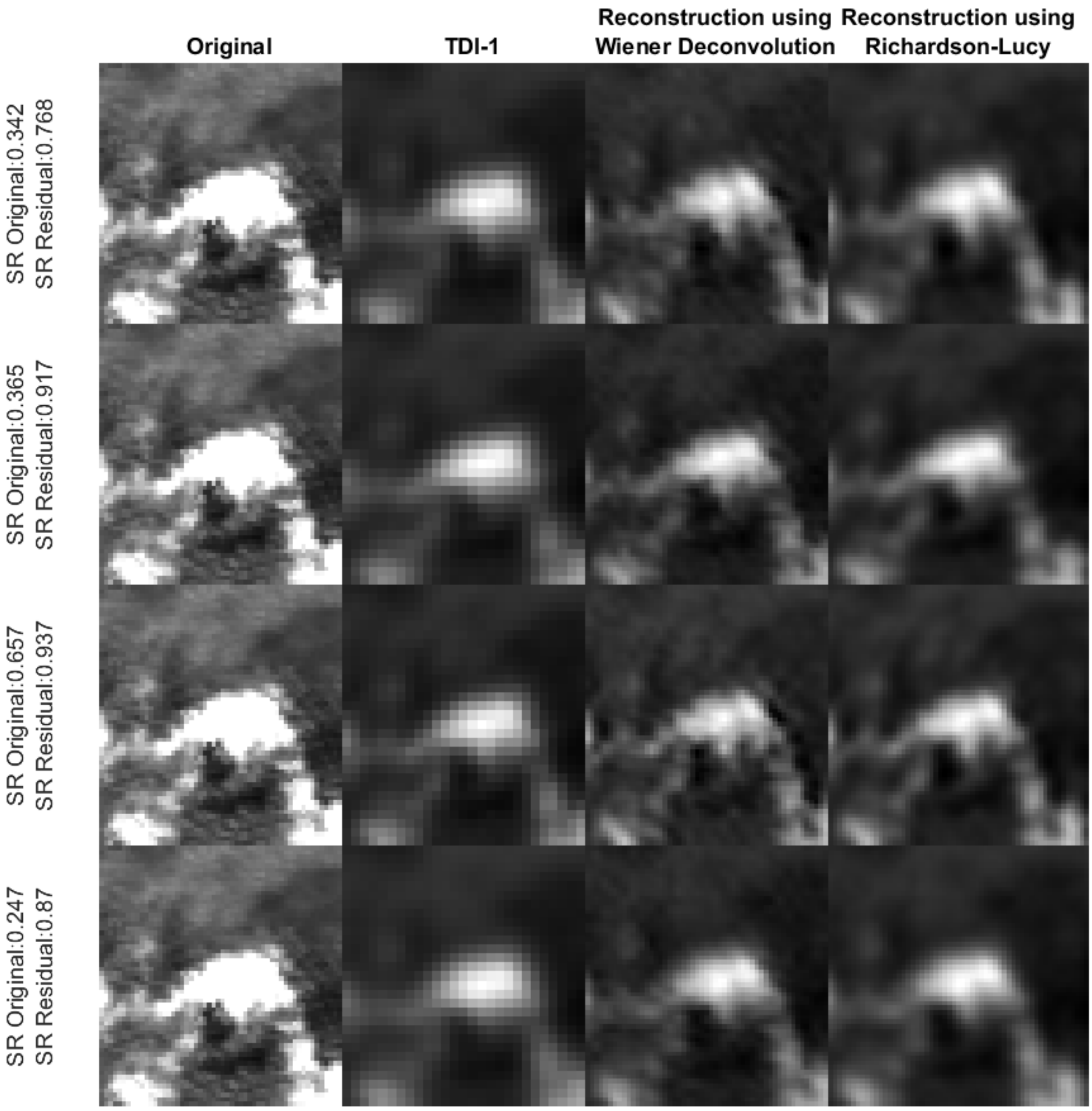

Figure 5.32: Comparison between the original scene, the TDI-1 measurement, the scene reconstructed using *deconvblind* with the estimated PSF as the kernal and lastly with the diffraction-limited PSF as the Kernel for four cases.

5.5. Closed-Loop Performance

The algorithm settings used for the closed-loop simulation has been adapted slightly from the open-loop algorithm settings by trial and error. These settings are presented in table 5.6. Two differences should be noted. The first is that in this simulation only the *Farm* scene type is used. The goal of these simulations is to provide an upper limit for the closed-loop configuration performance. Since only 100 simulations can be executed due to time constraints, it was decided to perform them all using the scene type that showed the best performance in the open-loop simulations. Using the same scene type allows convenient comparison of all 100 results per configuration. The second change in settings is that only one field is simulated instead of three fields. This is due to the fact that this decreases the time taken up by the imaging simulation by nearly a factor three. This is desirable due to time constraints. To test the sensitivity to this parameter change, 50 open-loop simulation runs were performed. No post-processing was used. This was done for a configuration that simulated three fields as well as a configuration that simulated a single field. Regardless of the fact that every of these 100 simulations was performed with a different wavefront error, the average original and residual Strehl ratios were still very similar as shown in table 5.7. It was therefore concluded that the simulations are insensitive to a reduction of the number of simulated fields from three to one. The results are tabulated in appendix section C.5.

Table 5.6: Table of settings for the closed-loop peformance studies.

Parameter	**Value**	**Unit**
Scene type	*Farm*	-
Number of detectors	2	-
Pupil Sampling Distance FORTA	1.02	mm
Tolerance Type	[Drift, New Drift, Calibrated]	-
Number of Discrete Field Angles for PSF calculation	1	-
TDI 2 defocus	0.5	wavelengths
Phase Diversity Subframe Size	128	pixels
Detector Pixel Pitch	5	μm
Average photon count per pixel	10^4	-
Gaussian Noise SNR	100	-
Zernike Polynomials	15 (= 24 basis functions)	-
Apodization ratio	0	$\frac{pixels_{apodized}}{pixels_{unapodized}}$
Learning Rate κ	0.001	-
Max Number of Iterations	2000	-
Defocus Error	0	μm
Step Tolerance (Fraction of initial Metric Value)	$1 \cdot 10^{-7}$	-
Post-processing algorithm enabled	Yes	-

Table 5.7: Average original and residual Strehl ratios of 50 simulation runs for a configuration simulating 1 field and a configuration simluation 3 fields. Simulation runs are independent, i.e. different wavefront errors were calculated for each configuration.

No. of Fields	**Original Strehl Ratio**	**Residual Strehl Ratio**
1	0.53	0.82
3	0.58	0.85

The results of the Monte Carlo simulations for the three configurations are presented in figures 5.33, 5.34 and 5.35. Each of the figures shows the Strehl ratio and the RMS error of the system in its initial state, after seven iterations of the closed-loop method, and at the iteration where the system performance is maximum. Both the performance at a field angle of 0.0 degrees, the center field, as well as at 0.3 degrees, the extreme field, is provided. For completeness, additional histogram plots are presented of the Strehl ratio values before and after calibration for configuration 3. While the calibration will not be treated at length, these histograms, presented in figure 5.36, serve to give the reader a feeling for the performance increase that is expected to be obtained through calibration. After the calibration shown here, the drift budgets are added resulting in the Strehl ratio that can be observed on the left side of figure 5.35.

In addition to these histograms, a scatter plot of the original Strehl ratio vs the Strehl ratio at the iteration where performance is maximum, is provided for each of the configurations in figure 5.37.

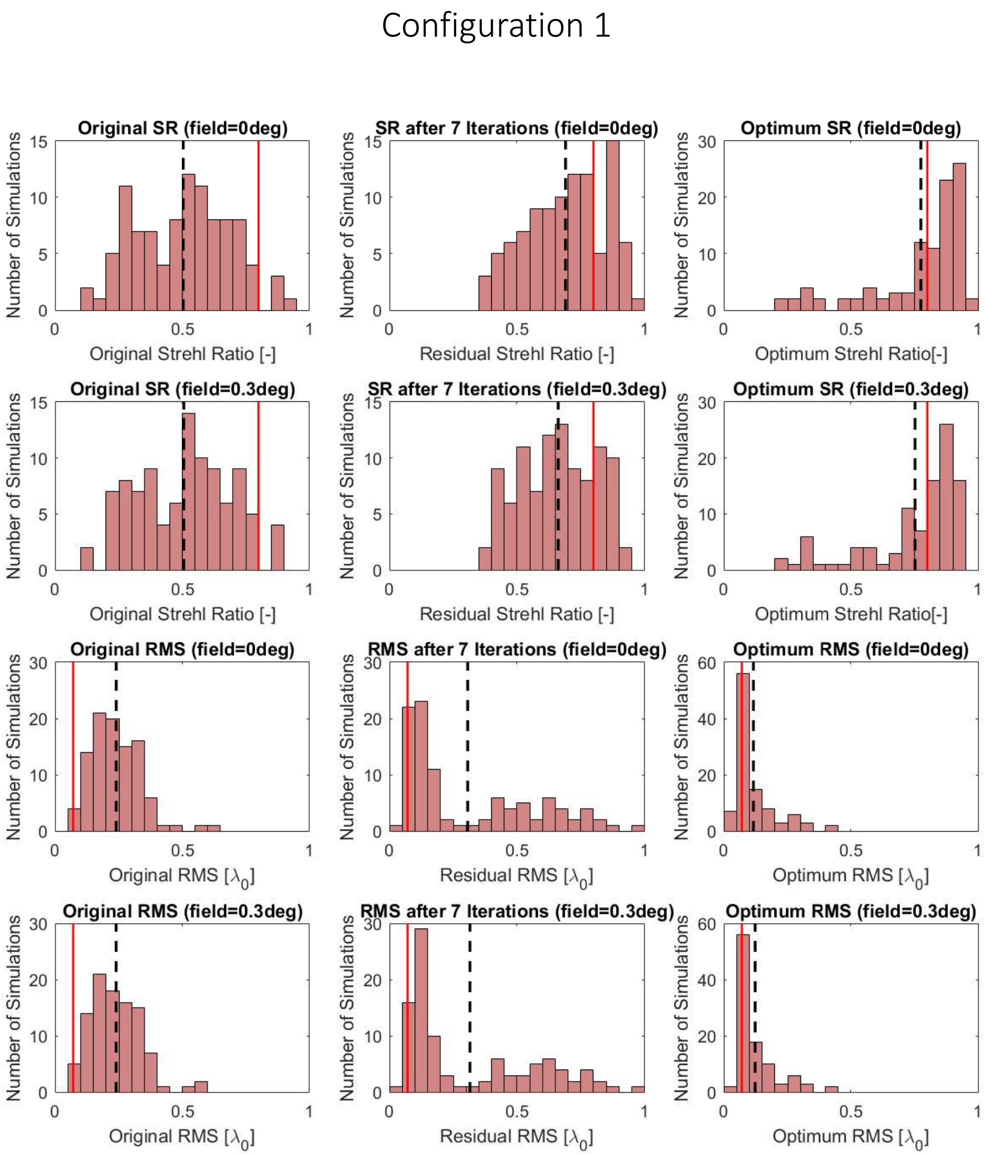

Figure 5.33: Resulting Strehl ratio and RMS error values from the Monte Carlo analysis of configuration 1. The solid red line indicates the limit set by the requirement, the dashed black line indicates the average of the results.

From figure 5.33 it can be observed that after seven iterations there is a significant improvement in both the Strehl ratio as well as the RMS error. However, it can also be observed that the average values of the RMS and Strehl ratio are still well below the minimum set by the requirements. Looking at the histograms to the right of the figure, it can be seen that if the Strehl ratio and RMS are plotted at the iteration where performance is maximum, the averages are very close to the limit set by requirements. In 62% of cases the center field Strehl ratio is above 0.8 and in 58% the extreme field Strehl ratio is above 0.8. For the RMS these percentages are lower, 37% and 26% respectively. While these percentages are low, it must be noted that the RMS value is $0.12\lambda_0$ on average, which is less than twice the allowable wavefront error RMS. In addition, the Strehl ratio has a stronger correlation with the image quality than the RMS error, as is explained in section 2.1.4.

From figure 5.37 it can be observed that the original Strehl ratio of the simulation has a strong impact on

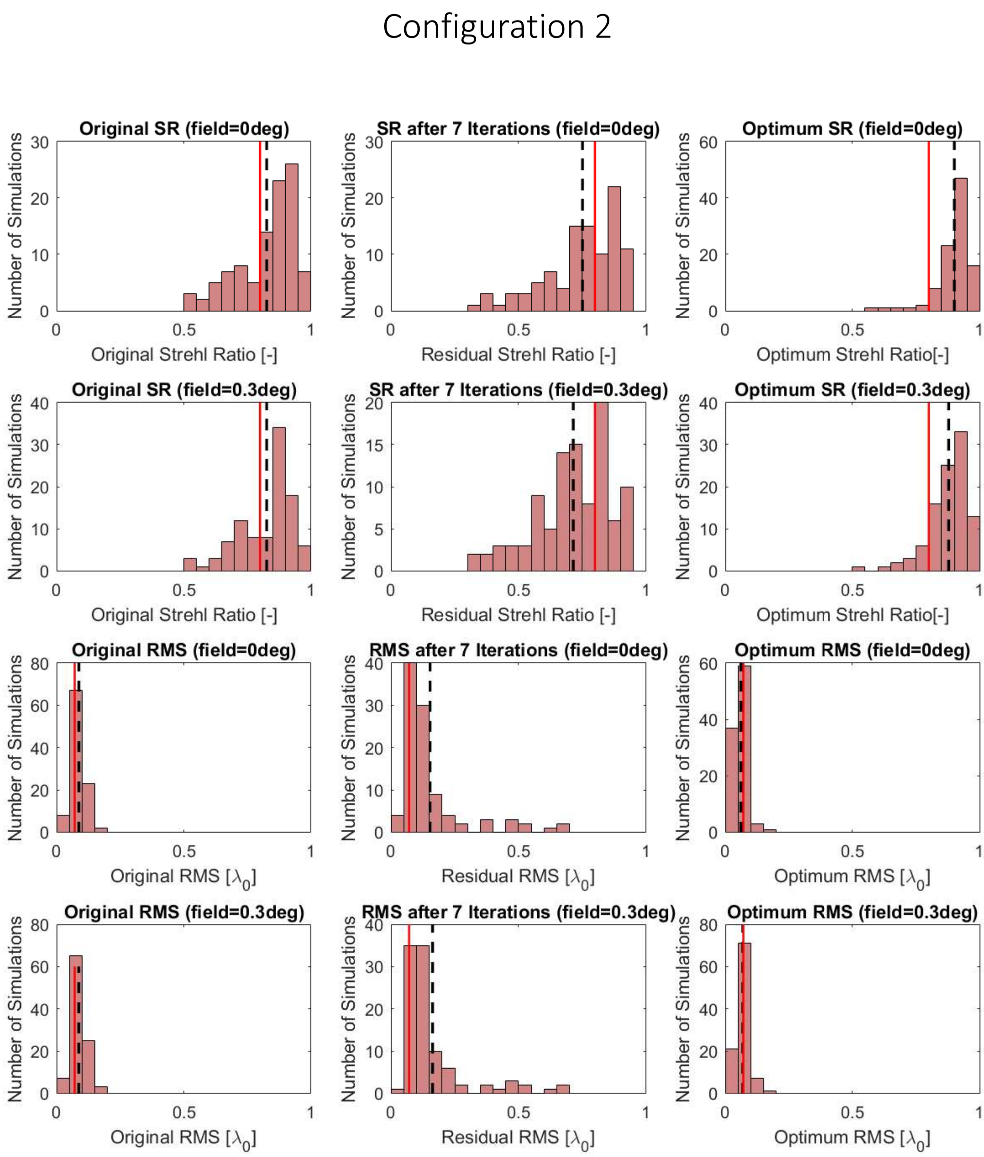

Figure 5.34: Resulting Strehl ratio and RMS error values from the Monte Carlo analysis of configuration 2. The solid red line indicates the limit set by the requirement, the dashed black line indicates the average of the results.

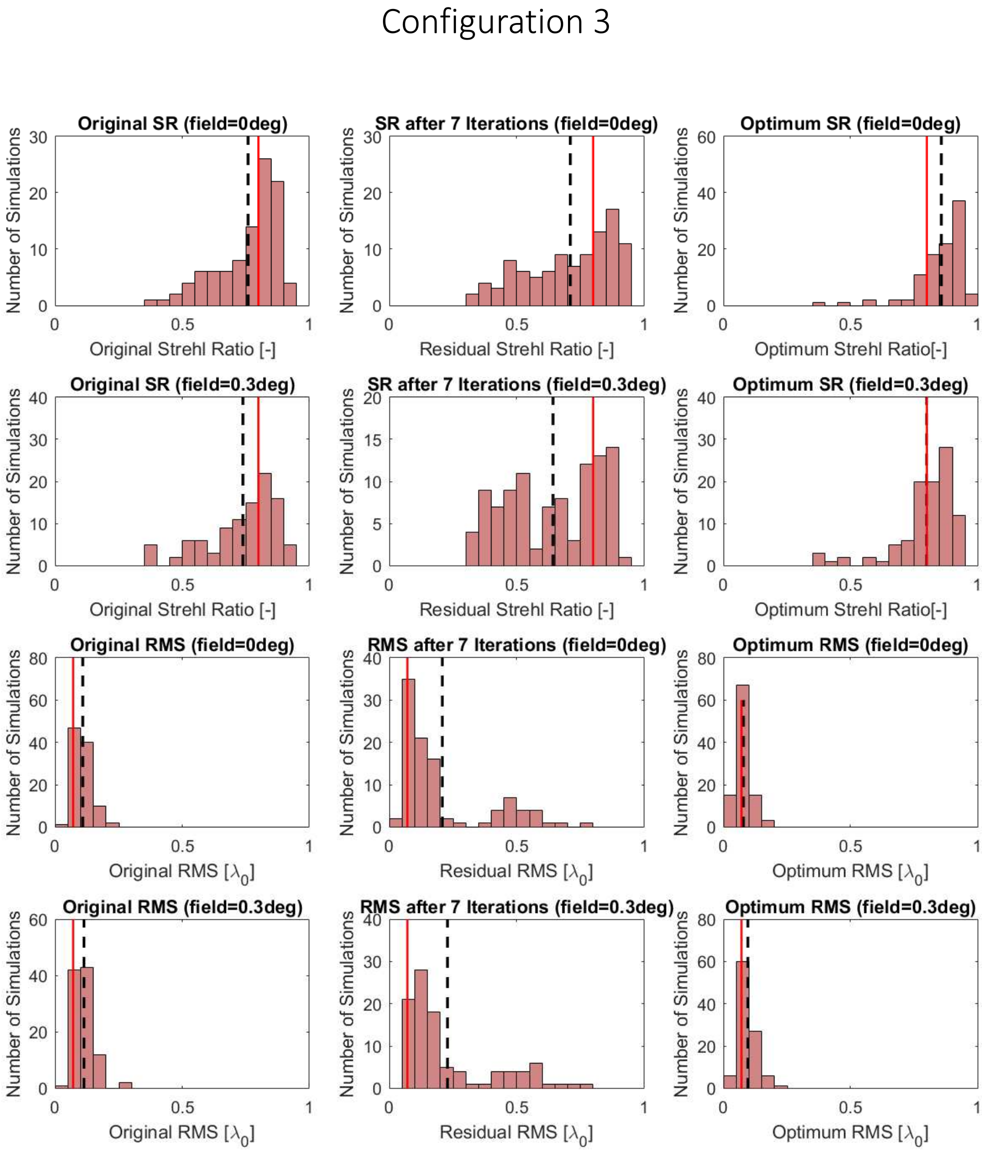

Figure 5.35: Resulting Strehl ratio and RMS error values from the Monte Carlo analysis of configuration 3. The solid red line indicates the limit set by the requirement, the dashed black line indicates the average of the results.

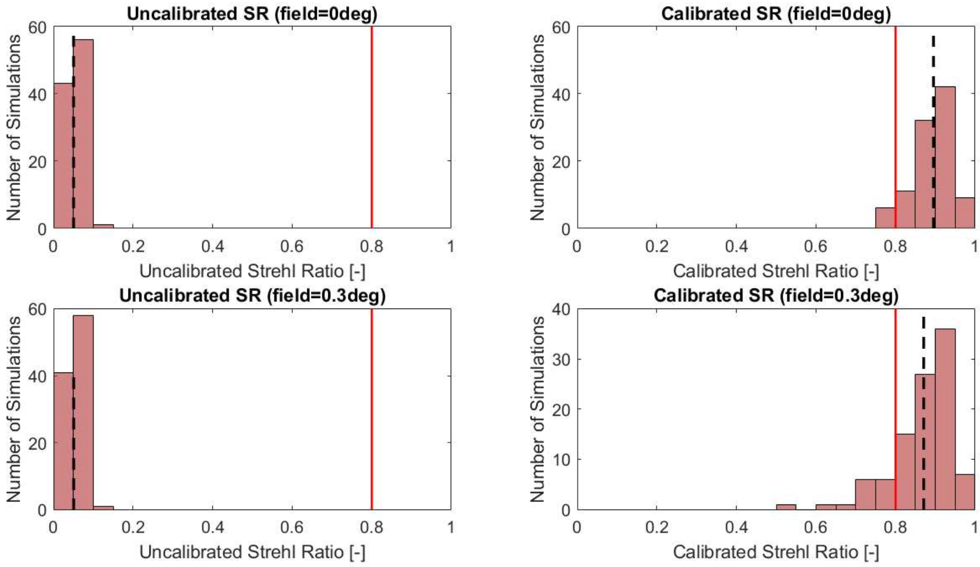

Figure 5.36: Strehl ratio for the 0 degree and 0.3 degree fields for configuration 3 before and after the application of the calibration trategy described in section 4.5.

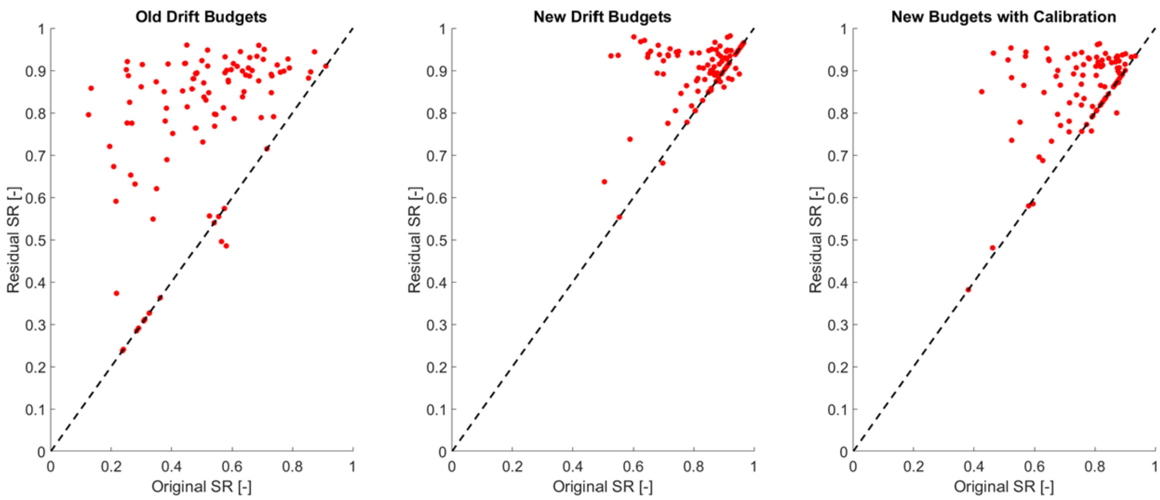

Figure 5.37: Scatter plots showing the original Strehl ratio vs the Strehl ratio at the iteration at which performance is maximum for the center fields of configurations 1, 2 and 3.

the accuracy of the estimate. Up until an original Strehl ratio of about 0.6, there is a large spread in the quality of the wavefront estimate. However, it can be seen that for simulations in which the original Strehl ratio was above 0.6, the residual Strehl ratio was almost always around 0.8 or higher. This is expected to be due to the fact that simulations with a lower original Strehl ratio are more likely to converge towards estimates that contain erroneous segment terms, as was discussed in section 5.4. It also interesting to see that the Strehl ratio and RMS error results obtained in the closed-loop simulation are less accurate than the results obtained in the open-loop simulation. However, this can be easily explained by the fact that in the assessment of the open-loop performance, virtual Strehl ratio and RMS values were used. These values were calculated by subtracting the estimated wavefront error from the actual wavefront error. This was done just to express the quality of the estimate. The Strehl ratio and RMS in the closed-loop simulations are the actual system parameters calculated after adaption of the active optics. The reduction in accuracy is due to the degradation caused by imperfect fitting of the estimation error by the active optics. When segment tip, tilt, and piston are corrected using the M1 segment controls, the control mechanism also causes parasitic movement in the plane perpendicular to the optical axis, introducing additional error terms. The DM is not able to adequately correct all of these aberrations, which introduces additional higher order aberrations into the system. These higher order aberrations decrease the optical performance and are also expected to cause the closed-loop phase diversity algorithm to diverge after a few iterations.

After the Monte Carlo analysis of configuration 1, which assumes the old *Drift* budgets, a Monte Carlo analysis of configuration 2, which assumes the new *Drift* budgets, was performed. As can be seen from figure 5.34, the new budgets significantly improved optical performance in general. The performance after seven iterations was, in terms of both Strehl ratio as well as RMS, worse than the initial performance of the system before the PD algorithm was executed. This poor performance is attributed to the fact that compared to configuration 1, the simulations reached an optimum at an earlier iteration on average, after which they started to diverge. After seven simulations the cumulative decrease in performance with respect to the initial performance was thus larger than for configuration 1. However, the SR and RMS values at the iteration were performance was maximum, showed significant improvement. The center field and extreme field Strehl ratios were above 0.8 in 94% and 87% of cases respectively. The center field and extreme field RMS errors were within the limits set by the requirements in 73% and 56% of cases. From figure 5.37 it can be seen that for the relatively lower original Strehl ratios, there was still a significant spread in results. However, in accordance with the results for configuration 1, resulting Strehl ratios were almost all around 0.8 or higher for simulations with an original Strehl ratio of 0.6 or higher.

Finally, a Monte Carlo analysis was done for configuration 3. The were expected to be different from the results of configuration 2 due to two reasons. First, the initial system performance was expected to be lower as the *Drift* budgets were added after a calibration step instead of to an ideal system. Second, due to the calibration step the active optics were already in adapted state, instead of in their default state, which was expected to lead to some higher order aberrations at the start of the first iteration. For these two reasons, performance was expected to be worse than for configuration 2. While figure 5.35 shows that performance was indeed worse, it was still much better than for configuration 1. Running the algorithm for seven iterations again resulted in a decrease in the performance. However, looking at the optimum performance a significant increase could indeed be seen. The Strehl ratios were compliant with requirements in 81% and 60% of cases for the center field and extreme field respectively. These percentages were 45% and 22% for the RMS error. Looking at the scatter plot in figure 5.37 a similar distribution can be witnessed as for configuration 2. Again, simulations in which the original Strehl ratio was above 0.6 typically showed an optimum performance of around or above 0.8. The slightly larger spread in the residual Strehl ratio resulting from simulations with a high original Strehl ratio is attributed to the presence of the higher aberrations resulting from parasitic movement of the segments during calibration.

It can be concluded from these Monte Carlo analyses that for a system with an initial Strehl ratio of larger than 0.6, a closed-loop configuration could deliver reliable performance. However, the number of iterations after which the method reached an optimum and started to diverge varied among simulations. No method has yet been developed to determine whether the algorithm has reached an optimum. Because of this, a closed-loop configuration is not reliable enough for implementation yet.

5.6. Chapter Summary

In this chapter, the results of the simulations were presented and discussed. Based on the parametric studies, two configurations were selected for further analysis. It was found, for both configurations, that calculating a grey world spectrum based on the multispectral channel measurement data did not noticeably improve the performance of the phase diversity algorithm when compared to the assumption of a uniform grey world spectrum. This means that the answer to secondary research question 1, presented in section 1.5.2, is: no, performance cannot be increased by including multispectral channel measurement data in the PSF estimation. Comparison of the different subframe selection algorithms, however, did find that performance of the algorithm could be increased in all nearly all cases using either the *Bright Peak* or the *Dark Borders* algorithm for selection of the subframe instead of applying phase diversity to a random subframe. The randomly selected subframe was, in this case, the central subframe. Since the *Bright Peak* algorithm performance was superior to the performance of the *Dark Borders* algorithm, it was adopted as the standard subframe selection method. The answer to secondary research question 2 is thus: yes, performance can be significantly increased by actively selecting the subframe to which phase diversity is applied. This finding is expected to apply to EO phase diversity methods in general and could be beneficial for the development of phase diversity algorithms for other EO instruments. The open-loop performance analysis found that both configuration 1, as well as configuration 2, would converge to a solution which meets the Strehl ratio requirement in over 80% of cases, and to a solution that meets the RMS requirement in over 75% of cases. Configuration 1, which used a subframe of only 128×128, showed both much shorter run times as well as slightly superior performance. Poor estimations were found to be characterized by an erroneous segment piston term of about a wavelength at one or two segments. Post-processing the data with an algorithm that exploited a priori knowledge of the expected error shape resulted in increased performance. After post-processing, over 85% of cases converged to a solution that met the Strehl ratio requirement and over 85% of cases converged to a solution that met the RMS error requirement. In most cases, the segment piston errors were removed. This novel approach shows promise and further development might result in additional improvement. Finally, it was found that Richardson-Lucy deconvolution resulted in a reconstruction with details as small as $25cm$. Wiener deconvolution, which uses the estimate of the wavefront error, outperformed Richardson-Lucy deconvolution and resulted in a reconstruction that showed details of even smaller than $25cm$.

With regard to the closed-loop performance of the system, it was found that a closed-loop PD method could potentially be effective for active correction of systems with an original Strehl ratio of higher than 0.6. However, two issues that limit the open-loop performance were encountered. The first is the fitting error due to parasitic movement resulting from control of the M1 segments for segment piston, tip, and tilt correction. This parasitic movement likely resulted in higher order aberrations in the system which are the expected cause of the lower performance of the closed-loop method compared to the virtual Strehl ratio and RMS values found in the open-loop performance analysis. In addition, these higher order aberrations are expected to be the cause of the divergence of the algorithm after it reaches an optimum after a several iterations. The number of iterations before an optimum was reached and divergence started differed among simulations. No reliable method has yet been found for determining when the algorithm has reached an optimum.

The final chapter of this report will present the conclusions that were drawn from these results and will present the recommendations for future research that are made based on these conclusions.

6 Conclusions and Recommendations

The previous chapter presented the results of the simulations and discussed the performance of the phase diversity algorithms. This final chapter of the report will present conclusions based on these results and reflect on the thesis goal, the research questions and the mission requirements of the DST project. First, section 6.1 discusses the conclusions. Afterwards, section 6.2 will present the recommendations.

6.1. Conclusions

The goal of the thesis project was expressed earlier in this report as:

> *The goal of this thesis project is to determine whether the implementation of Phase Diversity algorithms is a suitable strategy for aberration correction for the Deployable Space Telescope*

A corresponding primary research question was proposed, which focuses on the engineering dimension of this project. In addition, two secondary research questions were stated, related to two topics of scientific interest. First, the conclusions with respect to the primary research question will be discussed. Afterwards, the conclusions with respect to the secondary research questions will be presented

6.1.1. Conclusion Regarding Performance

The primary research question of the project was expressed as found in section 1.5. The primary research question concerns the achievable performance of phase diversity in the context of the DST project. The question was subdivided into two subquestions. The first concerns the performance of an open-loop phase diversity configuration in which an estimate is generated and deconvolution is subsequently applied to improve resolution and recover details lost during the imaging process. The second subquestion concerns the performance of an open-loop phase diversity configuration in which the estimation of the wavefront error is used for control of the systems active optics in an iterative fashion.

With regard to the first subquestion, it was found that the average performance of open-loop configuration 1 in terms of residual Strehl ratio was 0.88 and the average performance in terms of RMS was 0.077, which could be increased through post-processing to 0.89 and 0.05 respectively. Using a Wiener deconvolution filter in combination with the PSF estimate produced using phase diversity, sub-pixel details could be reconstructed in all observed cases, even when the Strehl ratio was below 0.8. This corresponds to a resolution of $25cm$. Comparing this figure to DST mission requirement **REQ-1** it can be observed that according to the simulation results the system should be able to meet the main mission requirement, a ground resolution of $25cm$. Comparing the achieved residual Strehl ratio to the lower limit of 0.8 set by requirement **REQ-6**, it can be concluded that after post-processing over 85% of simulations converge to an estimate with a residual Strehl ratio of higher than 0.8%. Comparing the RMS error to the RMS error requirement of $0.07\lambda_0$ set by **REQ-9** also shows that estimations meet the requirement in over 85% of cases. While care must be taken that these values for the Strehl ratio and RMS are not the actual residual values for the optical system, since the open-loop configuration does not involve re-configuring the active optics, it does show the high estimation accuracy that can be achieved using phase diversity algorithms. Implementation of the novel post-processing algorithm resulted in significant improvement in the number of simulation converging to an accurate estimate. The author considers it likely that a further increase in the number of converging simulations can be achieved if more post-processing or pre-processing methods that exploit shape characteristics of the expected wavefront error are implemented. This is also addressed in the recommendations. From discussions with Dolkens it was determined that requirement **REQ-5** concerning the MTF is an outdated requirement that should be revised. Therefore, performance was not assessed in term of the MTF curve value at the Nyquist and half the Nyquist frequency.

The average run time of the algorithm was around 20 seconds. Since the wavefront error does not change much during this interval, it is expected that regular execution of the phase diversity algorithm can continuously keep the system at diffraction-limited performance [19]. Furthermore, scientific literature was found demonstrating that using an FPGA for image convolution, one of the most demanding operations performed by the phase diversity algorithm, a speed increase of nearly 4 times could be achieved. Using GPU's it has been shown that a speed of almost 70 times the speed of MATLAB convolution can be achieved [72]. Therefore the 20 seconds seen in this project can be considered a very conservative estimation.

However, it should be noted that the simulations assumed a perfectly calibrated system to which the *Drift* tolerance budgets were added. In reality, a state of perfect calibration will not be reached, which means that the initial Strehl ratio will be lower than in the simulations. This might mean that in practice the open-loop RMS residual Strehl ratio and residual RMS could be slightly lower than in these simulations. Even in the case that the residual Strehl ratio and RMS are not lower, the resolution achieved with Wiener deconvolution might still decrease. This is because Wiener deconvolution performance positively correlates with the initial Strehl ratio as well. This should be further investigated.

With respect to the closed-loop simulations, it was found that the method was able to consistently increase the Strehl ratio to around or even above 0.8 for simulations in which the original Strehl ratio was at least 0.6, even for simulations that included simulation of the calibration step. For simulations were the original Strehl ratio was lower, an increase in the Strehl ratio was seen but the residual Strehl ratio was often lower than 0.8. As was mentioned earlier, it can be concluded that a closed-loop method can only be reliably implemented if two issues are solved. The issue of higher order aberrations caused by parasitic movement of the M1 segment and the related issue of determining at what iteration the algorithm should be terminated for optimum performance. Due to time constraint developing such a method could not be done within the scope of this thesis. However, it is expected that a termination criterion could be developed based on exploiting shape characteristics of the estimated wavefront error in a similar fashion as the post-processing algorithm described in this report. In addition, it could be possible that using the edge sensors which are currently included in the design for development of a termination criterion could be a feasible solution. These edge sensors are located at the edges between the M1 segments. Another possibility would be to mitigate the root cause of the divergence behavior of the algorithm, which are the higher order aberrations originating from the parasitic movement of the segments. The impact of these aberrations could perhaps be reduced if additional higher order Zernike basis functions are used for wavefront estimation in the closed-loop configuration.

6.1.2. Scientific Conclusions

The two secondary research question for this thesis project were on the topic of including multispectral data in the wavefront estimation, and on the topic active selection of the subframe, respectively.

The simulations have provided clear answers to both these research questions. With respect to the first question, it was found that no performance improvement was achieved when the multispectral channel measurements were used for the estimation of the grey world spectrum. It is hypothesized that this is due to the fact that there is no strong correlation, or even no correlation at all, between the average pixel color spectrum and the grey world spectrum.

However, with respect to research the second question it was found that active selection of the subframe to which the phase diversity is applied makes a very significant difference. Especially the performance of the *Bright Peak* algorithm resulted in a large increase in performance. It is expected that increasing the intensity in the center of the frame relative to the intensity just outside of the frame decreases the negative influence of parts of the scene that fall outside of the subframe but still influence the measurement through their PSF signature. It is expected that selection of the subframe could not just improve performance in the context of the DST but also for other EO instruments that rely on phase diversity algorithms.

Two other innovations of scientific relevance, are the implementation of the smooth decomposition method developed by Mahmood et al., and the post-processing method developed in this project. The former was used to treat Fourier Domain artifacts resulting from the Fast Fourier Transform's implicit assumption of periodicity. In the literature on phase diversity, these artifacts are often mitigated through the application of apodization. Section 5.1.15 shows that the method developed by Mahmood proved superior to most apodization schemes applied, and showed comparable performance to the full apodization configuration. Undocumented test runs showed that the apodization ratio required for optimum performance differs strongly depending on the algorithm settings. While full apodization using an apodization ratio of 1.0 did show the best performance for the particular study presented in section 5.1.15, lower apodization ratios were more effective for other configuration methods. The smooth decomposition method, however, showed excellent performance regardless of algorithm settings. Because of this, it is considered to be more robust than apodization.

Phase diversity algorithms sometimes have the tendency to convert to local minima that do not correspond to the actual wavefront error shape. It proved very effective to exploit characteristics of the expected wavefront shape to identify erroneous points of convergence, and subsequently correct the wavefront shape. While the post-processing method implemented in this project already resulted in a significant improvement in performance, it is expected that further analysis of the error shapes using statistics could result in even more powerful post-processing algorithms. While shape characteristics are different in every optical system, the insights gained in this project might serve as a starting point for the development of post-processing algorithms for other systems as well.

6.2. Recommendations

While the conclusions presented in the previous section provide an answer to the research questions posed in this report. Based on these conclusions this report presents a number of recommendations for the DST project. These will be presented in this section. The list of recommendations contains both recommendations with respect to the design of the DST, as well as recommendations for further research topics.

If it is decided to implement phase diversity as either a stand-alone aberration correction method or as part of a hybrid correction strategy, the following design parameter settings are recommended:

- A two detector configuration. The field separation between these detectors is irrelevant for the performance of the PD algorithm.
- For addition of the known defocus aberration to the TDI-2 measurement, a $0.5mm$ displacement of TDI-2 is advised. Whether the defocus displacement is in the direction of the exit pupil or away from the exit pupil is not relevant for performance.
- The accuracy of the TDI-2 defocus displacement should be maximum $5\mu m$. If this is found to result in a high price for the detectors, studies should be performed to see if this number can be further relaxed.
- A requirement for the max chance of a pixel going dead during operation should be added to the list of subsystem requirements. Suggested values are 0.5% (goal) and 1% (threshold).

In addition, it is recommended that further research is done on several topics. It is advised that additional simulations are performed that combine calibration with phase diversity. This is especially true for the case of the open-loop configuration, for which no simulations including calibration have been performed yet. However, also for the closed-loop configuration only a single Monte Carlo analysis including calibration has been performed. It would be interesting if a broader range of configurations, including different algorithm settings as well as different calibration methods were simulated. A configuration that would be interesting to simulate is a joint implementation with the Parallel Perturbation Stochastic Gradient Optimization algorithm developed by van Marrewijk. One possible configuration for aberration correction would be the use of van Marrewijk's SGD method, supported by phase diversity for checking whether the SGD algorithm converged to the correct point. Another would be the combination of using SGD until a Strehl ratio of about 0.6 is reached after which a closed-loop phase diversity algorithm is executed for further improvement of the system performance. One challenge which has to be solved for such a calibration, however, is determining when a Strehl ratio of 0.6 is reached.

Further possibilities for post-processing should be researched to prevent the erroneous piston error estimations that occur in about 15% of the open-loop simulations after the current post-processing algorithm has been used for correction. An interesting opportunity would be to not just exploit obvious shape characteristics of the expected wavefront error, but also employ machine learning to discover exploitable patterns in the occurring wavefront errors. In addition, it could be studied if the edge sensor measurements can be used to validate the wavefront error estimation produced using phase diversity. It should then also be investigated whether the application of these two methods can be extended to the case of closed-loop phase diversity methods for development of a termination criterion. Such a criterion would make a closed-loop phase diversity method a good candidate for active aberration control. If further research is done on the implementation of phase diversity in the DST, the author would suggest that either the use of machine learning or use of the edge sensors is selected as the main topic.

An additional improvement would be to research the topic of image power spectrum estimation. If a better estimate of the image power spectrum could be produced, this could be used to produce a frequency dependent SNR estimate. This SNR estimate could, in turn, be used for calculation of a Wiener filter that suppresses noise more selectively and preserves high frequencies that carry significant amounts of signal. This could further increase the resolution that is obtained through deconvolution.

Furthermore, it is advised to re-run some of the simulations when more is known about the choice of the detectors, as well as the environmental parameters, such as the expected average photon count per pixel or the noise types and magnitudes. This could either confirm the rationale for the design changes proposed above or lead to new insights regarding the optimum phase diversity algorithm design.

Lastly, it is advised that an experimental breadboard setup is created in the future so that the results obtained in this study through simulation can be validated using empirical data.

Appendices

A

Pixel PSF Derivation

To prove that the value of each individual detector pixel can be determined by convolving the ideal geometric projection of the object $o(u)$ with the Pixel PSF, it is convenient to start with the most general expression for the measured intensity at a single square pixel in the image plane with center coordinates u_c as shown in equation (A.1). Note that u is a 2-dimensional position vector that denotes the position in the image plane. Δu is the 2-dimensional vector indicating the side lengths of the square pixel.

$$p(u_c, \Delta u) = \iint_{u_c - \frac{\Delta u}{2}}^{u_c + \frac{\Delta u}{2}} \iint_{-\infty}^{\infty} o(u') s(u - u') \mathrm{d}u' \mathrm{d}u \tag{A.1}$$

For a space invariant PSF this equation can be rewritten to the expression presented in equation (A.2).

$$p(u_c, \Delta u) = \iint_{-\infty}^{\infty} o(u') \iint_{u_c - \frac{\Delta u}{2}}^{u_c + \frac{\Delta u}{2}} s(u - u') \mathrm{d}u \mathrm{d}u' \tag{A.2}$$

The limits of the inner integral complicate the further analysis of the relation and can be removed by defining a 2-dimensional square pulse signal, shown in equation (A.3).

$$\Pi(\Delta u, u) = \begin{cases} 1 & \text{if } -\frac{\Delta u}{2} < u < \frac{\Delta u}{2} \\ 0 & \text{otherwise} \end{cases} \tag{A.3}$$

Using this square pulse equation (A.2) can be rewritten to the expression shown in equation (A.4).

$$p(u_c, \Delta u) = \iint_{-\infty}^{\infty} o(u') \iint_{-\infty}^{\infty} \Pi(\Delta u, u - u_c) s(u - u') \mathrm{d}u \mathrm{d}u' \tag{A.4}$$

Introducing a change of variable from u' to $u' + u_c$ the expression in equation (A.5) is derived.

$$p(u_c, \Delta u) = \iint_{-\infty}^{\infty} o(u' + u_c) \iint_{-\infty}^{\infty} \Pi(\Delta u, u - u_c) s(u - u' - u_c) \mathrm{d}u \mathrm{d}u' \tag{A.5}$$

Due to the fact that the integral runs from $-\infty$ to ∞, the constant u_c term can be dropped for the innermost terms without consequence, resulting in equation (A.6).

$$p(u_c, \Delta u) = \iint_{-\infty}^{\infty} o(u' + u_c) \iint_{-\infty}^{\infty} \Pi(\Delta u, u) s(u - u') \mathrm{d}u \mathrm{d}u' \tag{A.6}$$

The innermost term can now be recognized as a convolution between a square pulse with the dimensions of the pixel and the PSF of the optical channel. This expression can be exploited if a pixel PSF is now defined as s_{pix} as shown in equation (A.7).

$$s_{pix}(\Delta u, u') = \iint_{-\infty}^{\infty} \Pi(\Delta u, u) s(u' - u) \mathrm{d}u \tag{A.7}$$

Due to the symmetric nature of the square pulse Π equation (A.6) can be rewritten to the expression shown in equation (A.8) if the pixel PSF s_{pix} is substituted in.

$$p(u_c, \Delta u) = \iint_{-\infty}^{\infty} o(u' + u_c) s_{pix}(\Delta u, -u') \mathrm{d}u' \tag{A.8}$$

The direction in which the variable $\mathrm{d}u'$ runs when calculating this integral is inconsequential, which means that this equation can be rewritten to the expression shown in equation (A.9).

$$p(u_c, \Delta u) = \iint_{-\infty}^{\infty} o(u_c - u') s_{pix}(\Delta u, u') \mathrm{d}u' \tag{A.9}$$

This expression can be recognized as a simple convolution between the projection of the object predicted by ideal geometric optics and the pixel PSF s_{pix}, shown in equation (A.10).

$$p(u_c, \Delta u) = (o * s_{pix}(\Delta u))(u_c) \tag{A.10}$$

The value at each pixel in the complete set of pixels $\{p\}$ can therefore be calculated by convolving $o(u)$ with the pixel PSF s_{pix} and then sampling at the location of the pixel centers $\{u_c\}$.

B
Analytic Gradient for Broadband Metric

This appendix provides the derivation of the analytic gradient of the broadband phase diversity metric described by Seldin [50]. To calculate this gradient one should start from the expression for a single Coherent Transfer Function calculated at a sample wavelength index l. This expression is shown in equation (B.1).

$$H_{kl}(f) = |H(f)| \exp\left[i\frac{\bar{\lambda}}{\lambda}(\phi(f,\alpha) + \theta_k(f))\right] \tag{B.1}$$

Note that throughout this derivation f will be used as the 2-dimensional vector containing the spatial frequency coordinates and u will be used as the 2-dimensional vector containing the image plane coordinates. In this equation, the parameter $\bar{\lambda}$ is the base wavelength in terms of which the Optical Path Difference is expressed. The monochromatic Coherent PSF $h_{kl}(u)$ can be calculated from this CTF by appropriately adding or removing zeros and subsequently applying the inverse Fourier transform, as shown in equation (B.2).

$$h_{kl}(u) = \sum_{f=0}^{N_{kl}-1} H_{kl}(f) \exp\left[i\frac{2\pi}{N_{kl}}\langle f, u\rangle\right] \tag{B.2}$$

The method that is used to derive the analytic gradient is analogous to the method used by Paxman et al. [48] to compute the analytic gradient of the metric proposed by Gonsalves [43], which relies on the fact that the Optical transfer function of the Optical Transfer Function $S_k(f)$ can be written as the autocorrelation of the CTF $H_k(f)$. However, performing this calculation at all sample wavelengths would result in a different sampling interval for every monochromatic OTF $S_{kl}(f)$ which makes the calculation of the analytic gradient impossible. It is, therefore, worthwhile to see if an analogous autocorrelation expression could be found that results in a common grid size for all OTFs, containing the arbitrary function $\mathbf{H}_{kl}(f)$. Such an expression is shown in equation (B.3).

$$S_{lk}(f) = \frac{1}{N^2}\sum_{f=1}^{N-1} \mathbf{H}_{kl}(f')\mathbf{H}^*_{kl}(f'-f) \tag{B.3}$$

It has been found by the author that such an expression exists when $\mathbf{H}_{kl}(f)$ is defined as shown in equation (B.4) and (B.5).

$$\mathbf{H}_{kl}(f') = \sum_{u'=-\frac{N}{2}}^{\frac{N}{2}-1} \frac{1}{N_{kl}^2} \sum_{f=0}^{N_{kl}-1} H_{kl}(f) \exp\left[i\frac{2\pi}{N_{kl}}\langle f, u'\rangle\right] \exp\left[-i\frac{2\pi}{N}\langle u', f'\rangle\right] \tag{B.4}$$

$$\mathbf{H}_{kl}(f'-f'') = \sum_{u'=-\frac{N}{2}}^{\frac{N}{2}-1} \frac{1}{N_{kl}^2} \sum_{f=0}^{N_{kl}-1} H_{kl}(f) \exp\left[i\frac{2\pi}{N_{kl}}\langle f, u'\rangle\right] \exp\left[-i\frac{2\pi}{N}\langle u', f'\rangle\right] \exp\left[i\frac{2\pi}{N}\langle u', f''\rangle\right] \tag{B.5}$$

The partial derivative of each monochromatic OTF $S_{kl}(f)$ with respect to an arbitrary basis function coefficient α_j can then be expressed as shown in equation (B.6).

$$\frac{\partial}{\partial \alpha_j} S_{kl}(f) = \frac{1}{N^2} \sum_{f'=0}^{N-1} \left[\mathbf{H}_{kl}^*(f'-f'') \frac{\partial}{\partial \alpha_j} \mathbf{H}_{kl}(f) + \mathbf{H}_{kl}(f') \frac{\partial}{\partial \alpha_j} \mathbf{H}_{kl}^*(f'-f'') \right] \tag{B.6}$$

Expanding this by substituting (B.4) and (B.5) into this expression then results in equation (B.7).

$$\begin{aligned}
\frac{\partial}{\partial \alpha_j} S_{kl}(f) = \frac{1}{N^2} \sum_{f'=0}^{N-1} \Bigg[& \sum_{u'=-\frac{N}{2}}^{\frac{N}{2}-1} \frac{1}{N_{kl}^2} \sum_{f=0}^{N_{kl}-1} H_{kl}^*(f) \exp\left[i \frac{2\pi}{N_{kl}} \langle f, u' \rangle\right] \exp\left[-i \frac{2\pi}{N} \langle u', f' \rangle\right] \exp\left[i \frac{2\pi}{N} \langle u', f'' \rangle\right] \\
& \times \sum_{u'=-\frac{N}{2}}^{\frac{N}{2}-1} \frac{1}{N_{kl}^2} \sum_{f=0}^{N_{kl}-1} i \frac{\bar{\lambda}}{\lambda_l} \phi_n(f) H_{kl}(f) \exp\left[i \frac{2\pi}{N_{kl}} \langle f, u' \rangle\right] \exp\left[-i \frac{2\pi}{N} \langle u', f' \rangle\right] \\
& - \sum_{u'=-\frac{N}{2}}^{\frac{N}{2}-1} \frac{1}{N_{kl}^2} \sum_{f=0}^{N_{kl}-1} H_{kl}(f) \exp\left[i \frac{2\pi}{N_{kl}} \langle f, u' \rangle\right] \exp\left[-i \frac{2\pi}{N} \langle u', f' \rangle\right] \\
& \times \sum_{u'=-\frac{N}{2}}^{\frac{N}{2}-1} \frac{1}{N_{kl}^2} \sum_{f=0}^{N_{kl}-1} i \frac{\bar{\lambda}}{\lambda_l} Z_j(f) H_{kl}^*(f) \exp\left[i \frac{2\pi}{N_{kl}} \langle f, u' \rangle\right] \exp\left[-i \frac{2\pi}{N} \langle u', f' \rangle\right] \exp\left[i \frac{2\pi}{N} \langle u', f'' \rangle\right] \Bigg]
\end{aligned} \tag{B.7}$$

Defining the variable $f''' = f' - f''$ and taking the summation $\sum_{f'=0}^{N-1}$ into the brackets, this expression can be rewritten to equation (B.8).

$$\begin{aligned}
\frac{\partial}{\partial \alpha_j} S_{kl}(f) = \frac{1}{N^2} \Bigg[& \sum_{f'=0}^{N-1} \sum_{u'=-\frac{N}{2}}^{\frac{N}{2}-1} \frac{1}{N_{kl}^2} \sum_{f=0}^{N_{kl}-1} H_{kl}^*(f) \exp\left[i \frac{2\pi}{N_{kl}} \langle f, u' \rangle\right] \exp\left[-i \frac{2\pi}{N} \langle u', f' \rangle\right] \exp\left[i \frac{2\pi}{N} \langle u', f'' \rangle\right] \\
& \times \sum_{u'=-\frac{N}{2}}^{\frac{N}{2}-1} \frac{1}{N_{kl}^2} \sum_{f=0}^{N_{kl}-1} i \frac{\bar{\lambda}}{\lambda_l} Z_j(f) H_{kl}(f) \exp\left[i \frac{2\pi}{N_{kl}} \langle f, u' \rangle\right] \exp\left[-i \frac{2\pi}{N} \langle u', f' \rangle\right] \\
& - \sum_{f'''=0}^{N-1} \sum_{u'=-\frac{N}{2}}^{\frac{N}{2}-1} \frac{1}{N_{kl}^2} \sum_{f=0}^{N_{kl}-1} H_{kl}(f) \exp\left[i \frac{2\pi}{N_{kl}} \langle f, u' \rangle\right] \exp\left[-i \frac{2\pi}{N} \langle u', f''' \rangle\right] \exp\left[-i \frac{2\pi}{N} \langle u', f'' \rangle\right] \\
& \times \sum_{u'=-\frac{N}{2}}^{\frac{N}{2}-1} \frac{1}{N_{kl}^2} \sum_{f=0}^{N_{kl}-1} i \frac{\bar{\lambda}}{\lambda_l} Z_j(f) H_{kl}^*(f) \exp\left[i \frac{2\pi}{N_{kl}} \langle f, u' \rangle\right] \exp\left[-i \frac{2\pi}{N} \langle u', f''' \rangle\right] \Bigg]
\end{aligned} \tag{B.8}$$

Applying the convolution theory twice to the second terms of both the first as well as the second multiplication, the $Z_j(f)$ and $H_{kl}(f)$ terms can be separated and the former can be moved out of the brackets, resulting in equation (B.9). It should be noted that in this expression the term f''' has been discarded and replaced by f'' for readability.

$$
\begin{aligned}
\frac{\partial}{\partial\alpha_j}S_{kl}(f) = \frac{i}{N^2}\frac{\bar{\lambda}}{\lambda_l}\sum_{f'=0}^{N-1}\sum_{u'=-\frac{N}{2}}^{\frac{N}{2}-1}\frac{1}{N_{kl}^2}\sum_{f=0}^{N_{kl}-1} Z_j(f)\exp\left[i\frac{2\pi}{N_{kl}}\langle f,u'\rangle\right]\exp\left[-i\frac{2\pi}{N}\langle u',f'\rangle\right] \\
\times\left[\sum_{u'=-\frac{N}{2}}^{\frac{N}{2}-1}\frac{1}{N_{kl}^2}\sum_{f=0}^{N_{kl}-1} H_{kl}(f)\exp\left[i\frac{2\pi}{N_{kl}}\langle f,u'\rangle\right]\exp\left[-i\frac{2\pi}{N}\langle u',f'\rangle\right]\right. \\
\times\sum_{u'=-\frac{N}{2}}^{\frac{N}{2}-1}\frac{1}{N_{kl}^2}\sum_{f=0}^{N_{kl}-1} H_{kl}^*(f)\exp\left[i\frac{2\pi}{N_{kl}}\langle f,u'\rangle\right]\exp\left[-i\frac{2\pi}{N}\langle u',f'\rangle\right]\exp\left[i\frac{2\pi}{N}\langle u',f''\rangle\right] \\
-\sum_{u'=-\frac{N}{2}}^{\frac{N}{2}-1}\frac{1}{N_{kl}^2}\sum_{f=0}^{N_{kl}-1} H_{kl}^*(f)\exp\left[i\frac{2\pi}{N_{kl}}\langle f,u'\rangle\right]\exp\left[-i\frac{2\pi}{N}\langle u',f'\rangle\right] \\
\left.\times\sum_{u'=-\frac{N}{2}}^{\frac{N}{2}-1}\frac{1}{N_{kl}^2}\sum_{f=0}^{N_{kl}-1} H_{kl}(f)\exp\left[i\frac{2\pi}{N_{kl}}\langle f,u'\rangle\right]\exp\left[-i\frac{2\pi}{N}\langle u',f'\rangle\right]\exp\left[-i\frac{2\pi}{N}\langle u',f''\rangle\right]\right]
\end{aligned} \tag{B.9}
$$

In a way analogous to the derivation by Paxman, the overall derivation of the metric L_M can be expressed as shown in equation (B.10).

$$
\frac{\partial}{\partial\alpha_j}L_M = \sum_{f''=0}^{N-1}\sum_{k=1}^{K} C_k^b\frac{\partial}{\partial\alpha_j}S_k^b + c.c = \sum_{f''=0}^{N-1}\sum_{k=1}^{K} C_k^b\sum_{l=1}^{\Lambda}\frac{\partial}{\partial\alpha_j}S_{kl} + c.c \tag{B.10}
$$

In this equation, the term C_k^b is defined as shown in equation (B.11), similar to the definition used by Paxman.

$$
C_k^b(f) = \frac{\sum_{j=1}^{K}|S_j^b(f)|^2\left(\sum_{l=1}^{K} I_l(f)S_l^{b*}(f)\right)I_k^*(f) - |\sum_{j=1}^{K} I_j(f)S_j^{b*}(f)|^2 S_k^{b*}(f)}{\left(\sum_{j=1}^{K}|S_j^b(f)|^2\right)^2} \tag{B.11}
$$

Inserting equation (B.9) into (B.10) results in the expression shown in equation (B).

$$
\begin{aligned}
\frac{\partial}{\partial\alpha_j}L_M = \sum_{f''=0}^{N-1}\sum_{k=1}^{K} Z_k^b(f'')\sum_{l=1}^{\Lambda}\frac{i}{N^2}\frac{\bar{\lambda}}{\lambda_l}\sum_{f'=0}^{N-1}\sum_{u'=-\frac{N}{2}}^{\frac{N}{2}-1}\frac{1}{N_{kl}^2}\sum_{f=0}^{N_{kl}-1} Z_j(f)\exp\left[i\frac{2\pi}{N_{kl}}\langle f,u'\rangle\right]\exp\left[-i\frac{2\pi}{N}\langle u',f'\rangle\right] \\
\times\left[\mathbf{H}_{kl}(f')\sum_{u'=-\frac{N}{2}}^{\frac{N}{2}-1} h_{kl}^*(-u')\exp\left[-i\frac{2\pi}{N}\langle u',f'\rangle\right]\exp\left[i\frac{2\pi}{N}\langle u',f''\rangle\right]\right. \\
\left.-\mathbf{H}_{kl}^*(f')\sum_{u'=-\frac{N}{2}}^{\frac{N}{2}-1} h_{kl}(u')\exp\left[-i\frac{2\pi}{N}\langle u',f'\rangle\right]\exp\left[-i\frac{2\pi}{N}\langle u',f''\rangle\right]\right] + c.c
\end{aligned} \tag{B.12}
$$

Note that during application of the Fourier and inverse Fourier transforms to arrive at equation it has been taken into account that when the complex conjugate of a function is transformed, the rule presented in equation (B.13) should be applied.

$$
\mathscr{F}\{x^*(f)\} = X^*(-f) \tag{B.13}
$$

The function C_k^b can then be moved into the brackets to arrive at equation (B.14).

$$\frac{\partial}{\partial \alpha_j} L_M = i\bar{\lambda} \sum_{f'=0}^{N-1} \sum_{k=1}^{K} \sum_{l=1}^{\Lambda} \frac{1}{N^2 \lambda_l} \sum_{u'=-\frac{N}{2}}^{\frac{N}{2}-1} \frac{1}{N_{kl}^2} \sum_{f=0}^{N_{kl}-1} Z_j(f) \exp\left[i\frac{2\pi}{N_{kl}}\langle f, u'\rangle\right] \exp\left[-i\frac{2\pi}{N}\langle u', f'\rangle\right]$$
$$\left[\mathbf{H}_{kl}(f') \sum_{u'=-\frac{N}{2}}^{\frac{N}{2}-1} h_{kl}^*(-u') \sum_{f''=0}^{N-1} C_k^b(f'') \exp\left[i\frac{2\pi}{N}\langle f'', u'\rangle\right] \exp\left[-i\frac{2\pi}{N}\langle u', f'\rangle\right]\right.$$
$$\left. -\mathbf{H}_{kl}^*(f') \sum_{u'=-\frac{N}{2}}^{\frac{N}{2}-1} h_{kl}(u') \sum_{f''=0}^{N-1} C_k^b(f'') \exp\left[-i\frac{2\pi}{N}\langle f'', u'\rangle\right] \exp\left[-i\frac{2\pi}{N}\langle u', f'\rangle\right]\right] + c.c \quad \text{(B.14)}$$

For conciseness and readability, the wavelength dependent basis function $\mathbf{Z}_{jl}$ can be introduced, expressed as shown in equation (B.15).

$$\mathbf{Z}_{jl} = \sum_{u'=-\frac{N}{2}}^{\frac{N}{2}-1} \frac{1}{N_{kl}^2} \sum_{f=0}^{N_{kl}-1} Z_j(f) \exp\left[i\frac{2\pi}{N_{kl}}\langle f, u'\rangle\right] \exp\left[-i\frac{2\pi}{N}\langle u', f'\rangle\right] \quad \text{(B.15)}$$

Inserting this into equation (B.14) yields equation (B.16). In this equation another change of variable has been introduced: $f''' = -f''$.

$$\frac{\partial}{\partial \alpha_j} L_M = i\bar{\lambda} \sum_{f'=0}^{N-1} \sum_{k=1}^{K} \sum_{l=1}^{\Lambda} \frac{1}{N^2 \lambda_l} \mathbf{Z}_{jl} \left[\mathbf{H}_{kl}(f') \sum_{u'=-\frac{N}{2}}^{\frac{N}{2}-1} h_{kl}^*(-u') \sum_{f''=0}^{N-1} C_k^b(f'') \exp\left[i\frac{2\pi}{N}\langle f'', u'\rangle\right] \exp\left[-i\frac{2\pi}{N}\langle u', f'\rangle\right]\right.$$
$$\left. -\mathbf{H}_{kl}^*(f') \sum_{u'=-\frac{N}{2}}^{\frac{N}{2}-1} h_{kl}(u') \sum_{f'''=0}^{N-1} C_k^b(-f''') \exp\left[i\frac{2\pi}{N}\langle f''', u'\rangle\right] \exp\left[-i\frac{2\pi}{N}\langle u', f'\rangle\right]\right] + c.c \quad \text{(B.16)}$$

As explained by Paxman, the function C_k^b is Hermitian. Which means that $C_k^b(-f''') = C_k^{b*}(f''')$. Applying this to the second term in equation (B.16) and subsequently substituting f'' for f''' for readability one arrives at equation (B.17).

$$\frac{\partial}{\partial \alpha_j} L_M = i\bar{\lambda} \sum_{f'=0}^{N-1} \sum_{k=1}^{K} \sum_{l=1}^{\Lambda} \frac{1}{N^2 \lambda_l} \mathbf{Z}_{jl} \left[\mathbf{H}_{kl}(f') \sum_{u'=-\frac{N}{2}}^{\frac{N}{2}-1} h_{kl}^*(-x') \sum_{f''=0}^{N-1} C_k^b(f'') \exp\left[i\frac{2\pi}{N}\langle f'', u'\rangle\right] \exp\left[-i\frac{2\pi}{N}\langle u', f'\rangle\right]\right.$$
$$\left. -\mathbf{H}_{kl}^*(f') \sum_{u'=-\frac{N}{2}}^{\frac{N}{2}-1} h_{kl}(u') \sum_{f''=0}^{N-1} C_k^{b*}(f'') \exp\left[i\frac{2\pi}{N}\langle f'', u'\rangle\right] \exp\left[-i\frac{2\pi}{N}\langle u', f'\rangle\right]\right] + c.c \quad \text{(B.17)}$$

Noting that the second term is the complex conjugate of the first term this can be further simplified to the expression shown in equation (B.18).

$$\frac{\partial}{\partial \alpha_j} L_M = 2i\bar{\lambda} \sum_{f'=0}^{N-1} \sum_{k=1}^{K} \sum_{l=1}^{\Lambda} \frac{1}{N^2 \lambda_l} \mathbf{Z}_{jl} \mathbf{H}_{kl}(f') \sum_{u'=-\frac{N}{2}}^{\frac{N}{2}-1} h_{kl}^*(-u') \sum_{f''=0}^{N-1} C_k^b(f'') \exp\left[i\frac{2\pi}{N}\langle f'', u'\rangle\right] \exp\left[-i\frac{2\pi}{N}\langle u', f'\rangle\right] + c.c \quad \text{(B.18)}$$

Finally, noting that because of the combination of the i term in front of the equation and the summation of with its complex conjugate the imaginary part is multiplied by two while the real part cancels out, one arrives at a practical final expression for the analytic gradient of the broadband metric presented in equation (B.19)

$$\frac{\partial}{\partial \alpha_j} L_M = -4\bar{\lambda} \sum_{f'=0}^{N-1} \sum_{k=1}^{K} \sum_{l=1}^{\Lambda} \frac{1}{N^2 \lambda_l} \mathbf{Z}_{jl} \times \mathrm{Im} \left\{ \mathbf{H}_{kl}(f') \sum_{u'=-\frac{N}{2}}^{\frac{N}{2}-1} h_{kl}^*(-x') \sum_{f''=0}^{N-1} C_k^b(f'') \exp\left[i\frac{2\pi}{N}\langle f'', u'\rangle\right] \exp\left[-i\frac{2\pi}{N}\langle u', f'\rangle\right] \right\} \quad \text{(B.19)}$$

C

Simulation Results

C.1. Parametric Study Results

Table C.1: Information about the performance for the 3 and 2 detector configurations.

Configuration	**Average Iteration Count [#]**	**Average Time per Iteration [s]**	**Average Run Time [s]**	**Simulations <1000 Iterations [#]**
3 Detectors	915	0.166	152.41	23
2 Detectors	973	0.114	110.66	11

Configuration	**Average Original Strehl Ratio [-]**	**Average Residual Strehl Ratio [-]**					
		Farm	**Sea**	**Storm**	**Mountains**	**City**	**Overall**
3 Detectors	0.54	0.82	0.66	0.56	0.8	0.78	0.72
2 Detectors	0.54	0.81	0.58	0.6	0.79	0.65	0.69

Table C.2: Information about the performance for the $5\mu m$, $8\mu m$ and $11\mu m$ pixel pitch configurations.

Configuration	**Average Iteration Count** [#]	**Average Time per Iteration** [s]	**Average Run Time** [s]	**Simulations <1000 Iterations** [#]
5 μm pitch	964	0.101	96.57	15
8 μm pitch	928	0.098	91.26	12
11 μm pitch	952	0.102	97.1	15

Configuration	**Average Original Strehl Ratio** [-]	**Average Residual Strehl Ratio** [-]					
		Farm	**Sea**	**Storm**	**Mountains**	**City**	**Overall**
5 μm pitch	0.57	0.8	0.57	0.58	0.87	0.63	0.69
8 μm pitch	0.56	0.79	0.56	0.31	0.52	0.54	0.54
11 μm pitch	0.56	0.56	0.67	0.24	0.57	0.52	0.51

Table C.3: Information about the performance for the $0.01mm$, $0.25mm$, $0.5mm$, $0.75mm$ and $1mm$ TDI-2 defocus configurations.

Configuration	**Average Iteration Count** [#]	**Average Time per Iteration** [s]	**Average Run Time** [s]	**Simulations <1000 Iterations** [#]
0.01mm defocus	824	0.119	98.11	30
0.25mm defocus	866	0.118	101.95	27
0.5mm defocus	950	0.118	112.09	12
0.75mm defocus	996	0.118	117.34	3
1mm defocus	997	0.118	117.98	1

Configuration	**Average Original Strehl Ratio** [-]	**Average Residual Strehl Ratio** [-]					
		Farm	**Sea**	**Storm**	**Mountains**	**City**	**Overall**
0.01mm defocus	0.59	0.52	0.41	0.34	0.49	0.52	0.46
0.25mm defocus	0.59	0.8	0.74	0.46	0.7	0.72	0.69
0.5mm defocus	0.59	0.8	0.6	0.6	0.76	0.7	0.69
0.75mm defocus	0.59	0.75	0.53	0.6	0.65	0.51	0.61
1mm defocus	0.59	0.59	0.52	0.49	0.64	0.33	0.51

Table C.4: Information about the performance for the nominal field separation and the 1.5×, 2× and 2.5× nominal field separation.

Configuration	**Average Iteration Count [#]**	**Average Time per Iteration [s]**	**Average Run Time [s]**	**Simulations <1000 Iterations [#]**
nominal separation	946	0.112	106.16	12
1.5x nominal	956	0.112	106.7	12
2x nominal	958	0.112	107.49	12
2.5x nominal	948	0.112	105.78	14

Configuration	**Average Original Strehl Ratio [-]**	**Average Residual Strehl Ratio [-]**					
		Farm	**Sea**	**Storm**	**Mountains**	**City**	**Overall**
nominal separation	0.55	0.69	0.6	0.52	0.77	0.72	0.66
1.5x nominal	0.55	0.7	0.59	0.49	0.78	0.72	0.66
2x nominal	0.55	0.74	0.59	0.52	0.79	0.72	0.67
2.5x nominal	0.55	0.73	0.59	0.5	0.78	0.73	0.67

Table C.5: Information about the performance for the nominal field separation and the 1.5×, 2× and 2.5× nominal mechanical drift tolerances.

Configuration	**Average Iteration Count [#]**	**Average Time per Iteration [s]**	**Average Run Time [s]**	**Simulations <1000 Iterations [#]**
nominal drift tolerances	968	0.118	114.3	9
1.5x nominal drift	985	0.117	114.87	5
2x nominal drift	991	0.117	115.86	3
2.5x nominal drift	987	0.116	114.09	4

Configuration	**Average Original Strehl Ratio [-]**	**Average Residual Strehl Ratio [-]**					
		Farm	**Sea**	**Storm**	**Mountains**	**City**	**Overall**
nominal drift tolerances	0.54	0.68	0.58	0.64	0.77	0.68	0.67
1.5x nominal drift	0.36	0.66	0.44	0.51	0.64	0.52	0.55
2x nominal drift	0.25	0.46	0.37	0.44	0.56	0.48	0.46
2.5x nominal drift	0.2	0.35	0.26	0.43	0.45	0.28	0.35

Table C.6: Information about the performance for 0, 1, 2, 3 and 5 μm of unknown defocus error in TDI-2.

Configuration	**Average Iteration Count** [#]	**Average Time per Iteration** [s]	**Average Run Time** [s]	**Simulations <1000 Iterations** [#]
0 μm error	951	0.103	97.62	16
1 μm error	953	0.102	96.95	14
2 μm error	954	0.102	97.64	16
3 μm error	957	0.102	97.58	14
5 μm error	948	0.103	97.48	16

Configuration	**Average Original Strehl Ratio** [-]	**Average Residual Strehl Ratio** [-]					
		Farm	**Sea**	**Storm**	**Mountains**	**City**	**Overall**
0 μm error	0.56	0.76	0.57	0.56	0.84	0.69	0.69
1 μm error	0.56	0.76	0.57	0.56	0.85	0.7	0.69
2 μm error	0.56	0.76	0.57	0.56	0.85	0.7	0.69
3 μm error	0.56	0.76	0.57	0.56	0.85	0.7	0.69
5 μm error	0.56	0.76	0.57	0.56	0.85	0.7	0.69

Table C.7: Information about the performance for Gaussian Noise Signal to Noise ratios of SNR = 100, $SNR = 75$, $SNR = 50$ and $SNR = 10$.

Configuration	**Average Iteration Count** [#]	**Average Time per Iteration** [s]	**Average Run Time** [s]	**Simulations <1000 Iterations** [#]
SNR = 100	974	0.135	131.49	8
SNR = 75	970	0.135	131.22	12
SNR = 50	971	0.134	130.41	11
SNR = 10	949	0.134	126.82	12

Configuration	**Average Original Strehl Ratio** [-]	**Average Residual Strehl Ratio** [-]					
		Farm	**Sea**	**Storm**	**Mountains**	**City**	**Overall**
SNR = 100	0.56	0.75	0.58	0.54	0.8	0.64	0.66
SNR = 75	0.56	0.74	0.58	0.55	0.8	0.64	0.66
SNR = 50	0.56	0.74	0.58	0.49	0.81	0.64	0.65
SNR = 10	0.56	0.8	0.56	0.41	0.77	0.64	0.64

Table C.8: Information about the performance for 10^4, $7 \cdot 10^3$, $5 \cdot 10^3$ and $\cdot 10^3$ average photon/pixel values.

Configuration	**Average Iteration Count** [#]	**Average Time per Iteration** [s]	**Average Run Time** [s]	**Simulations <1000 Iterations** [#]
1×10^4 photons average	973	0.104	101.31	10
7×10^3 photons average	965	0.104	99.94	12
5×10^3 photons average	966	0.103	99.91	16
1×10^3 photons average	958	0.103	99.06	16

Configuration	**Average Original Strehl Ratio** [-]	**Average Residual Strehl Ratio** [-]					
		Farm	**Sea**	**Storm**	**Mountains**	**City**	**Overall**
1×10^4 photons average	0.55	0.8	0.58	0.59	0.85	0.67	0.7
7×10^3 photons average	0.55	0.79	0.57	0.59	0.85	0.67	0.69
5×10^3 photons average	0.55	0.8	0.58	0.56	0.85	0.66	0.69
1×10^3 photons average	0.55	0.8	0.54	0.42	0.84	0.66	0.65

Table C.9: Information about the performance for 0%, 0.1%, 1% and 10% chance dead pixels, both with and without correction.

Configuration	**Average Iteration Count** [#]	**Average Time per Iteration** [s]	**Average Run Time** [s]	**Simulations <1000 Iterations** [#]
0% chance	973	0.152	147.52	8
0.1% chance (uncorrected)	944	0.151	142.15	15
0.1% chance (corrected)	978	0.151	147.42	9
1% chance (uncorrected)	913	0.151	137.36	21
1% chance (corrected)	946	0.151	143.4	16
10% chance (uncorrected)	854	0.151	128.76	30
10% chance (corrected)	965	0.15	144.42	8

Configuration	**Average Original Strehl Ratio** [-]	**Average Residual Strehl Ratio** [-]					
		Farm	**Sea**	**Storm**	**Mountains**	**City**	**Overall**
0% chance	0.53	0.75	0.5	0.59	0.79	0.64	0.65
0.1% chance (uncorrected)	0.53	0.48	0.4	0.33	0.6	0.63	0.49
0.1% chance (corrected)	0.53	0.75	0.5	0.59	0.79	0.64	0.65
1% chance (uncorrected)	0.53	0.34	0.32	0.22	0.5	0.52	0.38
1% chance (corrected)	0.53	0.74	0.5	0.44	0.78	0.64	0.62
10% chance (uncorrected)	0.53	0.27	0.24	0.27	0.3	0.31	0.28
10% chance (corrected)	0.53	0.55	0.42	0.29	0.69	0.6	0.51

Table C.10: Information about the performance for the *Farm*, *Sea*, *Storm*, *Mountains* and *City* scenes.

Configuration	**Average Iteration Count [#]**	**Average Time per Iteration [s]**	**Average Run Time [s]**	**Simulations <1000 Iterations [#]**
Farm	962	0.105	101.27	25
Sea	1000	0.105	105.46	0
Storm	984	0.105	102.97	6
Mountains	887	0.106	93.69	33
City	998	0.105	104.84	1

Configuration	**Average Original Strehl Ratio [-]**	**Average Residual Strehl Ratio [-]**
		Overall
Farm	0.56	0.78
Sea	0.56	0.57
Storm	0.56	0.59
Mountains	0.56	0.84
City	0.56	0.68

Table C.11: Information about the performance for simulations including Zernike polynomials up to degree 8, 7, 6, 5, 4, 3, 2 and 1 respectively.

Configuration	**Average Iteration Count [#]**	**Average Time per Iteration [s]**	**Average Run Time [s]**	**Simulations <1000 Iterations [#]**
up to order 8	972	0.11	106.71	13
up to order 7	964	0.099	95.99	12
up to order 6	979	0.09	88.51	7
up to order 5	984	0.082	80.69	10
up to order 4	977	0.075	73.16	8
up to order 3	991	0.068	67.83	4
up to order 2	993	0.064	63.58	3
up to order 1	1000	0.06	60.27	1

Configuration	**Average Original Strehl Ratio [-]**	**Average Residual Strehl Ratio [-]**					
		Farm	**Sea**	**Storm**	**Mountains**	**City**	**Overall**
up to order 8	0.55	0.76	0.56	0.54	0.81	0.64	0.66
up to order 7	0.55	0.76	0.58	0.53	0.83	0.67	0.68
up to order 6	0.55	0.78	0.61	0.64	0.85	0.72	0.72
up to order 5	0.55	0.8	0.57	0.63	0.86	0.79	0.73
up to order 4	0.55	0.79	0.59	0.71	0.83	0.8	0.75
up to order 3	0.55	0.7	0.61	0.67	0.74	0.75	0.69
up to order 2	0.55	0.69	0.59	0.61	0.71	0.76	0.67
up to order 1	0.55	0.67	0.56	0.57	0.57	0.64	0.6

Table C.12: Information about run time and iteration counts for simulations using a learning rate κ fo $1\cdot10^{-4}$, $5\cdot10^{-4}$, $1\cdot10^{-3}$, $5\cdot10^{-3}$ and $1\cdot10^{-2}$.

Configuration	Average Iteration Count [#]	Average Time per Iteration [s]	Average Run Time [s]	Simulations <1000 Iterations [#]
$\kappa = 1\times10^{-4}$	1000	0.131	130.77	0
$\kappa = 5\times10^{-4}$	1000	0.134	134.25	0
$\kappa = 1\times10^{-3}$	964	0.133	128.27	13
$\kappa = 5\times10^{-3}$	1000	0.173	172.83	0
$\kappa = 1\times10^{-2}$	166	0.13	21.55	50

Configuration	Average Original Strehl Ratio [-]	Average Residual Strehl Ratio [-]					
		Farm	Sea	Storm	Mountains	City	Overall
$\kappa = 1\times10^{-4}$	0.55	0.62	0.64	0.63	0.61	0.61	0.62
$\kappa = 5\times10^{-4}$	0.55	0.75	0.68	0.66	0.77	0.74	0.72
$\kappa = 1\times10^{-3}$	0.55	0.79	0.58	0.53	0.83	0.67	0.68
$\kappa = 5\times10^{-3}$	0.55	0.75	0.68	0.66	0.77	0.74	0.72
$\kappa = 1\times10^{-2}$	0.55	0.8	0.63	0.66	0.8	0.73	0.72

Table C.13: Information about the performance for the configurations using 1, 3, 7, 11 and 15 sample wavelengths to sample the detector band respectively.

Configuration	Average Iteration Count [#]	Average Time per Iteration [s]	Average Run Time [s]	Simulations <1000 Iterations [#]
1 Sample	993	0.028	27.77	5
3 Samples	966	0.058	56.37	14
7 Samples	964	0.121	116.59	13
11 Samples	972	0.185	180.17	10
15 Samples	973	0.253	246.77	14

Configuration	Average Original Strehl Ratio [-]	Average Residual Strehl Ratio [-]					
		Farm	Sea	Storm	Mountains	City	Overall
1 Sample	0.55	0.75	0.55	0.51	0.8	0.64	0.65
3 Samples	0.55	0.79	0.59	0.55	0.83	0.68	0.69
7 Samples	0.55	0.79	0.58	0.53	0.83	0.67	0.68
11 Samples	0.55	0.79	0.58	0.54	0.84	0.67	0.68
15 Samples	0.55	0.79	0.58	0.54	0.85	0.67	0.69

Table C.14: Information about the performance for suframe sizes of 256 × 256, 128 × 128 and 64 × 64.

Configuration	Average Iteration Count [#]	Average Time per Iteration [s]	Average Run Time [s]	Simulations <1000 Iterations [#]
256 × 256 pixels	848	0.267	228.13	34
128 × 128 pixels	969	0.104	100.93	11
64 × 64 pixels	905	0.034	30.84	22

Configuration	Average Original Strehl Ratio [-]	Average Residual Strehl Ratio [-]					
		Farm	Sea	Storm	Mountains	City	Overall
256 × 256 pixels	0.55	0.76	0.75	0.65	0.82	0.7	0.74
128 × 128 pixels	0.55	0.75	0.58	0.56	0.84	0.64	0.67
64 × 64 pixels	0.55	0.66	0.66	0.38	0.66	0.35	0.54

Table C.15: Information about the performance for configurations with apodization ratios of 0.0, 0.25, 0.5, 0.75 and 1.0 respectively.

Configuration	Average Iteration Count [#]	Average Time per Iteration [s]	Average Run Time [s]	Simulations <1000 Iterations [#]
apodization ratio = 0.0	959	0.105	100.62	16
apodization ratio = 0.25	996	0.107	106.57	4
apodization ratio = 0.5	965	0.107	103.25	15
apodization ratio = 0.75	948	0.106	100.48	14
apodization ratio = 1.0	949	0.106	100.59	17

Configuration	Average Original Strehl Ratio [-]	Average Residual Strehl Ratio [-]					
		Farm	Sea	Storm	Mountains	City	Overall
apodization ratio = 0.0	0.56	0.8	0.57	0.56	0.8	0.69	0.68
apodization ratio = 0.25	0.56	0.65	0.53	0.29	0.75	0.72	0.59
apodization ratio = 0.5	0.56	0.77	0.6	0.45	0.77	0.72	0.66
apodization ratio = 0.75	0.56	0.82	0.58	0.46	0.82	0.72	0.68
apodization ratio = 1.0	0.56	0.82	0.58	0.53	0.8	0.71	0.69

Table C.16: Information about the performance for the combined simulations.

Configuration	Average Iteration Count [#]	Average Time per Iteration [s]	Average Run Time [s]	Simulations <1000 Iterations [#]
Configuration 1	847	0.108	91.18	23
Configuration 2	695	0.288	199.72	40
Configuration 3	729	0.183	133.4	34
Configuration 4	125	0.387	47.98	50
Configuration 5	123	0.2	24.47	50
Configuration 6	900	0.233	209.72	17
Configuration 7	917	0.111	102.04	14
Configuration 8	176	0.223	39.12	50
Configuration 9	178	0.115	20.5	50

Configuration	Average Original Strehl Ratio [-]	Average Residual Strehl Ratio [-]					
		Farm	**Sea**	**Storm**	**Mountains**	**City**	**Overall**
Configuration 1	0.57	0.79	0.64	0.4	0.68	0.76	0.65
Configuration 2	0.57	0.77	0.63	0.57	0.66	0.79	0.68
Configuration 3	0.57	0.76	0.62	0.58	0.66	0.79	0.68
Configuration 4	0.57	0.75	0.59	0.59	0.65	0.78	0.67
Configuration 5	0.57	0.75	0.58	0.58	0.66	0.78	0.67
Configuration 6	0.57	0.78	0.61	0.54	0.65	0.83	0.68
Configuration 7	0.57	0.79	0.62	0.54	0.65	0.82	0.68
Configuration 8	0.57	0.78	0.59	0.6	0.65	0.81	0.69
Configuration 9	0.57	0.8	0.61	0.6	0.65	0.81	0.69

Table C.17: Information about the performance for the combined defocus simulations.

Configuration	Average Iteration Count [#]	Average Time per Iteration [s]	Average Run Time [s]	Simulations <1000 Iterations [#]
Configuration 1	186	0.055	10.08	50
Configuration 2	176	0.116	20.44	50
Configuration 3	235	0.116	27.22	50
Configuration 4	261	0.116	30.26	50
Configuration 5	278	0.117	32.33	50

Configuration	Average Original Strehl Ratio [-]	Average Residual Strehl Ratio [-]					
		Farm	Sea	Storm	Mountains	City	Overall
Configuration 1	0.55	0.79	0.79	0.54	0.82	0.86	0.76
Configuration 2	0.55	0.72	0.77	0.68	0.74	0.81	0.75
Configuration 3	0.55	0.77	0.78	0.65	0.82	0.83	0.77
Configuration 4	0.55	0.78	0.8	0.6	0.81	0.79	0.76
Configuration 5	0.55	0.75	0.71	0.51	0.75	0.77	0.7

C.2. Multispectral Study Results

Table C.18: Information about the performance for the simulation without multispectral data in the loop and for the simulation with multispectral data in the loop.

Configuration	Average Iteration Count [#]	Average Time per Iteration [s]	Average Run Time [s]	Simulations <1000 Iterations [#]
Configuration 1 No Multispectral	265	0.042	11.08	50
Configuration 1 Multispectral	263	0.038	9.9	50
Configuration 2 No Multispectral	256	0.105	26.95	50
Configuration 2 Multispectral	257	0.111	28.35	50

Configuration	Average Original Strehl Ratio [-]	Average Residual Strehl Ratio [-]					
		Farm	Sea	Storm	Mountains	City	Overall
Configuration 1 No Multispectral	0.53	0.86	0.66	0.7	0.88	0.86	0.79
Configuration 1 Multispectral	0.53	0.85	0.68	0.71	0.89	0.85	0.79
Configuration 2 No Multispectral	0.53	0.8	0.79	0.66	0.78	0.79	0.77
Configuration 2 Multispectral	0.53	0.79	0.77	0.66	0.78	0.8	0.76

C.3. Subframe Selection Results

Table C.19: Information about the performance for the simulation comparing different subframe selection algorithms.

Configuration	Average Iteration Count [#]	Average Time per Iteration [s]	Average Run Time [s]	Simulations <1000 Iterations [#]
Center Frame	254	0.033	8.43	50
Bright Peak	249	0.033	8.08	50
Dark Borders	245	0.033	7.99	50

Configuration	Average Original Strehl Ratio [-]	Average Residual Strehl Ratio [-]					
		Farm	Sea	Storm	Mountains	City	Overall
Center Frame	0.56	0.9	0.53	0.64	0.92	0.8	0.76
Bright Peak	0.56	0.94	0.76	0.7	0.88	0.88	0.83
Dark Borders	0.56	0.92	0.7	0.59	0.86	0.86	0.79

C.4. Open-Loop Performance Results

Table C.20: Performance of the two Open Loop configurations in terms of run time, iteration count, Strehl ratio and RMS error.

Configuration	**Average Iteration Count [#]**	**Average Time per Iteration [s]**	**Average Run Time [s]**	**Simulations <1000 Iterations [#]**
Configuration 1	242	0.084	20.19	500
Configuration 2	237	0.205	45.26	500

Configuration	**Average Original Strehl Ratio [-]**	**Average Residual Strehl Ratio [-]**					
		Farm	**Sea**	**Storm**	**Mountains**	**City**	**Overall**
Configuration 1	0.41	0.95	0.85	0.74	0.92	0.95	0.88
Configuration 2	0.4	0.94	0.88	0.69	0.93	0.94	0.88

Configuration	**Average Original RMS [-]**	**Average Residual RMS [-]**					
		Farm	**Sea**	**Storm**	**Mountains**	**City**	**Overall**
Configuration 1	0.63	0.046	0.104	0.112	0.071	0.049	0.077
Configuration 2	0.628	0.044	0.1	0.125	0.066	0.047	0.076

Table C.21: Performance of the two Open Loop configurations in terms of run time, iteration count, Strehl ratio and RMS error after correction.

Configuration	**Average Iteration Count [#]**	**Average Time per Iteration [s]**	**Average Run Time [s]**	**Simulations <1000 Iterations [#]**
Configuration 1	257	0.082	20.86	500
Configuration 2	254	0.205	47.69	500

Configuration	**Average Original Strehl Ratio [-]**	**Average Residual Strehl Ratio [-]**					
		Farm	**Sea**	**Storm**	**Mountains**	**City**	**Overall**
Configuration 1	0.41	0.95	0.87	0.76	0.93	0.95	0.89
Configuration 2	0.4	0.95	0.91	0.72	0.95	0.95	0.89

Configuration	**Average Original RMS [-]**	**Average Residual RMS [-]**					
		Farm	**Sea**	**Storm**	**Mountains**	**City**	**Overall**
Configuration 1	0.63	0.034	0.057	0.083	0.042	0.032	0.05
Configuration 2	0.628	0.032	0.043	0.088	0.034	0.032	0.046

C.5. Closed-Loop Performance Results

Table C.22: Results of the closed-loop performance analysis

Parameter	**Configuration 1**		**Configuration 2**		**Configuration 3**	
field angle	**0**	**0.3**	**0**	**0.3**	**0**	**0.3**
Average original SR [-]	0.5	0.51	0.83	0.83	0.76	0.74
Average residual SR [-]	0.69	0.66	0.75	0.71	0.71	0.64
Average optimum SR [-]	0.77	0.75	0.9	0.88	0.86	0.8
cases SR above 0.8 [%]	62	58	94	87	81	60
Average original RMS [λ_0]	0.24	0.24	0.09	0.09	0.11	0.11
Average residual RMS [λ_0]	0.31	0.32	0.15	0.16	0.21	0.23
Average optimum RMS [λ_0]	0.12	0.12	0.06	0.07	0.08	0.1
Cases RMS below 0.07 [%]	37	26	73	56	45	22

D

Phase Diversity Toolbox File Overview

```
FORTA Phase Diversity Toolbox
├── GenerateSettings.m
├── LoadScene.m
├── AberrateScene.m
├── SimulateMeasurement.m
│   ├── BrightPeak.m
│   └── DarkBorders.m
├── CreateZernikePolynomials.m
├── EstimateWavefront.m
│   ├── RunOptimizer.m
│   │   ├── RemoveEdgeArtifacts.m
│   │   ├── RemoveEdgeArtifactsInv.m
│   │   ├── ComputeMetric.m
│   │   └── ComputeGradient.m
│   └── SegmentCorrection.m
├── DeconvoluteImage.m
└── VizualizeOutput.m
```

Bibliography

[1] Planet RapidEye. Altotting, germany. https://www.effigis.com/en/solutions/satellite-images/satellite-image-samples/.

[2] Apollomapping. Satellite image of the Louvre, Paris taken by DigitalGlobe's WorldView 4 satellite. https://apollomapping.com/blog/30-cm-color-worldview-3-4-image-month-paris-france/louvre_museum_paris_france_10_15_2017_wv4_30cmcolor_enhance.

[3] DigitalGlobe. Schematic representation of the size of the worldview-4 system. http://blog.digitalglobe.com/news/frequently-asked-questions-about-worldview-4/.

[4] Cyberchalky. Seawave diffraction. https://cyberchalky.wordpress.com/.

[5] J.W. Goodman. *Introduction to Fourier Optics*, volume 8. McGraw-Hill Series in Electrical and Computer Engineering, 1996.

[6] Remi J. Oude kerk delft. https://nl.wikipedia.org/wiki/Delft#/media/File:Delft_(13).JPG.

[7] Fleck A. Lakshminarayanan, V. *Zernike polynomials: A guide*, volume 58. 2011.

[8] R.H. van Rijn. Nachtwacht. https://www.rijksmuseum.nl/nl/zoeken/objecten?q=nachtwacht&p=1&ps=12&st=Objects&ii=0#/SK-C-5,0.

[9] D. Dolkens. A deployable telescope for sub-meter resolutions from microsatellite platforms. 2015.

[10] J.M. Goei B.T.C. de Gill E.K.A Dolkens, D. Kuiper. Design and optimization of a deployable telescope for earth observation.

[11] Ba J.L. Kingma, D.P. Adam: A Method for Stochastic Optimization. *Conference procedings of ICLR 2015*, 2015.

[12] NASA. NASA Space Science Data Coordinated Archive - Nimbus 1. https://nssdc.gsfc.nasa.gov/nmc/spacecraft/display.action?id=1964-052A. [Online; accessed 3-January-2008].

[13] DigitalGlobe. Worldview-4 datasheet.

[14] spacepolicyonline.com/news/enhancedview-news-not-so-rosy-for-geoeye.

[15] C. Huygens. *Traite de la Lumiere*. Opticks, 1690.

[16] M.A. Fresnel. Memoire sur la diffraction de la lumiere, ou l'on examine particulierement le phenomene des franges colorees que presentent les ombres des corps eclaires par un point lumineux. *Annales de la chimie et de physique*, 1:239–281, Oct 1815.

[17] G.B. Airy. On the Diffraction of an Object-glass with Circular Aperture. *Transactions of the Cambridge Philosophical Society*, 1835.

[18] F.R.S. Lord Rayleigh. Investigations in optics, with special reference to the spectroscope. *Philosophical magazine and journal of science*, Oct 1879.

[19] G.P van Marrewijk. Design of an aberration correction system for a deployable space telescope, 2018.

[20] E. Hecht. Addison-Wesley, 2002.

[21] D. Korsch. Closed form solution for three-mirror telescopes, corrected for spherical aberration, coma, astigmatism, and field curvature. *Applied optics*, 11(12):2986–7, 1972.

[22] B.T. van Putten. Design of the deployment mechanism for the primary mirror elements of a deployable space telescope, 2017.

[23] M. Corvers. Design of a Primary Mirror Deployment Mechanism for a Deployable Space Telescope. 2018.

[24] S.M. Pepper. Primary Mirror Fine Positioning Mechanism for a Deployabel Space Telescope, year = 2018.

[25] J.W. Lopes Barreto. Deployable Space Telescope: Optimal Boom Design for High Precision Deployment of the Secondary Mirror. 2017.

[26] A. Krikken. Design of the Secondary Mirror Support Structure for the Deployable Space Telescope. 2018.

[27] M. Voorn. Initiating the Testing pPhase of a Deployable Space Telescope: An Experimental Characterisation of Hysteresis in CORE Hinges. 2019.

[28] W.J. Smith. *Optical The Design of Optical Systems.* 2008.

[29] R.V. Shack. Production and use of a lenticular hartmann screen. *Journal of the optical society of America*, 1971.

[30] J.F. Hartmann. Bemerkungen uber den bau und die justirung von spektrographen. *Zeitschrift für Instrumentenkunde*, 1900.

[31] Radick R.R. Rimmele T.R. Radick R.R Rimmele, T.R. Solar observatory. (September 1998), 2018.

[32] Rousset G. Fontanella J.C. Michau, V. Wavefront sensing of extended sources. 1993.

[33] V.M. Radhakrishnan. Design of an adaptive optics system for a deployable space telescope, 2016.

[34] Sivokon V.P. Vorontsov, M.A. Stochastic parallel-gradient-descent technique for wave-front phase-distortion correction. *Journal of the optical society of America*, 15(10), 1998.

[35] Dorrance P. Gleichman K. Jonik J. Liskow D. Lapprich H. Naik V. Parker S. Paxman R. Warmuth M. Wilson A. Zaugg T. Georges III, J.A. High-speed closed-loop dual deformable-mirror phase-diversity testbed. 671105(September 2007):671105, 2007.

[36] Bell R. Duncan A.L. Love G.D. Acton D.S. Kendrick, R.L. Closed loop wavefront correction using phase diversity. *Space Telescopes and Instruments V*, (August 1998):844–853, 1998.

[37] Korkiakoski V. Doelman N. Fraanje R. Andrei R. Verhaegen M. Keller, C.U. Extremely fast focal-plane wavefront sensing for extreme adaptive optics. *Adaptive Optics Systems III, Proc. SPIE*, 8447(July):844721, 2012.

[38] Wang J. Wang B. Li H. Ma, X. Phase diversity for calibrating noncommon path aberrations of adaptive optics system under nonideal measurement environment. *Optik*, 125(17):5029–5035, 2014.

[39] F. Zernike. Beugungstheorie des schneidenver-fahrens und seiner verbesserten form, der phasenkontrastmethode. *Physica*, 1(7):689–704, 1934.

[40] R.J. Noll. Zernike polynomials and atmospheric turbulence. 66(3):207, 1976.

[41] K. Strehl. Aplanatische und fehlerhafte Abbildung im Fernrohr. *Zeitschrift für Instrumentenkunde*, 15(7):362—370, 1895.

[42] Saxton W.O. Gerchberg, R.W. A practical algorithm for the determination of phase from image and diffraction plane pictures. *Optik*, 35(2):237–246, 1972.

[43] R.A. Gonsalves. Phase retrieval and diversity in adaptive optics. *Optical Engineering*, 21(5), 1982.

[44] R.A. Gonsalves. Sequential diversity imaging of extended sources. *Proc. SPIE*, 4792(December 2002):26–34, 2002.

[45] Korkiakoski V. Doelman N. Fraanje R. Andrei R. Verhaegen M. Keller, C.U. Extremely fast focal-plane wavefront sensing for extreme adaptive optics. *Adaptive Optics Systems III, Proc. SPIE*, 8447(September 2012):844721, 2012.

[46] J.R. Janesick. *Photon Transfer*, volume PM170. 2007.

[47] R.G. Paxman and J.R. Fienup. Optical misalignment sensing and image reconstruction using phase diversity. *Journal of the Optical Society of America A*, 5(6), 1988.

[48] Schulz T.J. Fienup J.R. Paxman, R.G. Joint estimation of object and aberrations by using phase diversity. *Journal of the Optical Society of America A*, (7), 1992.

[49] NASA's Jet Propulsion Laboratory. AVIRIS Data Portal. `https://aviris.jpl.nasa.gov/alt_locator/`.

[50] Paxman R.G. Zarifis V.G. Benson L. Stone R.E. Seldin, J.H. Closed-loop wavefront sensing for a sparse-aperture multitelescope array using broadband phase diversity. *Conference proceedings of SPIE*, (October 2000):48–63, 2000.

[51] J.B. Johnson. Thermal Agitation of Electrical Conductors. *PHYSICAL REVIEW'*, 32, 1928.

[52] P. Cattin. Image restoration: Introduction to signal and image processing, 2016.

[53] W. Schottky. Über spontane Stromschwankungen in verschiedenen Elektrizitätsleitern. *Annales de Physique*, 57:541, 1918.

[54] Woods R.E. Gonzalez, R.C. *Digital Image Processing*. 1977.

[55] B. Widrow. *Digital Image Processing*. Cambridge University Press, 2008.

[56] Toots M. Öfverstedt L.G. Skoglund U. Mahmood, F. 2D Discrete Fourier Transform with Simultaneous Edge Artifact Removal for Real-Time Applications. pages 2–5, 2016.

[57] F.J. Harris. On the use of windows for harmonic analysis with the discrete fourier transform. *Proceedings of the IEEE*, (1), 1978.

[58] Scharmer G.B. Lofdahl, M.G. Wavefront sensing and image restoration from focused and defocused solar images. *Astronomy and Astrophysics Supplement Series*, 107:243–264, 1994.

[59] O. von der Luehe. Speckle imaging of solar small scale structure. i - methods. *Astronomy & Astrophysics*, 268(3), 1993.

[60] Crippen S.L. Paxman, R.G. Aberration correction for phased-array telescopes using phase diversity. (November 1990):787–797, 1990.

[61] Fienup J.R. Bolcar, M. *Sub-aperture piston phase diversity for segmented and multi-aperture systems*. PhD thesis, 2009.

[62] Roggemann M.C. Welsh B.M. Crosby E.R. Lee, Da.J. Evaluation of least-squares phase-diversity technique for space telescope wave-front sensing. *Applied Optics*, 36(35):9186, 1997.

[63] Chan T.F. Plemmons R.J. Vogel, C.R. Fast algorithms for phase-diversity-based blind deconvolution. (September 1998):994, 1998.

[64] S. Ruder. An overview of gradient descent optimization algorithms. pages 1–14, 2016.

[65] N. Wiener. *Extrapolation, interpolation, and smoothing of stationary time series*. MIT Press, 1942.

[66] C.W. Helstrom. Image restoration by the method of least squares. *Journal of the Optical Society of America*, 57(3), 1967.

[67] Caulfield H.J. Yaroslavsky, L.P. Deconvolution of multiple images of the same object. *Applied Optics*, 33(11), 1994.

[68] W.H. Richardson. Bayesian-Based Iterative Method of Image Restoration*. *Journal of the Optical Society of America*, 62(1):55, 1972.

[69] L.B. Lucy. An iterative technique for the rectification of observed distributions. *The Astronomical Journal*, 79(6):745–749, 1974.

[70] Andrews M. Biggs, D.S.C. Acceleration of Image Restoration Algorithms. *Applied Optics*, 36(8):1766–1775, 1997.

[71] Kuiper J.M. Dolkens, D. Active Correction System of a Deployable Telescope for Earth Observation. In *International Conference on Space Optics*, volume 19, pages 9–12, 2018.

[72] Pedrino E.C. Roda V.O. Russo L.M. Kato, E. Image convolution processing: A GPU versus FPGA comparison. *SPL 2012 - 8th Southern Programmable Logic Conference*, (2010):1–6, 2012.